

**DEVELOPMENT OF IN-SITU TECHNIQUES FOR PREDICTING  
PEB TEMPERATURE**

**REGINALD LI FENG YIING**

(B. Eng (Hons.), NUS)

**A THESIS SUBMITTED  
FOR THE DEGREE OF MASTER OF ENGINEERING  
DEPARTMENT OF ELECTRICAL AND  
COMPUTER ENGINEERING  
NATIONAL UNIVERSITY OF SINGAPORE**

**2003**

# CONTENTS

<b>SUMMARY .....</b>	<b>iii</b>
<b>LIST OF FIGURES .....</b>	<b>v</b>
<b>LIST OF TABLES .....</b>	<b>vii</b>
<b>LIST OF ABBREVIATIONS .....</b>	<b>viii</b>
<b>CHAPTER 1 .....</b>	<b>1</b>
1.1 Motivation.....	1
1.2 Thesis Organization .....	4
<b>CHAPTER 2 .....</b>	<b>6</b>
2.1 Introduction.....	6
2.2 Deep-UV Lithography .....	8
2.2.1 <i>Imprinting the Image</i> .....	9
2.2.2 <i>Chemically-Amplified Resist</i> .....	11
2.2.3 <i>Post-exposure bake or PEB</i> .....	11
2.3 The Integrated Bake/Chill Machine.....	16
2.3.1 <i>The Turntable</i> .....	17
2.3.2 <i>The Multi-zone Hotplate</i> .....	18
2.3.3 <i>In-situ Temperature Measurement System</i> .....	19
2.3.4 <i>Machine Operation</i> .....	21
2.4 The Influence of Poor Thermal Contact .....	22
<b>CHAPTER 3 .....</b>	<b>26</b>
3.1 Sensor Parameter Estimation Using the LCSR Test.....	26
3.1.1 <i>Sensor Transfer Function</i> .....	27
3.1.2 <i>Identifying the Sensor Parameters Using the LCSR Test</i> .....	30
3.1.3 <i>Simulation Results</i> .....	33
3.2 The AD7711AN Signal Conditioning ADC Chip .....	34
3.2.1 <i>Design Considerations</i> .....	36
3.3 Design A .....	39
3.3.1 <i>Basic Principle</i> .....	39
3.3.2 <i>The External High Current Circuit</i> .....	41
3.3.3 <i>Choice of Maximum High Current</i> .....	43
3.3.4 <i>Software Modifications</i> .....	43
3.3.5 <i>Experimental Results</i> .....	44
3.4 Design B .....	46
3.4.1 <i>Calibrating the Modified Measurement Board</i> .....	48
3.5 Experimental Results .....	49

<b>CHAPTER 4</b> .....	<b>52</b>
4.1    The Compensation Algorithm .....	52
4.2    Experimental Results .....	55
4.2.1 <i>The Choice of Filter Pole</i> .....	55
4.2.2 <i>The Closed Loop Performance</i> .....	58
4.3    The Need for an Accurate Estimate of K.....	62
<b>CHAPTER 5</b> .....	<b>64</b>
5.1    Mathematical Derivation .....	64
5.2    Simulation Results .....	71
5.3    Caveat .....	76
5.4    Relationship between K and $\tau$ .....	81
5.4.1 <i>The Experimental Results</i> .....	81
5.5    Experimental Results .....	83
5.5.1 <i>Good Thermal Contact</i> .....	84
5.5.2 <i>Poor Thermal Contact</i> .....	88
<b>CONCLUSION</b> .....	<b>92</b>
<b>REFERENCES</b> .....	<b>95</b>

## SUMMARY

As there is an ever-increasing need to pack more features into smaller chip packages at the lowest possible cost, the wafer fabrication process has to be optimized to produce the greatest possible yield. With the move towards DUV lithography and its necessary use of chemically amplified resists, one aspect of fabrication that is influential in the control of linewidth is the development of the photoresist after it has been imaged. Tight control of the post-exposure bake temperature across the entire wafer is crucial in ensuring proper reaction of the chemically amplified resist. For proper development of the resist, temperature variations have to be within  $\pm 1^{\circ}\text{C}$  when the wafer temperature is beyond  $60^{\circ}\text{C}$  and  $\pm 0.1^{\circ}\text{C}$  at steady state.

Closed loop wafer temperature control requires the use of contact temperature sensors to measure and feedback the current wafer temperature. As wafers are loaded for processing, the level of thermal contact between the temperature sensor and wafer varies and this can degrade the quality of the feedback signal. Experiment results showed that poor thermal contact can cause temperature differences of up to  $3.8^{\circ}\text{C}$ . Such a large difference in temperature can affect the reactions of the chemically amplified resist and the ability to maintain tight linewidth control across the wafer. In-situ testing of the temperature sensor's parameters may be conducted using the Loop Current Step Response test which provides an indication of the extent of thermal contact. To perform the LCSR test in-situ, the existing temperature measurement board had to be modified. The hardware design principles and considerations, and the

LCSR test results of the modified system were presented. The software modifications were also noted.

Knowing the sensor's parameters, a software compensation algorithm can be used to post-process the sensor's readings and recover the actual wafer temperature. The mathematical basis of the algorithm was presented. It was demonstrated that with the algorithm the temperature difference could be reduced to within  $\pm 1^\circ\text{C}$  during transient and  $\pm 0.1^\circ\text{C}$  at steady state.

If the LCSR test was performed separately from the PEB step, additional time would be incurred, reducing the throughput of wafers processed. A solution would be to perform the LCSR test concurrently with the PEB step. An algorithm was proposed to enable this. The mathematical derivation of the algorithm and its simulated performance were presented. The simulation results showed that there is a caveat to the use of the algorithm, and so a workaround was proposed. Experimental results demonstrated that the sensor parameters could be obtained when the LCSR test was performed during the PEB temperature ramp. The subsequent closed loop temperature control of the wafer was able to maintain the measurement error to within  $\pm 1^\circ\text{C}$  when the wafer temperature is beyond  $60^\circ\text{C}$  and  $\pm 0.1^\circ\text{C}$  at steady state.

## LIST OF FIGURES

Figure 1-1. Exponential increase in the number of transistors produced [1].....	1
Figure 2-1. The photoresist spin-coating process .....	8
Figure 2-2. The ultra-violet portion of the EM spectrum .....	9
Figure 2-3. Step-and-repeat system .....	10
Figure 2-4. Process latitude for a 0.5 $\mu$ m lithography with respect to exposure dose, PEB duration and PEB temperature [10] .....	14
Figure 2-5. SEM photographs of resolution stars for wafers with PEB temperatures a PEB duration of 90s at (a) 65 $^{\circ}$ C (b) 90 $^{\circ}$ C (c) 100 $^{\circ}$ C [10].....	15
Figure 2-6. Cross-section showing the layout of the machine [10].....	16
Figure 2-7. The turntable .....	17
Figure 2-8. The multi-zone hotplate .....	18
Figure 2-9. Functional block diagram of temperature measurement board.....	20
Figure 2-10. Operation of the bake-chill machine .....	22
Figure 2-11. Closed loop control performance when feedback sensor has good and bad thermal contact with wafer .....	25
Figure 3-1. Schematic of temperature sensor model .....	28
Figure 3-2. Simulation result of LCSR test .....	33
Figure 3-3. Details of the AD7711AN.....	34
Figure 3-4. Analog input impedance .....	38
Figure 3-5. Simplified schematic of LCSR circuit (first modification).....	41
Figure 3-6. LCSR Profile of design A .....	45
Figure 3-7. Simplified schematic of LCSR circuit (second modification).....	46
Figure 3-8. Straight-line fit of Channel 13 calibration data.....	49
Figure 3-9. LCSR result of design B for good thermal contact.....	50
Figure 3-10 LCSR result of design B for poor thermal contact.....	50
Figure 4-1. Functional block diagram of temperature measurement system.....	54
Figure 4-2. Comparing measurement noise with and without filter .....	57
Figure 4-3. Comparison of closed loop performance .....	59
Figure 4-4. Temperature difference between feedback and reference sensor .....	61
Figure 5-1. Functional block diagram of temperature measurement.....	66
Figure 5-2. A typical wafer temperature profile during PEB [8].....	67
Figure 5-3. Illustration of high current and PEB temperature ramp .....	72

Figure 5-4. Simulation results of parameter estimation algorithm .....	75
Figure 5-5. Simulation wafer temperature profile over the first 10s of PEB ramp with noise added .....	76
Figure 5-6. Illustration of a 0.5s delay in starting data logging.....	77
Figure 5-7. Dynamic response of closed loop performance simulation .....	80
Figure 5-8. Temperature difference between actual and compensated readings for $\hat{\tau} = 0.73s$ .....	80
Figure 5-9. Best fit line representing relation between $\tau$ and $K$ .....	82
Figure 5-10. Functional block diagram of simulation to generate PEB temperature rise .....	85
Figure 5-11. Experimental result of LCSR test with wafer heating for sensor with good thermal contact .....	85
Figure 5-12. Experimental result of closed loop control with compensation for sensor with good thermal contact .....	87
Figure 5-13. Temperature difference between the compensated measurement and reference sensor for experiment with good sensor thermal contact .....	88
Figure 5-14. Experimental result of LCSR test with wafer heating for sensor with poor thermal contact .....	90
Figure 5-15. Experimental result of closed loop control with compensation for sensor with poor thermal contact.....	91
Figure 5-16. Temperature difference between the compensated measurement and reference sensor for experiment with poor sensor thermal contact.....	91

## LIST OF TABLES

Table 2-1. Summary of steps for fabricating a single layer.....	7
Table 2-2. Temperature sensitivity of various chemically-amplified resists [2] .....	13
Table 3-1. Comparison of high and nominal current measurements.....	40
Table 3-2. Calibration data for Channel 13 after modifications.....	48
Table 4-1. The estimated sensor parameters.....	58
Table 4-2. Simulation results with and without high-current data.....	63
Table 5-1. The estimated coefficients from simulation .....	73
Table 5-2. The estimated parameters from simulation .....	73
Table 5-3. The estimated parameters from simulation with noise added .....	74
Table 5-4. Variation of estimates with delay in measurement .....	77
Table 5-5. Variation of estimates with delay in measurement, in the presence of measurement noise .....	78
Table 5-6. Corresponding values of $\tau$ and $K$ .....	82
Table 5-7. The identified parameters for a sensor with good thermal contact .....	84
Table 5-8. The identified parameters for a sensor with poor thermal contact.....	89

## LIST OF ABBREVIATIONS

ADC	Analog-digital Converter
CAR	Chemically amplified resist
CD	Critical dimension
DUV	Deep ultraviolet photolithography
EM	Electromagnetic
Hz	Hertz
IC	Integrated circuit
IEC	International Electrotechnical Commission
LCSR	Loop current step response test
PAG	Photoacid generator
PC	Personal computer
PEB	Post-exposure bake
PI	Proportional-Integral control
rpm	Revolutions per minute
RTD	Resistance temperature detector
SEM	Scanning electron microscope
SIA	Semiconductor Industry Association
VAC	Alternating current voltage
VDC	Direct current voltage
ZOH	Zero-order hold

# CHAPTER 1

## INTRODUCTION

### 1.1 Motivation

The introduction of new semiconductor technologies now exceeds the rate predicted by Moore's Law. Microprocessor speed doubles every four years and, every five years, the number of bits produced increases tenfold [1]. Wafer, chip-die sizes and feature densities have become ever larger as wafer processing technology advances. This development results from the incessant move towards the fabrication of finer features over larger chip-die sizes on bigger wafers. The latest prediction from the Semiconductor Industry Association's (SIA) International Technology Roadmap for Semiconductors (ITRS) indicates that feature density can only increase as time progresses (Figure 1-1).

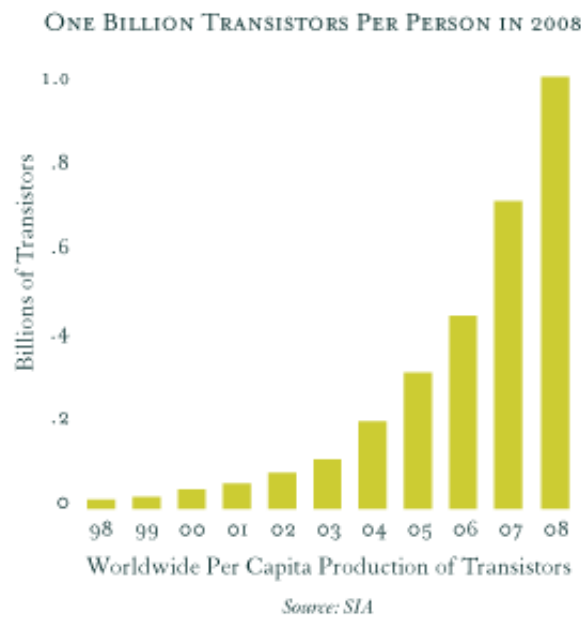


Figure 1-1. Exponential increase in the number of transistors produced [1]

In summary, the current trends in the semiconductor industry include :

- decreasing feature size
- increasing need for reduced defect density
- increasing interconnect levels
- reducing chip cost

These trends place tremendous pressure on the industry to produce chips that pack an ever-greater amount of components into an ever-shrinking area, with the greatest possible yield and at the lowest possible cost. To meet such a demand, every aspect of the wafer fabrication process has to perform well.

Variation in temperature uniformity across-die and across-wafer is an important factor affecting the quality and yield in wafer processing [2]. With better control of absolute and spatial temperature distribution across the wafer during the several baking steps in the lithographic sequence, linewidth variations can be kept to a minimum. Furthermore, the widespread adoption of deep ultra-violet (DUV) lithography has necessitated the use of chemically-amplified resists, which are more sensitive to temperature variations than traditional Novolac resists. Thus, the search for better wafer temperature control has now greater impetus.

A method by which temperature regulation may be improved is closed-loop control. Unfortunately, it is difficult to achieve accurate in-situ monitoring of spatial temperature distribution using either contact or non-contact temperature sensors. The measurement accuracy of contact temperature sensors such as thermocouples and RTDs are dependent on the amount of thermal contact between the transducer and the

wafer surface. As a wafer is simply placed on the hot-plate during PEB process, it is difficult to ensure that there is good and consistent thermal contact between the wafer and the sensors. Consequently, the sensor output is unreliable.

An alternative to contact sensors are non-contact temperature sensing techniques that are based on the detection of infrared radiation. However, the accuracy of non-contact temperature sensors is dependent on the emissivity of the target material. If the emissivity is less than 1.0, the radiation power actually emitted from the material surface is less than expected and a non-contact sensor will give a reading that is lower than the true surface temperature. Another problem is that semiconductors are substantially transparent in the spectral range where thermal radiation is emitted because they have very small emissivity. Due to the fact that wafers are semi-transparent to IR radiation, radiation from the underlying devices (e.g., heater) will also be picked up by the sensor [3]. Even in more sophisticated infrared thermometers where a pulsed laser is emitted and the amount of reflected energy measured, the accuracy is specified as  $\pm 3^{\circ}\text{C}$  [4]. Such accuracy is insufficient for use in wafer temperature uniformity control. The difficulties in using of contact and non-contact sensors to accurately measure wafer temperature have hindered the widespread use of closed loop temperature control. It is, therefore, worthwhile to explore methods for improving the accuracy of contact sensors so they can be used in the semiconductor fabrication process.

This thesis seeks to demonstrate that measurement accuracy, and therefore wafer temperature control, can be improved by using a software compensation algorithm to post-process the readings obtained using a resistance temperature detector (RTD). The

proposed algorithm is able to obtain the sensor response characteristics required for the compensation algorithm without interrupting existing fabrication procedures, thereby maintaining the throughput of wafers processed.

## **1.2 Thesis Organization**

The thesis is organized as follows :

Chapter 2 will introduce the basic processes in patterning a wafer. It will describe the move towards deep ultra-violet photolithography and the use of chemically amplified photoresists. The integrated bake/chill machine in which the experiments are performed on is then described, with emphasis on its main components. To provide motivation for the work presented in this thesis, the effect of poor thermal contact between the temperature sensor and the wafer on the performance of closed loop control is also demonstrated.

Chapter 3 will introduce the principles of the Loop Current Step Response test which is used to determine the sensor parameters. The existing measurement board design is introduced, focusing on the AD7711AN chip, which is an analog front-end chip for the RTD that provides the excitation current and analog-digital conversion of the temperature measurements. The principles and design considerations for the hardware modifications to incorporate the LCSR test function are then presented. Finally, the experimental result of an LCSR test performed using the modified measurement board is presented.

Chapter 4 presents the derivation of the proposed software compensation algorithm. The algorithm has the characteristics of a high-pass filter which will amplify high frequency noise and requires the introduction of a low-pass filter to remove the high frequency signals. The choice of the low-pass filter pole is discussed and its experimental impact demonstrated. The performance of a closed loop controller that utilizes the algorithm to improve sensor accuracy is then shown. A point is noted on the need for an accurate estimate of sensor parameter  $K$ . Another stumbling block is that the duration of the LCSR test is long compared to the time taken to complete the PEB. As a result, manufacturing throughput will suffer.

Chapter 5 presents the algorithm that enables the estimation of the sensor parameters to be estimated via an LCSR test during the PEB process. The mathematical derivation of this algorithm is shown, followed by the simulation results demonstrating its viability. Simulation results showed that the sensor gain estimated using the proposed algorithm depends on how accurately the start of the PEB process can be synchronized with the LCSR test. Hence, a possible workaround for this problem is proposed. The experimental procedure for demonstrating the performance of the algorithm is then described, and the experimental results presented.

## CHAPTER 2

### THE WAFER PATTERNING PROCESS

#### 2.1 Introduction

An integrated circuit (IC) is a semiconductor device that contains electronic components fabricated on a silicon substrate. A semiconductor device is fabricated by transferring layer upon layer of circuit patterns onto a wafer. As feature sizes decrease and the amount of interconnects increase, precise fabrication of chip features becomes critical.

Photolithography is the all-important process that creates the layers of circuit patterns on the wafer surface. It is one of the most critical operations in wafer fabrication because it determines the horizontal surface dimension that can be produced on a wafer. A photolithography system typically costs more than one third the costs of processing a wafer to completion. Although this cost will increase as minimum feature size on a semiconductor chip decreases, optical lithography remains attractive because of its high wafer throughput [5].

There are two primary objectives in the photolithography process. One is the creation of pattern features whose dimensions are as close to the design requirements as possible. The accuracy of this process is termed the resolution of the images. The second is the accurate layering of circuit patterns over one another. This is termed the registration or alignment. An entire layer has to be correctly placed and the individual

parts of a circuit must be in the correct positions relative to each other. Failure in this step could prevent the interconnecting vias from linking adjoining layers of circuit, rendering the chip defective. Each step in the photolithography process contributes variations to the patterning process, and cumulative errors can ultimately cause the chip to fail.

<b><u>Process Step</u></b>	<b><u>Purpose</u></b>
1. Surface preparation	Cleaning and drying of wafer surface (dehydration) to promote resist adhesion
2. Photoresist application	Application of a thin layer of chemically-amplified photoresist to the wafer by spin-coating
3. Exposure	Precise alignment of mask to wafer and exposure to DUV light. Then pattern image is projected onto wafer
4. Post-exposure bake	Baking at about 90°C to activate catalyst that drives image development in chemically-amplified resist
5. Development	Removal of unwanted resist by dissolving resists in developer
6. Develop Inspection	Inspection of wafer for alignment and defects (ie. Correctness of image transfer)
7. Etching	Top layer of wafer is removed
8. Photoresist removal	Removal of photoresist layer from wafer
9. Final inspection	Surface inspection for etch irregularities and other problems

Table 2-1. Summary of steps for fabricating a single layer

In general, the sequence of steps for patterning a single layer can be summarized as in Table 2-1 [6]. Before the image of the circuit is projected onto the wafer, photoresist is first dripped onto the centre of the wafer and then spun to eventually form a uniform and very thin layer (Figure 2-1). Upon exposure to UV light, the exposed regions then undergo chemical changes. A post-exposure bake (PEB) is then performed to activate

the reactions in the exposed regions, causing them to become soluble. The unexposed regions remain insoluble and protect the underlying substrate from subsequent processing. After the PEB, the soluble regions are removed and the exposed regions of the wafer are processed. Once the processing is complete, the photoresist is completely removed.

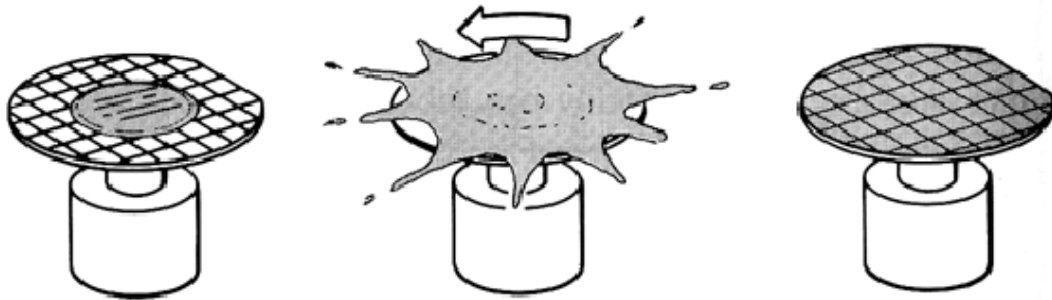


Figure 2-1. The photoresist spin-coating process

## 2.2 Deep-UV Lithography

The demand for finer features has driven the technology of optical lithography to the deep-UV (DUV) range. Figure 2-2 shows the ultra-violet portion of the electromagnetic wave spectrum and the move towards shorter wavelength with deep-UV lithography.

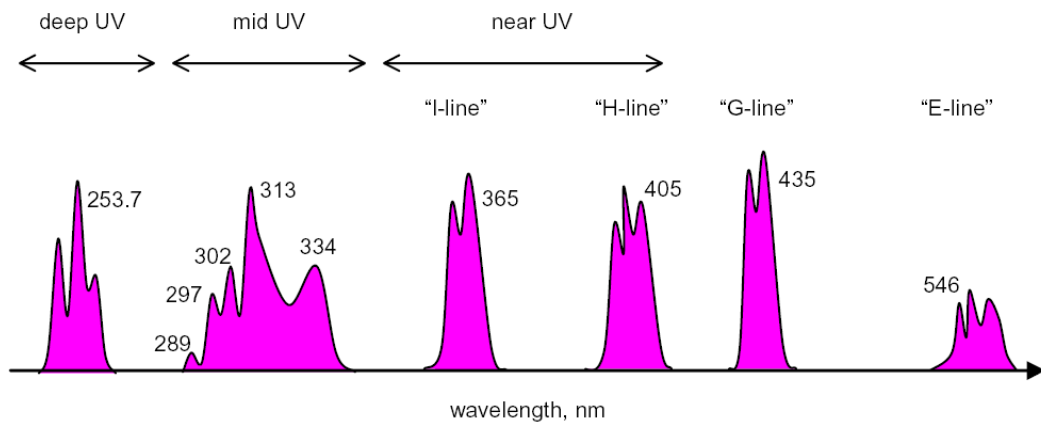


Figure 2-2. The ultra-violet portion of the EM spectrum

The shift to deep-UV also involved a new type of light source, the development of special projection lenses, and the introduction of new resist materials that exhibit sufficient transparency to deep-UV exposures [6]. Transparency to deep-UV light is necessary for the projected light to penetrate through to the bottom of the photoresist layer. Otherwise, exposure of the photoresist would not be uniform across the depth of the photoresist, thereby deteriorating the imprinted image quality. The following sections describe various aspects of DUV lithography.

### 2.2.1 *Imprinting the Image*

The most commonly used patterning technique is the step-and-repeat method performed on a machine called a stepper, as illustrated in Figure 2-3. In DUV lithography, the light source is an excimer laser which is focused onto the wafer through a series of mirrors and lens. A mask is aligned with the wafer and exposed to the light source, then ‘stepped’ to the next site. This process is then repeated over the entire wafer surface. In reduction stepper systems, a large mask is used and the projected image is then reduced (usually at a ratio of 5:1). The use of a large mask

ensures that any stray pattern introduced by dirt or glass distortion in the mask is reduced to insignificance. Also, a large mask is easier to fabricate and repair.

The advantage of a step-and-repeat system is that each chip is individually aligned, resulting in better pattern overlay and registration. Since a single mask is used throughout the entire process, the wafer images are potentially more uniform. Other improvements include better resolution and reduced vulnerability to dust and dirt since a smaller area is exposed each time.

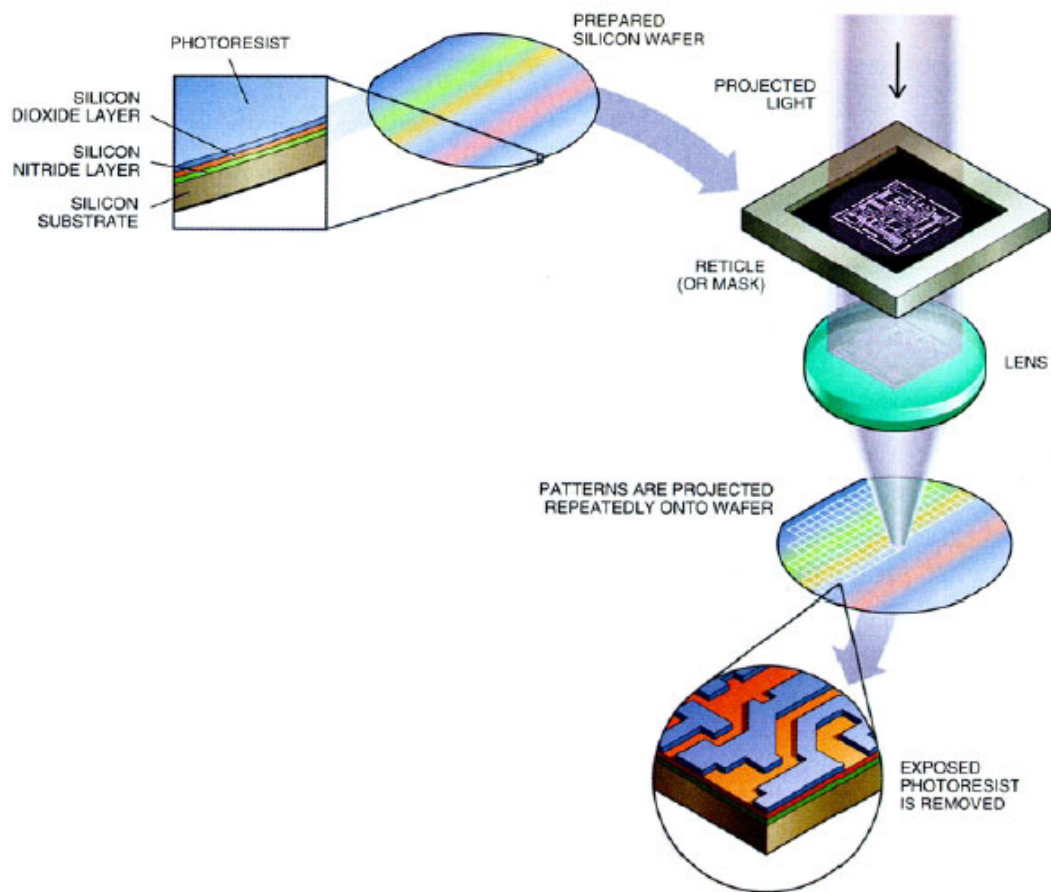


Figure 2-3. Step-and-repeat system

Good linewidth control and overlay can be obtained because focus and alignment can be adjusted during the scan of each field to match the topography and previous level

pattern. With a bright illumination source, high throughput can be achieved because the stage can be scanned at high speeds [7].

### ***2.2.2 Chemically-Amplified Resist***

With the move towards DUV lithography, traditional photoresists could no longer be used. They do not perform adequately because of their inability to become more transparent when exposed to deep-UV wavelength light. Furthermore, the intensities of DUV light sources are lower. To circumvent this intrinsic sensitivity limitation and to dramatically increase the resist sensitivity, the concept of chemical amplification was introduced.

In chemical amplification, a catalytic species generated by irradiation triggers off a series of subsequent chemical transformations, providing a gain mechanism. An additional photoactive compound commonly called photoacid generator (PAG) is added to the photoresist. The PAG dissolves into a strong acid when exposed to light. A post-exposure bake is required to thermally induce a chemical reaction, which may be the activation of a cross-linking agent for a negative resist or the deblocking of the polymer resin for a positive resist. The acid acts as a catalyst so that it is hardly consumed by the reaction, and can continue driving the deblocking process. For example, one molecule of PAG might trigger 500 to 1000 chemical reactions [8].

### ***2.2.3 Post-exposure bake or PEB***

In DUV lithography, PEB takes on a more critical role than traditional photolithographic techniques. In the use of chemically-amplified resists, PEB is

necessary to drive the catalytic reaction to completion. Three phenomena compete in the resist [2] during the PEB process :

1. Deprotection of the resist, which renders the exposed regions soluble during resist development. The rate of the deprotection reaction is a function of temperature and the concentration of the reactants and it increases with temperature.
2. Photoacid diffusion. After exposure, the exposed regions of the resist layer have much higher concentrations of acid than the unexposed regions. This difference in concentration causes the acid to diffuse from the exposed to the unexposed regions. Acid diffusion results in deprotection of the chemically amplified resist beyond the exposed regions which can ultimately deteriorate the image quality.
3. Photoacid loss due to neutralization by base species in the exposed regions. The amount of acid loss increases with PEB temperature [9] due to a greater likelihood of encounter with base species. This reduction in acid concentration leads to a slowing of the rate of deprotection reaction. However, base in the unexposed regions act as a trap for diffusing acid and neutralizes it.

The complex interaction between these three phenomena influences the quality of the final image formed in the resist. The discussion also highlights the important role played by the PEB temperature in the chemical reactions.

<b>Table 1. Thermal sensitivity of CA DUV resists during post-exposure bake</b>			
<b>Resist</b>	<b>Supplier</b>	<b>Sensitivity (nm/°C)</b>	<b>Reference</b>
APEX E	Shibley	16.0	2
UV2HS	Shibley	7.5	2
Version 1B (193nm)	IBM	3.8	3
UV6	Shibley	2.6	3
TM-461	JSR	2.6	3
DP-024	TOK	1.8	3
ARCH 2	Arch	0	3
R2J	JSR	0	3

Table 2-2. Temperature sensitivity of various chemically-amplified resists [2]

Table 2-2 shows the temperature sensitivity of various chemically amplified resists. While there is the option of selecting a chemically amplified resist with lower temperature sensitivity, this is not without trade-offs. For instance, although the APEX-E resist has high temperature sensitivity, its use is widespread because of its excellent resolution. In general, resists that are less temperature-sensitive have lower activation energies (the deblocking reaction can occur at room temperature) and hence have lower shelf-life [2].

The effect of post-exposure bake on linewidth control was studied by Sturtevant et al. [9], where the process parameters considered were PEB temperature, PEB duration and exposure dose. It was found that of the three process parameters, the process latitude for PEB temperature was the highest, indicating that PEB temperature is the most critical parameter for linewidth control. Figure 2-4 shows the respective process latitudes, expressed in terms of percentage CD change per percentage parameter change.

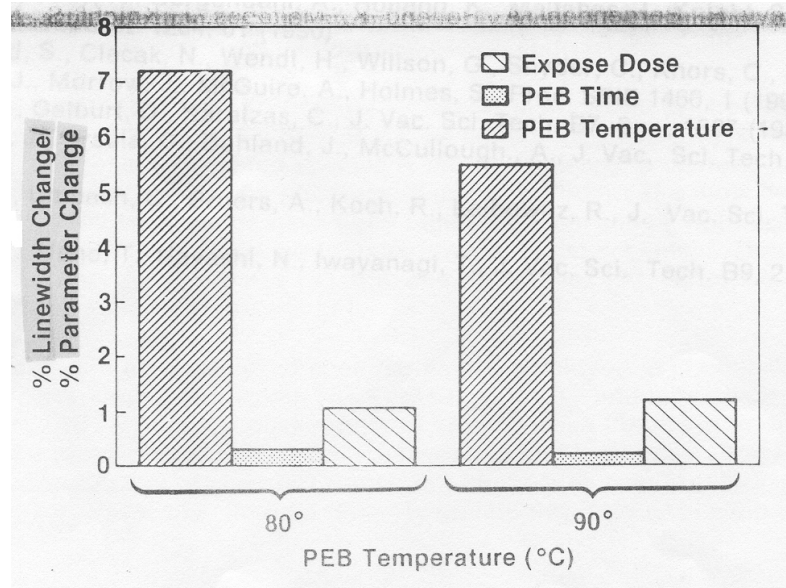


Figure 2-4. Process latitude for a 0.5µm lithography with respect to exposure dose, PEB duration and PEB temperature [9]

Figure 2-5 shows the effect of PEB temperature on the ability to fabricate a star pattern of feature size graduating from 0.25µm at the centre to 1.5µm at the edge. The PEB temperatures studied were 65°C, 90°C and 100°C over a PEB duration of 90s. At 65°C, the 0.3µm lines were resolved, while at 100°C only lines larger than 0.7µm were resolved. The features were best resolved at 90°C. Sturtevant et. al suggests that photoacid loss due to neutralization by base species and photoacid diffusion are the factors behind the above-mentioned trends. Thus, the PEB has a primary influence on resist performance and wafer temperature uniformity during the PEB process is important.

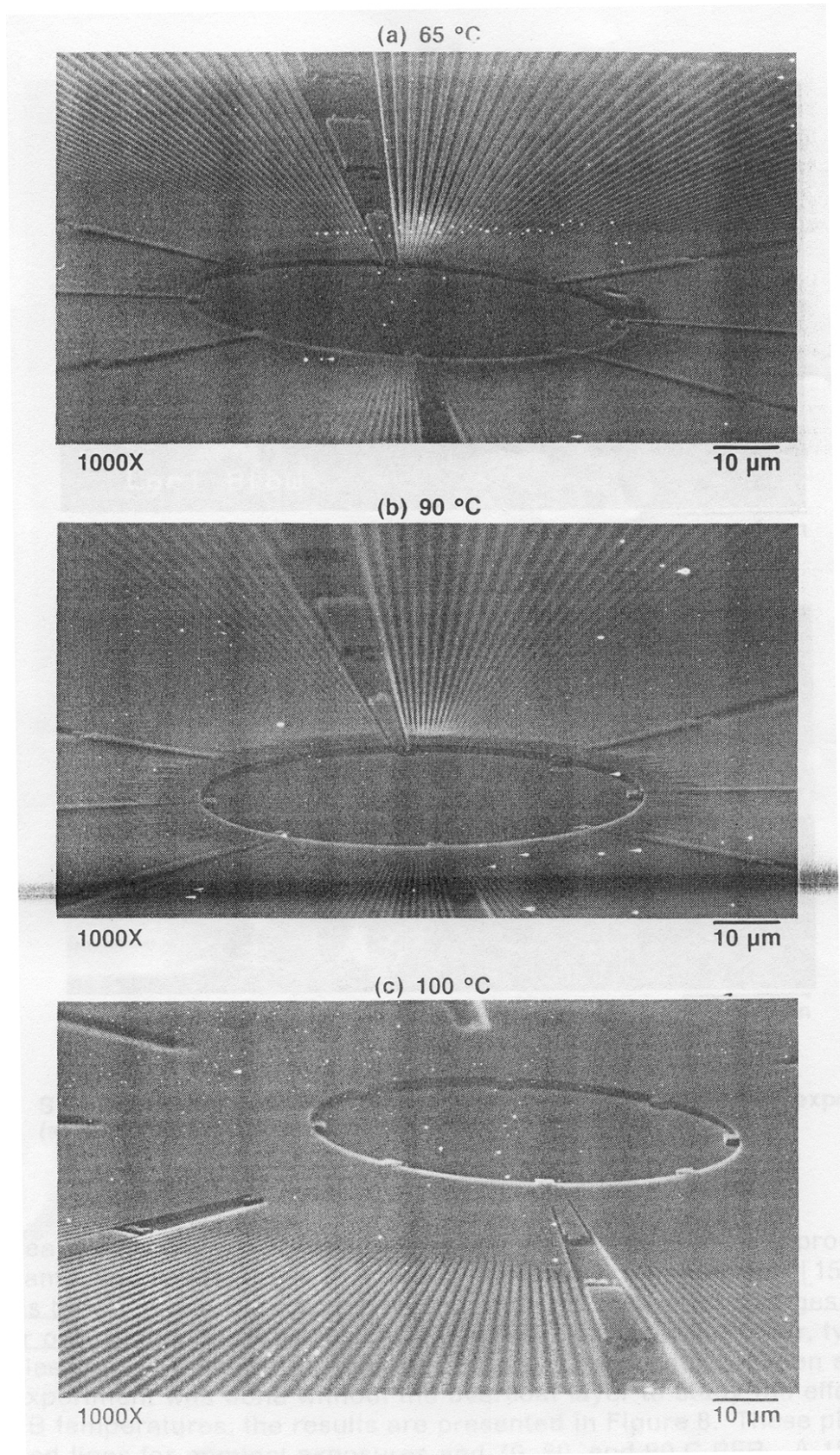


Figure 2-5. SEM photographs of resolution stars for wafers with PEB temperatures a PEB duration of 90s at (a) 65 °C (b) 90 °C (c) 100 °C [9]

## 2.3 The Integrated Bake/Chill Machine

The integrated bake-chill machine was designed with the aim of improving linewidth control and increasing the throughput of wafers processed. Section 2.2.3 noted the importance of PEB in the processing of wafers, and Section 2.2.2 further noted the sensitivity of chemically-amplified resists to PEB temperature. Hence, there is a need for a system that is designed to maintain wafer temperature uniformity across a wafer with the ultimate goal of achieving tight linewidth control. Figure 2-6 shows the cross-section of the integrated bake-chill machine.

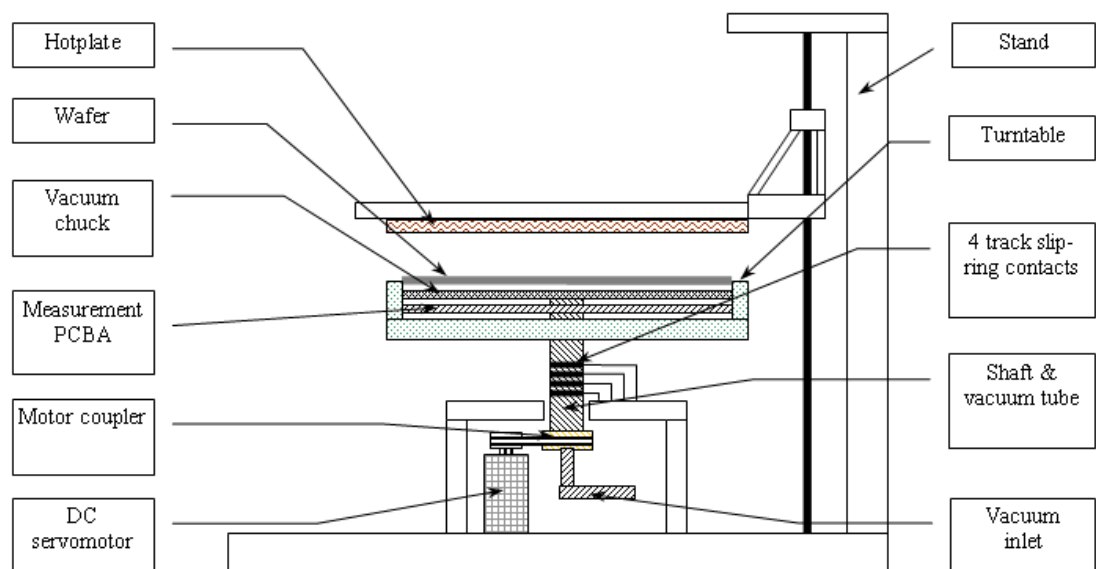


Figure 2-6. Cross-section showing the layout of the machine [10]

The key components of the integrated bake-chill machine are :

- A rotating turntable upon which the wafer is placed
- A multi-zone heating system
- An integrated temperature measurement system

### 2.3.1 *The Turntable*

The turntable houses the vacuum chuck, the in-situ temperature measurement board and the temperature sensors. It also serves as the platform upon which the wafers are placed.



Figure 2-7. The turntable

The motivation for spinning the wafer is to improve annular temperature uniformity. Spinning the wafer below the heater provides each wafer annulus with more consistent thermal conditions for both bake operation and heat dissipation. With a revolution speed of 600rpm, the temperature uniformity can be kept to within 0.1°C [11].

An added benefit of the rotating turntable is the ability to perform spin-coating of photoresist on the same platform. This removes the need to have the spin-coating

done separately and reduces the number of transfers of wafer. Furthermore, with the spin-coating and baking performed within the same machine, latter processing steps can commence as the former nears completion. For instance, towards the end of the spin-coating step with a typical full speed at 3000-6000rpm [12], the prebake step can be initiated without waiting for the turntable to come to a complete stop.

### ***2.3.2 The Multi-zone Hotplate***

The multi-zone hotplate consists of 7 heating zones. Figure 2-8 is a photograph of the hotplate.



Figure 2-8. The multi-zone hotplate

The machine can be configured to operate in two modes. One mode is wafer temperature control mode, where the wafer temperature readings from the in-situ measurement board are used as the feedback signal. The other mode is heater control mode, where the heater temperature readings from the sensors in the hotplate are used

as the feedback signal. This flexibility allows the machine, when it is not performing PEB of wafers, to maintain the heaters at a setpoint temperature.

### ***2.3.3 In-situ Temperature Measurement System***

The in-situ temperature measurement system enables the bake/chill machine to meet the ultimate objective of ensuring temperature uniformity across a wafer, as detailed in [10]. The two primary components of the temperature measurement system are :

- A temperature measurement board that is capable of 16 channels of concurrent measurements. The temperature measurement board is embedded in the body of the turntable and provides in-situ measurement of the wafer temperature.
- A computer running Labview, which provides the user interface

The temperature measurement board is connected to the temperature sensors and provides the necessary signal conditioning and data conversion. Its primary components are :

- an Intel 80C196KC microcontroller that controls the various sub-systems
- a PSD401A2 controller peripheral chip to provide address and data demultiplexing, address decoding and additional logic inputs and outputs for receiving commands or controlling other devices
- Analogue Devices AD7711AN signal conditioning chips that provide a stable built-in current of 200 $\mu$ A for exciting the RTDs and performs analogue-to-digital conversion
- Honeywell HRTS-5670 platinum resistance temperature detectors. The general characteristics of RTDs are provided in Appendix A

- ICL-232 serial communication chip to transmit the acquired data to a personal computer.
- MAX882 linear regulator chips to condition the board's power supply

Figure 2-9 presents a functional block diagram of the temperature measurement board

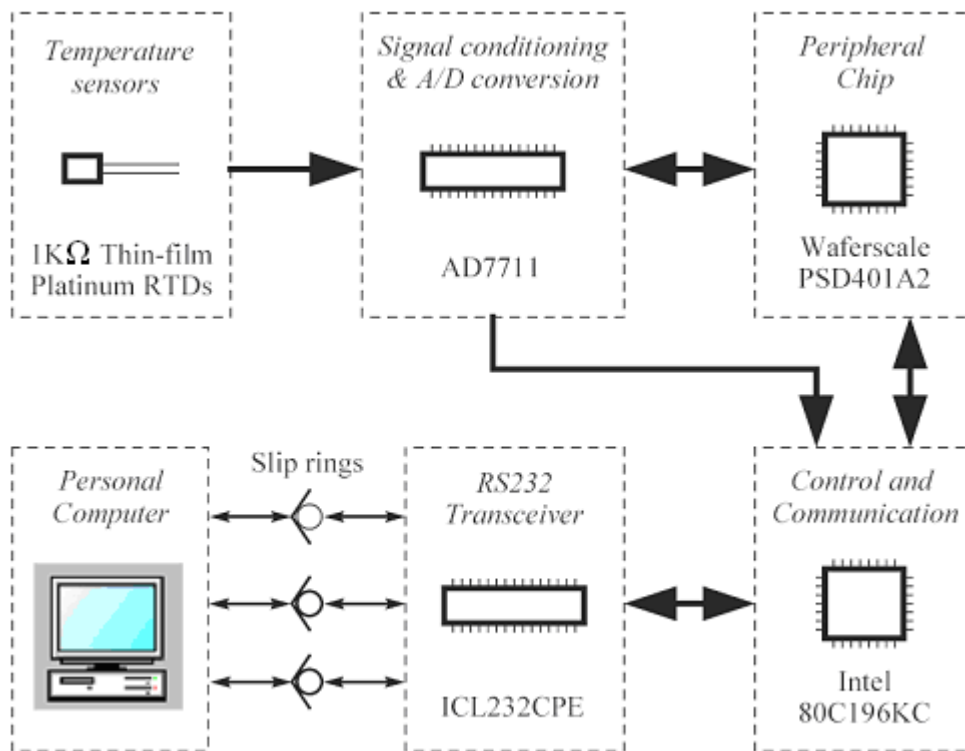


Figure 2-9. Functional block diagram of temperature measurement board

Before the board begins running, a firmware is first downloaded into the PSD401A2 chip. The functions of the firmware include :

- defining the operational modes of the 80C196KC, PSD401A2 and AD7711AN
- defining which pins on the 80C196KC and PSD401A2 are active and their corresponding functions
- initialization functions
- running the user programs

The firmware is compiled from several source codes, each of which is written specifically for a chip, or for the user program. The final product is a hexadecimal-format file which is downloaded into the PSD401 chip and executed by the 80C196KC microcontroller.

Each measurement channel consists of one temperature sensor and one AD7711AN chip. The AD7711AN chip passes a constant 200 $\mu$ A current through the temperature sensor and measures the voltage across the RTD. Since the excitation current is constant, the voltage across the RTD is proportional to its resistance and may be used to infer the temperature. The AD7711AN's ADC then converts the measured voltage to a 24-bit digital number and transmits that serially to the PSD401 chip. A total of 16 pins on the PSD401 are assigned to receiving the digital numbers from the AD7711ANs, one pin for each channel. As the PSD401 reads all 16 pins concurrently, the data from these 16 channels appear multiplexed at the PSD401 pins. The onboard firmware performs the de-multiplexing that recovers the digital numbers from each channel. These digital numbers are then passed to the RS-232 transceiver which then transmits them to the PC.

#### ***2.3.4 Machine Operation***

Figure 2-10 illustrates the operation of the bake-chill machine during PEB. The wafer is loaded onto the turntable and the latter rotated. The wafer is held down in place by suction force via eight vacuum cups. The RTDs in contact with the wafer measure its temperature, and the measurement signal is then processed by the temperature measurement system embedded in the turntable. The processed signals are then relayed to the PC which runs the closed loop temperature control scheme. Based on

the feedback signal, the PC outputs a 0-5VDC signal to the power modules, which is then translated into a 0-240VAC electrical drive that powers the heaters. Thus, the amount of heat applied to the wafer depends on the current wafer temperature.

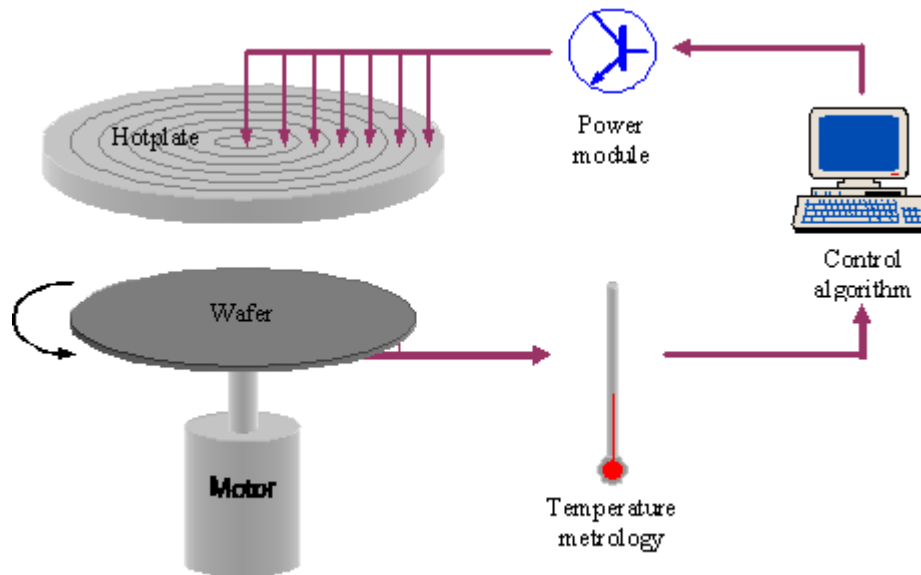


Figure 2-10. Operation of the bake-chill machine

## 2.4 The Influence of Poor Thermal Contact

Closed-loop control techniques can provide tighter temperature control. However, it is effective only if an accurate feedback signal is available. This section examines the influence of thermal contact level on the performance of a closed-loop controller. As the study aims at ascertaining the effect of poor feedback signal on control performance, a simple single-input single-output control system was used. Instead of multi-zone heating, the heater was configured into a single zone and the temperature on one point of the wafer was measured when it is heated from the room temperature of approximately 27°C to a typical PEB temperature of 90°C [13].

The experimental procedures were as follows :

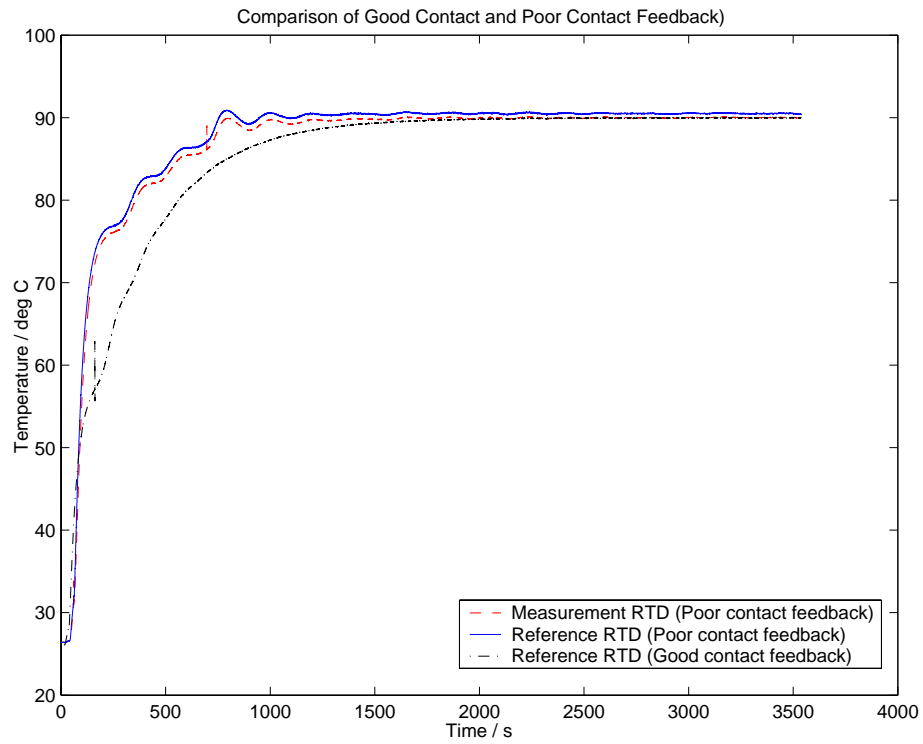
1. Before starting each experiment, the heating unit was moved away from the turntable. The steady-state temperature of the heater was then regulated at 130°C before work commenced. This temperature is the level that gives rise to a wafer temperature that is approximately equal to the steady state PEB temperature of 90°C .
2. The wafer was placed on the turntable and the hot-plate lowered so that the distance between the heater and the wafer was approximately 2.5 mm.
3. Temperature readings acquired by the temperature measurement system was passed to a Proportional plus Integral (PI) controller in order to manipulate the wafer temperature. The proportional gain ( $P$ ) and integral gain ( $I$ ) is 10 and 0.03 respectively. The sampling rate was 4Hz.

Two experiments were performed : one where the feedback signal was from the RTD that had good thermal contact with the wafer, and another in which the contact was poor. Poor thermal contact was simulated by pasting a layer of tape on the sensing surface of the sensor so that it was not in direct contact with the wafer. In order to gauge the effect of a poor contact sensor on the ability of the feedback system to maintain temperature uniformity, a reference RTD was mounted beside the poor contact sensor to obtain an indication of the wafer temperature. Good thermal contact between the reference RTD and the wafer was ensured by using a liberal amount of thermal paste.

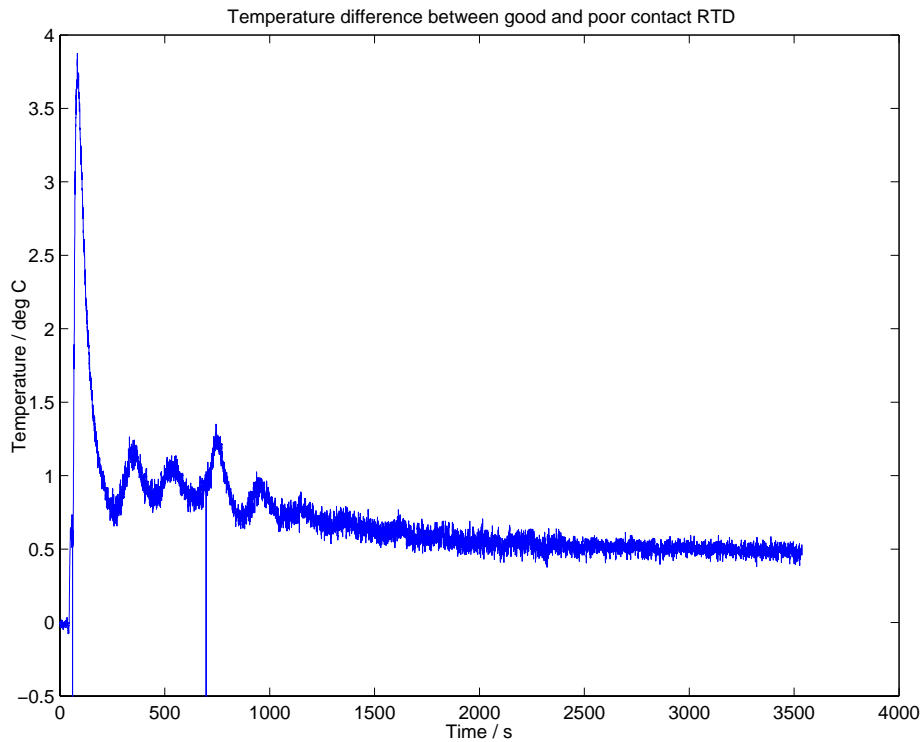
The wafer temperature rise profile obtained using sensors that have good and poor contact with the wafer are compared in Figure 2-11(a). The plots show that the step response is more oscillatory when the feedback signal is provided by a sensor that has

poor thermal contact. This may be caused by the fact that the time constant of a sensor which has poor contact is no longer negligible. Consequently, the effective order of the closed-loop system is increased leading to an oscillatory step response. Figure 2-11(b) shows the difference between the outputs of the two sensors.

During the PEB process, the desired spatial uniformity on a wafer is  $\pm 1^{\circ}\text{C}$  from  $60^{\circ}\text{C}$  to the PEB temperature of  $90^{\circ}\text{C}$  and  $\pm 0.1^{\circ}\text{C}$  at steady state [13]. It may be concluded from Figure 2-11(b) that the PEB temperature specifications cannot be achieved if the feedback signal passed to the various zones of the multi-zone heater is derived from sensors that have varying level of thermal contact with the wafer. Thus, an algorithm for improving the accuracy of the measurement is needed.



(a) Wafer heating profiles, showing effect of poor thermal contact



(b). Temperature difference between good and poor thermal contact sensors

Figure 2-11. Closed loop control performance when feedback sensor has good and bad thermal contact with wafer

## **CHAPTER 3**

### **THE LOOP CURRENT STEP RESPONSE TEST AND THE MEASUREMENT HARDWARE**

The variability of thermal contact between the temperature sensor and the wafer can deteriorate the quality of the feedback signal for closed loop control. To overcome this, an algorithm that processes the feedback signal to remove any variability in measurement accuracy is needed. Since this algorithm must operate online, an in-situ method for identifying the response characteristics of the sensor is essential. This chapter will introduce the Loop Current Step Response (LCSR) test that is used to determine the properties of the temperature sensor. The hardware modifications to incorporate the LCSR test function into the existing temperature measurement board are then documented. Finally, the experimental results of the LCSR test are presented.

#### **3.1 Sensor Parameter Estimation Using the LCSR Test**

Before software compensation can be used to improve the quality of the measured signal used to perform feedback control, the response characteristics of the sensor must first be determined. This can be achieved by the Loop Current Step Response (LCSR) test. This test is performed in-situ, with the sensor installed in the operating environment. The primary advantages of this test are that the sensor need not be removed for testing, and the test captures all factors that affect the response time of the sensor. The use of the LCSR test requires knowledge of the temperature sensor's model which represents its response characteristics. It also requires a means of

identifying the model's parameters from the LCSR test data obtained. These are detailed in the following sections.

### **3.1.1 Sensor Transfer Function**

Any change in temperature at any point in the sensing element can be assumed to arise from [14] :

1. Changes in the temperature of the sensor's surroundings
2. Self-heating effect due to passing of electrical current through the resistive sensing element
3. Combined effect of the above two changes

Schematically, such behaviour can be represented by Figure 3-1, where the symbols used represent :

$T_m(s)$	Measured temperature
$T_a(s)$	Actual medium temperature
$P(s)$	Electrical power generated in the sensor
$T_i(s)$	Rise in temperature due to self-heating
$K_p$	Transfer function of electro-thermal conversion in sensor
$G_1(s)$	Transfer function for temperature sensing of medium
$G_2(s)$	Transfer function for internal self-heating

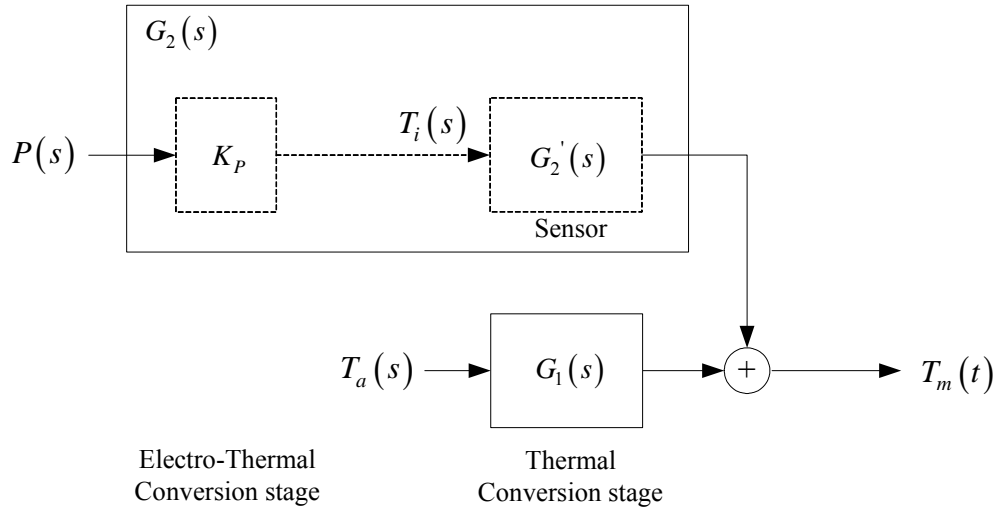


Figure 3-1. Schematic of temperature sensor model

The lower path models the direct temperature measurement and the classical immersion identification method with external excitation. Assuming that the sensor may be modelled as a multi-layer cylinder and the thermal capacitance between the sensing element and the central axis is negligible, the transfer function of the thermal conversion stage for externally excited immersion tests is given in Equation (3.1).

$$G_1(s) = \frac{T_m(s)}{T_a(s)} = \frac{K}{\prod_{i=1}^n (1 + s\tau_i)} \quad (3.1)$$

The upper path starting from  $P(s)$  models the self-heating effect when the temperature of the sensor's surroundings is constant. Since an RTD requires a constant excitation current to be passed through it, a current  $I$  passing through a resistance  $R$  generates a heating effect  $I^2R$ . This is converted into an internal temperature  $T_i(s)$  in the electro-thermal conversion stage of the model. For self-heating tests, the transfer function is given by

$$\begin{aligned}
G_2'(s) &= \frac{T_m(s)}{T_i(s)} \\
&= \frac{K \prod_{i=1}^m (1 + sN_i)}{\prod_{i=1}^n (1 + s\tau_i)}
\end{aligned} \tag{3.2}$$

and

$$\begin{aligned}
G_2(s) &= \frac{T_m(s)}{P(s)} \\
&= K_p G_2'(s) \\
&= \frac{K_p K \prod_{i=1}^m (1 + sN_i)}{\prod_{i=1}^n (1 + s\tau_i)}
\end{aligned} \tag{3.3}$$

RTDs are encapsulated in a protective sheathing and so the thermal energy of the surroundings is first transmitted through the protective sheath before reaching the sensing element. Thus, the two heat transfer processes and the schematic in Figure 3-1 can be modelled as

$$T_m(s) = \frac{K}{(\tau_1 s + 1)(\tau_2 s + 1)} T_a(s) + \frac{K_p K (1 + Ns)}{(\tau_1 s + 1)(\tau_2 s + 1)} P(s) \tag{3.4}$$

where  $\tau_1$  Thermal resistance of the protective sheath  
 $\tau_2$  Thermal resistance of sensing element

The RTD used for this project has a thin ceramic protective sheath and so the thermal resistance of the sheath is negligible relative to that of the sensing element. Thus,  $\tau_1 \ll \tau_2$  and the model of the sensor may be further simplified to

$$T_m(s) = \frac{K}{\tau_2 s + 1} T_a(s) + \frac{K_p K}{(\tau_1 s + 1)} P(s) \tag{3.5}$$

The zero in the second term is removed so that the transfer function is strictly proper.

### 3.1.2 Identifying the Sensor Parameters Using the LCSR Test

An RTD is a resistive element whose resistance varies with temperature. A known constant excitation current is passed through the RTD, generating a voltage across it from which the resistance can be found. Thus, variations in resistance are reflected as variations in the measured voltage across the RTD. The LCSR test involves the sudden change of current through the sensor filament, bringing about a temperature transient. This method exploits the fact that heat transfer resistances and heat capacities are independent of the direction of heat flow. Thus, the same heat transfer characteristics that control the transient response following a change in temperature around the sensor also controls the temperature transient following a change in the current flowing through the filament. Consequently, the test captures all factors that can affect sensor response time in the process.

The sensor's parameters can be found from the LCSR test data using the Least-squares method. Ambient temperature is assumed to be constant and by the Principle of Superposition,  $T_a(s) = 0$  and the first term in Equation (3.5) can be set to zero. The sensor model then becomes

$$T_m(s) = \frac{K_p K}{\tau_2 s + 1} P(s) \quad (3.6)$$

Since the parameters  $K$  and  $\tau_2$  in Equation (3.6) are to be identified, let  $\hat{K}$  and  $\hat{\tau}$  be the estimated static gain ( $K$ ) and time constant ( $\tau_2$ ) respectively. Rearranging Equation (3.6),

$$T_m(s) = -\frac{1}{\hat{\tau}} \frac{1}{s} T_m(s) + \frac{K_p \hat{K}}{\hat{\tau}} \frac{1}{s} P(s)$$

For a step change in the current flowing through the RTD,  $P(s) = \frac{A}{s}$ ,

$$T_m(s) = -\frac{1}{\hat{\tau}} \frac{1}{s} T_m(s) + \frac{\hat{K}}{\hat{\tau}} \frac{K_p A}{s^2} \quad (3.7)$$

Let  $A_2 = K_p A$ . Taking the inverse Laplace transform of Equation (3.7),

$$T_m(t) = -\frac{1}{\hat{\tau}} \int_0^t T_m(t) dt + \frac{\hat{K}}{\hat{\tau}} A_2 t \quad (3.8)$$

During the LCSR test, pairs of  $t$  and  $T_m(t)$  can be recorded. The data pairs may be arranged in the following matrix form,

$$\begin{bmatrix} T_m(t_1) \\ T_m(t_2) \\ \vdots \\ T_m(t_n) \end{bmatrix} = \begin{bmatrix} -\frac{1}{\hat{\tau}} \int_0^{t_1} T_m(t) dt + \frac{\hat{K}}{\hat{\tau}} A_2 t_1 \\ -\frac{1}{\hat{\tau}} \int_{t_1}^{t_2} T_m(t) dt + \frac{\hat{K}}{\hat{\tau}} A_2 t_2 \\ \vdots \\ -\frac{1}{\hat{\tau}} \int_{t_{n-1}}^{t_n} T_m(t) dt + \frac{\hat{K}}{\hat{\tau}} A_2 t_n \end{bmatrix}$$

$$= \begin{bmatrix} \int_0^{t_1} T_m(t) dt & t_1 \\ \int_{t_1}^{t_2} T_m(t) dt & t_2 \\ \vdots & \vdots \\ \int_{t_{n-1}}^{t_n} T_m(t) dt & t_n \end{bmatrix} \begin{bmatrix} -\frac{1}{\hat{\tau}} \\ \frac{\hat{K}}{\hat{\tau}} A_2 \end{bmatrix} \quad (3.9)$$

$$Y = X\theta$$

where

$$Y = \begin{bmatrix} T_m(t_1) \\ T_m(t_2) \\ \vdots \\ T_m(t_n) \end{bmatrix} \quad X = \begin{bmatrix} -\frac{1}{\hat{\tau}} \int_0^{t_1} T_m(t) dt & t_1 \\ -\frac{1}{\hat{\tau}} \int_{t_1}^{t_2} T_m(t) dt & t_2 \\ \vdots & \vdots \\ -\frac{1}{\hat{\tau}} \int_{t_{n-1}}^{t_n} T_m(t) dt & t_n \end{bmatrix} \quad \theta = \begin{bmatrix} -\frac{1}{\hat{\tau}} \\ \frac{\hat{K} A_2}{\hat{\tau}} \end{bmatrix}$$

Equation (3.9) is linear-in-the-parameters. Hence the coefficient vector  $\theta$  can be found using the Least-squares method.

$$\theta = (X^T X)^{-1} X^T Y \quad (3.10)$$

As the coefficient vector  $\theta$  contains two terms, only two equations can be formed to solve for three unknowns ( $A_2$ ,  $\hat{K}$  and  $\hat{\tau}$ ). An additional relationship is needed before the sensor parameters,  $\hat{K}$  and  $\hat{\tau}$ , can be identified on-line. Since the same current is passed through the sensor filament during each LCSR test, the amount of extra electrical power generated and hence,  $A_2$  should remain constant. If  $A_2$  can be determined experimentally off-line, then there will be sufficient information in  $\theta$  to identify  $\hat{K}$  and  $\hat{\tau}$  online. Assuming that the calibration errors are small, the steady-state sensor output will approach the actual temperature when there is good thermal contact between the sensor and the wafer. Consequently, the steady-state gain  $K$  of the sensor transfer function should be unity so that  $T_m(\infty) = T_a(\infty)$ . By performing an LCSR test under good contact conditions,  $A_2$  and  $\hat{\tau}$  can be found by setting  $K$  to 1. Once  $A_2$  is identified, it can be used together with the coefficient vector,  $\theta$ , to determine the sensor parameters online for subsequent tests.

### 3.1.3 Simulation Results

A simulation was performed to verify the model of the sensor and the ability of the least-squares method to identify the sensor parameters. Since the RTD data sheet states that the sensor time constant is 0.6s, and assuming the thermal contact between sensor and wafer is good, the sensor model was chosen as  $G(s) = \frac{1}{0.6s + 1}$ . The LCSR test duration was 15s and the sampling rate was 10Hz. Figure 3-2 shows the result of the simulated LCSR test. Using the Least-squares method in Equation (3.10), the identified  $\hat{\tau}$  and  $\hat{K}$  are 0.6014 and 1 respectively, demonstrating that it is able to accurately identify the sensor parameters from the LCSR test data.

Having introduced the LCSR test, the next step is to incorporate the LCSR test into the existing temperature measurement board so that it can be evaluated experimentally. Before presenting the hardware modifications, the design issues associated with the AD7711 is described.

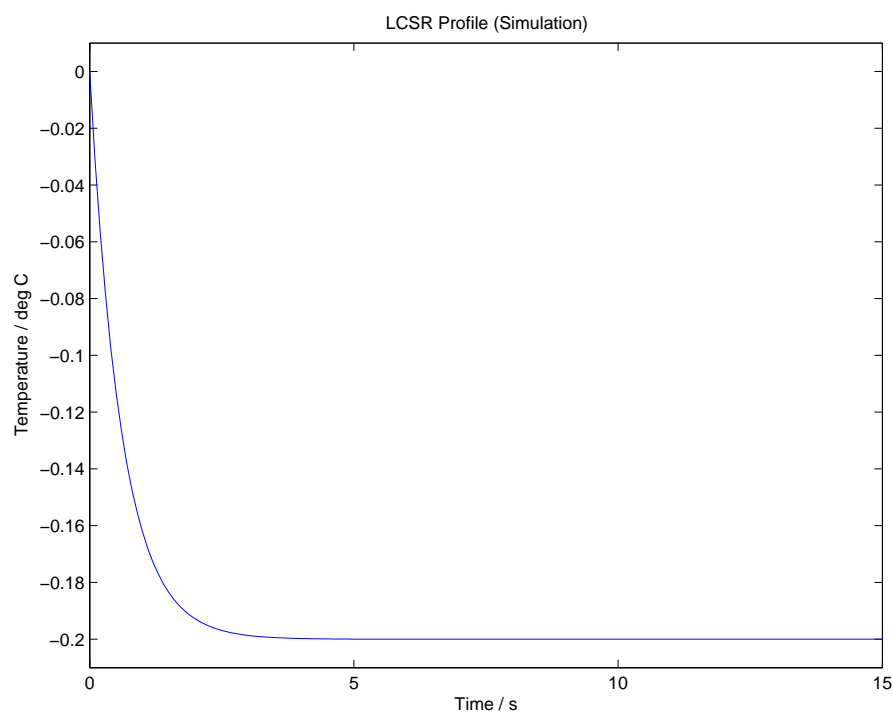


Figure 3-2. Simulation result of LCSR test

### 3.2 The AD7711AN Signal Conditioning ADC Chip

The AD7711AN chip offers a complete analog front end for low frequency measurement applications. It accepts low level signals directly from a transducer and outputs a serial digital word. Figure 3-3 presents the functional block diagram of the AD7711AN chip, showing the primary functions and pins of the chip.

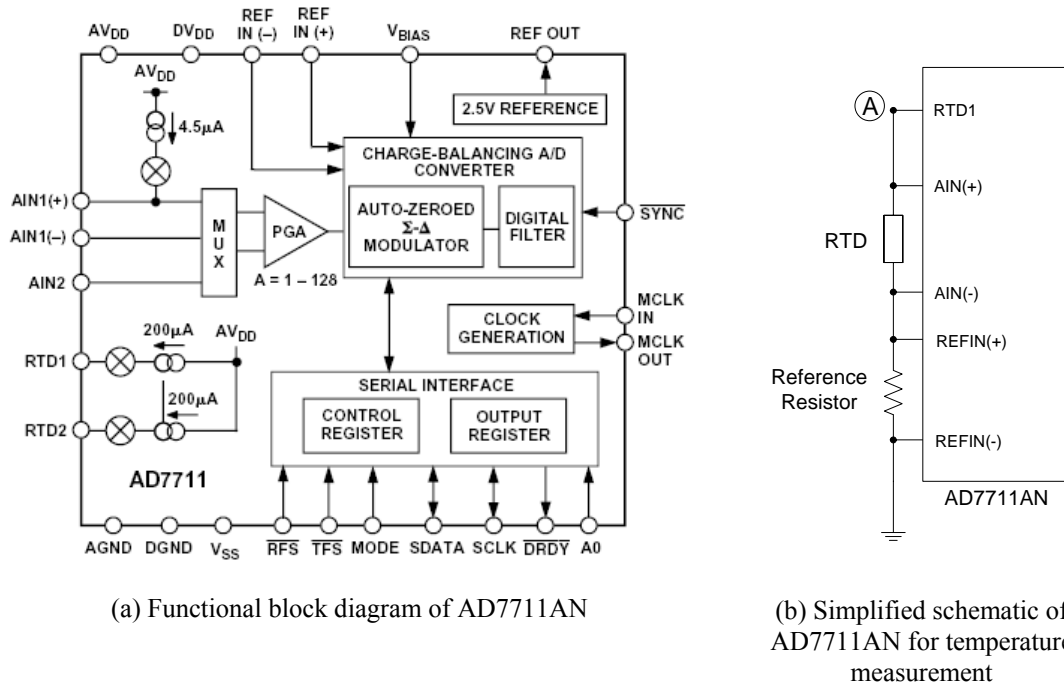


Figure 3-3. Details of the AD7711AN

The functions of the important pins and function blocks is as follows :

- $AINI(+)$  /  $AINI(-)$  : Differential analog input.
- $REFIN(+)$  /  $REFIN(-)$  : Differential reference voltage input.
- $V_{BIAS}$  : Biasing voltage for the AD7711AN internal circuit operation.
- $AV_{DD}$  : Analog positive supply voltage (+5V).
- $V_{SS}$  : Analog negative supply. Since single-rail power supply is used, this pin is connected to  $AGND$ .
- $RTD1$  : Internal current source.
- $REFOUT$  : Built-in 2.5V reference voltage. Can be used as the reference voltage in ratiometric AD conversion of voltage measurements.
- $AGND$  : Ground reference input for analog circuit.

- *PGA* : Programmable gain that allows direct interface with low-level signals. For a given sampling rate, higher gain values increase the signal-to-noise ratio of measurements.
- *Digital Filter* : Sets the sampling rate of the AD7711AN.
- *Control Register* : Defines the operating modes of the AD7711AN.
- $\Sigma$ - $\Delta$  *Modulator* : converts the sampled signal into a digital pulse train whose duty cycle contains the digital information.

The voltage across the temperature sensor is measured via a differential analog input (*AINI(+)* and *AINI(-)* in Figure 3-3a) and applied to a programmable gain (*PGA* in Figure 3-3a). The output from the gain is then sampled and then processed by an on-chip digital filter (*Charge-balancing AD converter* in Figure 3-3a). The first notch of this digital filter determines the sampling rate and hence the amount of measurement noise, and is programmed via the on-chip control register (*Control register* in Figure 3-3a). The input pins *REFIN(+)* and *REFIN(-)* provide the reference voltage for the ratiometric analog-digital conversion of the RTD voltage measurement.

Figure 3-3b shows the existing connections of the AD7711AN for the acquisition of temperature readings. Pin *RTDI* provides the constant excitation current through the RTD and the reference resistor. The pins *AINI(+)*/*AINI(-)* and *REFIN(+)*/*REFIN(-)* measure the voltages across the RTD and reference resistor respectively. The digital output of the AD7711AN chip is the discretized value of the ratio between the measured voltage and the reference voltage. The advantage of a ratiometric scheme is that if the same excitation current is used to excite the RTD and generate the reference voltage (see Figure 3-3b), any variations or drift of the current will not affect the measurements. For instance, let

$V_{RTD}$	Voltage across RTD
$Gain$	Gain of AD7711AN programmable gain ( $PGA$ )
$V_{REF}$	Voltage across reference resistor
$R_{RTD}$	RTD resistance at given temperature
$R_{REF}$	Reference resistor
$I$	Excitation current

$$\begin{aligned}
 \text{Ratiometric result} &= \frac{Gain \cdot V_{RTD}}{V_{REF}} & (3.11) \\
 &= Gain \cdot \frac{I \times R_{RTD}}{I \times R_{REF}} \\
 &= Gain \cdot \frac{R_{RTD}}{R_{REF}}
 \end{aligned}$$

If a stable resistor is chosen as the reference resistor, the measurement readings from the AD7711AN will be stable even in the presence of excitation current fluctuations. Furthermore, the current sources of the AD7711AN have low temperature coefficients. These two factors equip the AD7711AN with excellent measurement stability.

### 3.2.1 Design Considerations

There are several design guidelines/restrictions that must be adhered to for the AD7711AN chip to function properly. They are :

1. The absolute maximum voltage relative to ground applied at any pin is  $V_{SS} + 0.3V$ .
2. For better performance, the recommended  $V_{BIAS}$  is half of  $AV_{DD}$ . The latter is fixed at +5V.
3. There are mutual constraints on  $V_{BIAS}$  and  $V_{REF}$ .

$$V_{BIAS} + 0.85 \times V_{REF} < AV_{DD} \quad \text{and} \quad V_{BIAS} - 0.85 \times V_{REF} > AV_{SS}$$

For the case where  $AV_{DD} = +5V$  and  $V_{SS} = AGND = 0V$ ,  $V_{BIAS} = +2.5V$

(Constraint 2),

$$\begin{aligned} 2.5 + 0.85 \times V_{REF} < 5 & \quad \text{or} \quad 2.5 - 0.85 \times V_{REF} > 0 \\ V_{REF} < 2.94V & \quad \quad \quad V_{REF} < 2.94V \end{aligned}$$

4. For valid readings,  $V_{REF}$  has to be at least 1.1V. A further note is that the lower  $V_{REF}$  is, the greater the measurement noise.
5. The  $\Sigma$ - $\Delta$  converter discretizes voltages bounded by 0V and  $V_{REF}$  into  $2^N$  values, where  $N$  is the number of bits in the digital word. Hence the AD7711AN output will saturate when

$$V_{AIN1} \cdot Gain > V_{REF}$$

The current flowing through the RTD needs to be increased during the LCSR test, but as the output of the AD7711AN chip's built-in current source cannot be altered, an external circuit is needed to provide the high current. The connection between the external circuit and the measurement board can be made at the point labeled as 'A' indicated in Figure 3-3b. Pin *RTDI* is the output of the AD7711AN current source and it has very high output impedance. All the other input pins in Figure 3-3b also have high input impedance. The injected current will simply flow through the RTD and reference resistor down to ground. However, there are a number of other issues that need to be considered in order to safely integrate the external circuit into the existing system

The first consideration is that the analog voltage input pin of the AD7711AN (AIN) is connected to a sampling capacitor (see Figure 3-4). The input sample rate (fCLKIN)

determines the time that the analog input capacitor,  $C_{INT}$ , has to charge up fully before data is sampled. Hence, care must be taken to ensure that the external impedances do not cause the RC time constant to exceed the sampling period. As shown in Figure 3-3b, point A is connected to the  $AINI(+)$  analog input and so the external high current circuit can potentially introduce parasitic impedance to the  $AINI(+)$  input. To take care of this issue, the external circuit must present a very low output impedance so as not to significantly affect the charge-up time of the sampling capacitor  $C_{INT}$ . Alternatively, the output impedance has to be extremely high so as to effectively present an open circuit to the  $AINI(+)$  analog input.

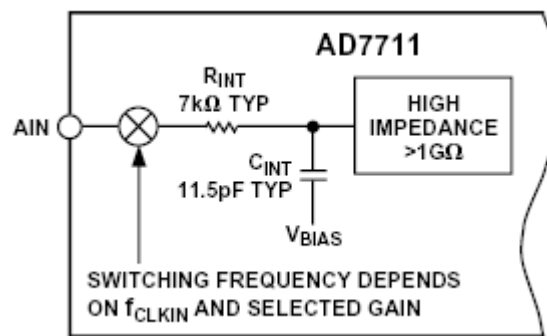


Figure 3-4. Analog input impedance

A second consideration hails from the fact that the signals of these circuits are low. It may, therefore, be prudent to power the external circuit from the same power supply as the measurement board. If more than one power supply is used, there is the possibility that each supply unit will have different ground potential. This can potentially affect the readings when the external circuit is switched into the measurement board. The measurement board utilizes the MAX883 voltage regulator chips, which can accept voltage inputs of up to +11.5VDC single-rail. With this in mind, the components would have to be able to operate from a +11.5VDC single-rail power supply.

Two designs were implemented on the temperature sensor board. The first design sought to incorporate the LCSR function that allowed for measurement of temperature during both the high current and nominal current phase. However due to hardware restrictions, only a limited amount of high current could be injected into the RTD and the resulting self-heating temperature rise was very small. A second design was implemented, which sacrificed the high current temperature measurement for a larger injected current and self-heating temperature rise. The designs are detailed in the following sections.

### **3.3 Design A**

To perform the LCSR test, a high current has to be passed through the RTD to cause self-heating. Furthermore, it is advantageous for the temperature measurement system to be able to acquire temperature readings during both the high and nominal current phases. Thus, the objective for this design is to inject a high current into the RTD and still be able to obtain temperature readings from the RTD during this high current phase. Since the built-in current source of the AD7711AN is fixed at  $200\mu\text{A}$ , an external constant current source circuit is required to provide the high current. For testing purposes, only one measurement channel would be modified.

#### ***3.3.1 Basic Principle***

Since the objective is to obtain the RTD readings during both the high current and nominal current phase, the modifications must allow the data acquired during both phases to be reliable.

The high current increases the amount of self-heating in the RTD, which in turn causes its resistance to increase. Since the reference resistor is stable, its resistance does not change in the presence of a larger current. Defining the following quantities,

$R_{heat}$	increase in resistance due to self-heating
$R_n$	RTD resistance at nominal current
$R_{REF}$	Resistance of reference resistor
$I_h$	Magnitude of high current
$I_n$	Magnitude of nominal current
<i>Gain</i>	Gain of AD7711AN programmable gain amplifier (PGA)

**Table 3-1** compares in general terms the measurements obtained during the nominal and high current phases.

	<u>Nominal Current</u>	<u>High current</u>
$V_{REF}$	$I_n R_{REF}$	$I_h R_{REF}$
$V_{RTD}$	$I_n R_n$	$I_h (R_n + R_{heat})$
Analog value corresponding to AD7711AN output (Equation (3.11))	$\frac{Gain \times V_{RTD}}{V_{REF}}$ $= \frac{Gain \times I_n R_n}{I_n R_{REF}}$ $= \frac{Gain \times R_n}{R_{REF}}$ $= R_n \frac{Gain}{R_{REF}}$	$\frac{Gain \times V_{RTD}}{V_{REF}}$ $= \frac{Gain \times I_h (R_n + R_{heat})}{I_h R_{REF}}$ $= \frac{Gain \times (R_n + R_{heat})}{R_{REF}}$ $= (R_n + R_{heat}) \frac{Gain}{R_{REF}}$

Table 3-1. Comparison of high and nominal current measurements

As the same current flows through both the RTD and the reference resistor, Table 2-1 shows that any change in readings during the high current phase is due only to the

change in RTD resistance caused by self-heating. When the high current is switched away from the RTD, the amount of self-heating decreases and  $R_{heat}$  will gradually decay to 0.

### 3.3.2 The External High Current Circuit

Figure 3-5 is a schematic diagram of the circuit that is used to pass a high current through the RTD.

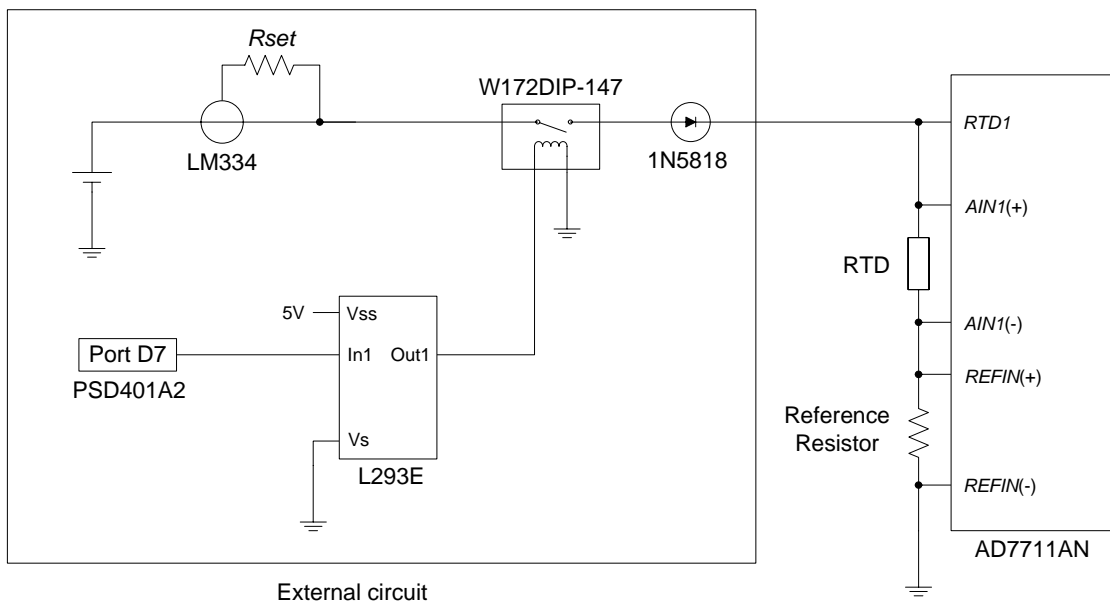


Figure 3-5. Simplified schematic of LCSR circuit (first modification)

The primary components of this design are :

- LM334 Current source to provide the high current.  $R_{SET}$  is used to set the output current
- W172DIP-147 Relay to switch the high current into the RTD
- L293E Relay driver. The L293E relay driver is required because the PSD401 is not able to provide sufficient current to drive the W172DIP-147 relay. The

L293E relay driver acts as a buffer by drawing very little current from the PSD401 and supplying the current required to drive the relay coil.

- 1N5818 Diode to provide a high impedance into the high current circuit. This is to satisfy the design consideration in section 3.2.1, where an external circuit should not cause the RC time constant of the sampling capacitor to increase beyond the sampling period
- AD7711AN Signal conditioning ADC with RTD excitation current to provide the analog front-end signal conditioning and ADC for acquiring temperature readings from the RTD
- PSD401A2 Field-programmable microcontroller peripheral to activate and deactivate the relay driver, thereby controlling the injection of high current into the RTD

All the components in Figure 3-5 can be powered from the same single-rail power supply as the measurement board.

When the LCSR test is activated, Port D7 of the PDS401A2 goes high, turning on the relay driver and closing the relay contact. This closed relay then passes the high current into the RTD and reference resistor. The total current passing through the RTD is the sum of the injected current and the AD7711AN's excitation current. After a pre-specified high current duration, Port D7 goes low which turns off the relay driver and opens the relay contact. Thus, the current through the RTD and the reference resistor reverts to the nominal value. As the amount of self-heating is now reduced, the sensor cools and this is recorded as a first-order decay in the temperature profile.

### 3.3.3 Choice of Maximum High Current

As mentioned in Section 3.2.1 (Constraint 3), the maximum voltage that can be applied to the  $V_{REF}$  pin is 2.94V. The current provided by the external circuit flows through both the RTD and the reference resistor. Consequently, the largest possible current that may be used to drive the RTD is

$$\text{Maximum current through RTD} = \frac{\text{Max } V_{REF}}{R_{REF}}$$

Setting  $R_{REF} = 6\text{k}\Omega$  and since  $\text{Max } V_{REF} = 2.94\text{V}$ ,

$$\begin{aligned}\text{Maximum current through RTD} &= \frac{2.94\text{V}}{6\text{k}\Omega} \\ &= 0.49\text{mA} \\ &= 490\mu\text{A}\end{aligned}$$

As the excitation provided by the AD7711AN is  $200\mu\text{A}$ , the maximum external current is  $290\mu\text{A}$ .

### 3.3.4 Software Modifications

Code was added to the firmware to control the injection of high current into the measurement board by activating and deactivating Port D7 of PSD401 chip. The original firmware also had a function that performed a moving average of the AD7711AN data with a moving average window of 8 samples. As a tradeoff between reducing measurement noise and preventing the averaging from muting the decay profile of the LCSR test, the moving average window was reduced to 4 samples. To accommodate these changes, various existing functions and definitions were modified. The firmware modifications are documented in Appendix B.

### 3.3.5 *Experimental Results*

Besides identifying the sensor time constant, the objective for this experiment is to determine whether the temperature change induced by the self-heating in the RTD is sufficiently large so that the sensor parameter identification is less likely to be affected by measurement noise and ambient temperature variations. In the experimental setup, a high current of about  $410\mu\text{A}$  is first passed through the sensor, causing self-heating and thus, raising the temperature of the sensor. The current is then returned to its nominal value and the sensor temperature decay profile recorded. The experimental setup is as follows :

- Current used to perform LCSR test is  $410\mu\text{A}$  , of which  $210\mu\text{A}$  is provided by the external circuit and  $200\mu\text{A}$  comes from the AD7711AN's internal current source
- High current duration = 30s
- Nominal current duration = 30s
- Sampling rate : 10Hz

Figure 3-6 shows the LCSR profile obtained using the modified circuit board when there is good thermal contact between the sensor and wafer. It shows the high current phase during the first 30s, followed by the temperature decay back to the readings that correspond to the ambient temperature after the high current is switched off. Using least-mean-squares estimation method described in Section 3.1.2, the sensor time constant was found to be  $\hat{\tau} = 0.6057\text{s}$  and the temperature change induced by the increase in electric power generated internally was  $0.0178^\circ\text{C}$ . The estimated  $\tau$  is close to the manufacturer-specified typical value of 0.6s.

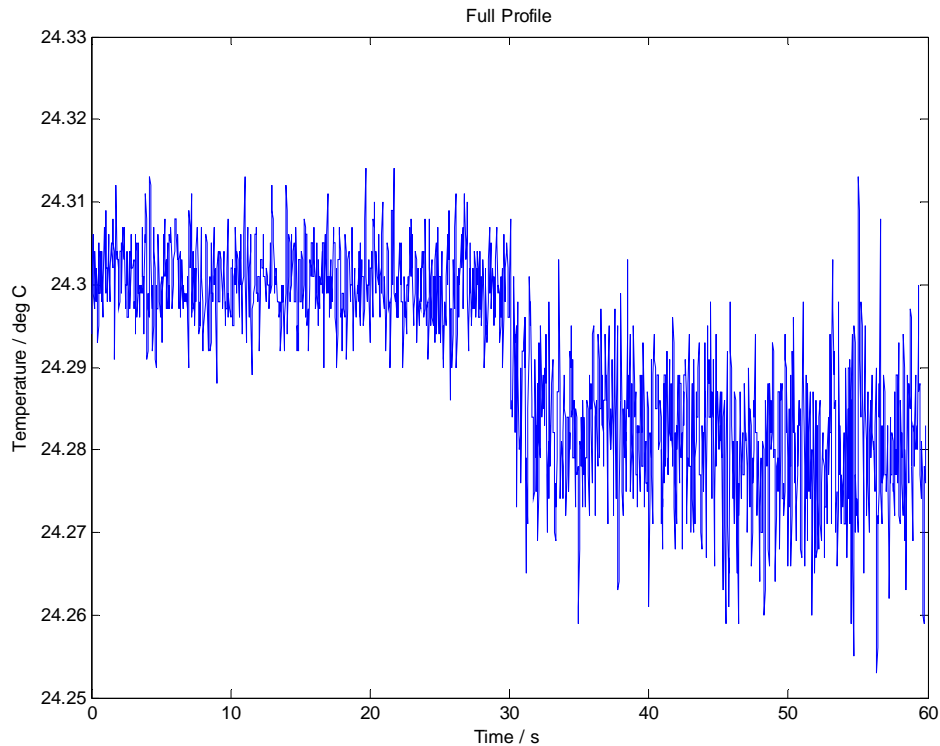


Figure 3-6. LCSR Profile of design A

It has to be noted that the self-heating induced temperature rise is very small (approximately  $0.02^{\circ}\text{C}$ ). With such a small temperature change, there is a chance that measurement noise will be significant relative to the temperature rise, which could affect the accuracy of the estimated sensor parameters. Furthermore, in the presence of ambient temperature fluctuation, the LCSR profile will not decay to a steady state value, but to a gradual upward or downward trend. Such steady state trends can affect the estimation of the sensor parameters. These concerns highlight the limitations of the proposed design. In the following section, a second circuit for performing the LCSR test is described.

### 3.4 Design B

The restriction on the maximum current that could be injected into the RTD is imposed by the decision to pass a common current through the RTD and the reference resistors so that the AD7711AN output will still be valid during the LCSR test. By doing away with the common excitation current and replacing the reference resistor with a constant +2.5V voltage instead, it would be possible to increase the maximum current through the RTD.

Figure 3-7 shows the schematic diagram of the revised design, with the shaded region highlighting the differences from Figure 3-5. The main changes are :

1. The reference resistor  $R_{REF}$  was removed
2. The connection between pin  $AIN1(-)$  and  $REFIN(+)$  severed
3.  $AIN1(-)$  was shorted to ground
4. A new connection was then made between  $REFOUT$  and  $REFIN(+)$

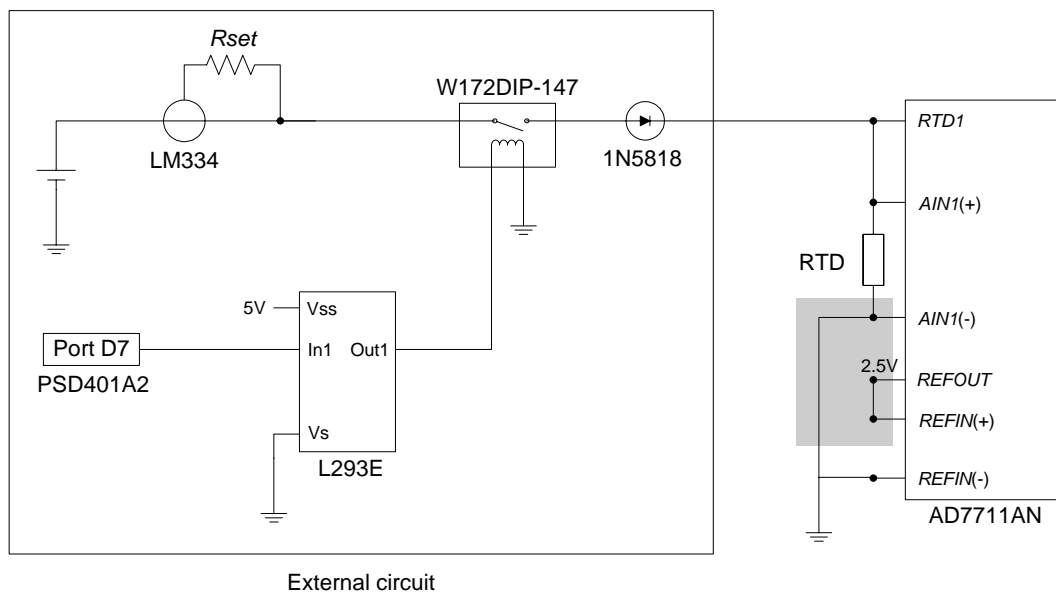


Figure 3-7. Simplified schematic of LCSR circuit (second modification)

It is necessary to sever the connection between  $REFIN(+)$  and  $AINI(-)$  because  $AINI(-)$  is now shorted to ground. Keeping the connection between  $REFIN(+)$  and  $AINI(-)$  would short  $REFOUT$ , which is the built-in 2.5V reference voltage, to ground and damage the AD7711AN. With this change, the excitation current from pin  $RTDI$  flows only through the RTD and down to ground. The full circuit schematics showing the modifications to the temperature measurement board are documented in Appendix C.

The maximum current that can flow through RTD in this design is given by

$$\text{Maximum current through RTD} = \frac{\text{Max } V_{AIN1}}{\text{Gain} \times R_{RTD}}$$

where  $Gain$  is the programmable amplifier gain at the  $AINI(+)/AINI(-)$  input of the AD7711AN. Measuring the resistance of the RTD at room temperature gives a reading of  $1075\Omega$ . For calculations, it is assumed that the RTD resistance at room temperature is  $1100\Omega$ . Setting  $Gain = 4$  and since  $\text{Max } V_{AIN1} = +5V$ ,

$$\begin{aligned} \text{Maximum current through RTD} &= \frac{5V}{4 \times 1100\Omega} \\ &= 1.136\text{mA} \end{aligned}$$

Since the excitation provided by the AD7711AN is  $200\mu\text{A}$ , the maximum external current is  $0.936\text{mA}$ .

The LCSR test will be performed at room temperature. Since  $1100\Omega$  is a typical resistance for a platinum  $1\text{k}\Omega$  RTD at room temperature, the analog input voltage is

$$\begin{aligned} V_{AIN1} \cdot \text{Gain} &= I_h R_{RTD} \cdot \text{Gain} \\ &= 1.1\text{mA} \cdot 1100\Omega \cdot 4 \\ &= 4.8V \end{aligned}$$

This exceeds  $V_{REF}$  and causes the AD7711AN readings to saturate (Constraint 5 in section 3.2.1). Thus, the ability to pass a larger current through the RTD sacrifices the ability to obtain temperature measurements during the high current phase.

### 3.4.1 *Calibrating the Modified Measurement Board*

The modifications involved changing the voltage supplied to the reference input of Channel 13, which requires the measurement board to be re-calibrated to relate the digitized readings to a degree-Celsius value. Calibration was performed by immersing the RTD in a closed loop regulated oil-bath. The oil-bath is a Neslab EX-251 high temperature bath that has a temperature stability of  $\pm 0.01^\circ\text{C}$  at  $60^\circ\text{C}$  [15]. The oil-bath temperature was allowed to settle to a fixed value before the digitized readings of the AD7711AN were recorded. This process was repeated for a temperature range of  $30^\circ\text{C}$  to  $110^\circ\text{C}$  at  $10^\circ\text{C}$  intervals. Table 3-2 shows the calibration data pairs relating the digitized readings to temperature. By fitting the data to a straight line in the least-squares sense, the relationship between them is found to be  $y = 0.3225x - 270.43$ , where  $y$  is the temperature in degree-Celsius and  $x$  is the digitized readings. Figure 3-8 shows the closeness of the straight-line fit to the calibration data.

Temperature / °C	Digitized Readings
30	930.65
40	961.74
50	994.56
60	1025.5
70	1055.8
80	1086.8
90	1117.9
100	1148.4
110	1178.8

Table 3-2. Calibration data for Channel 13 after modifications

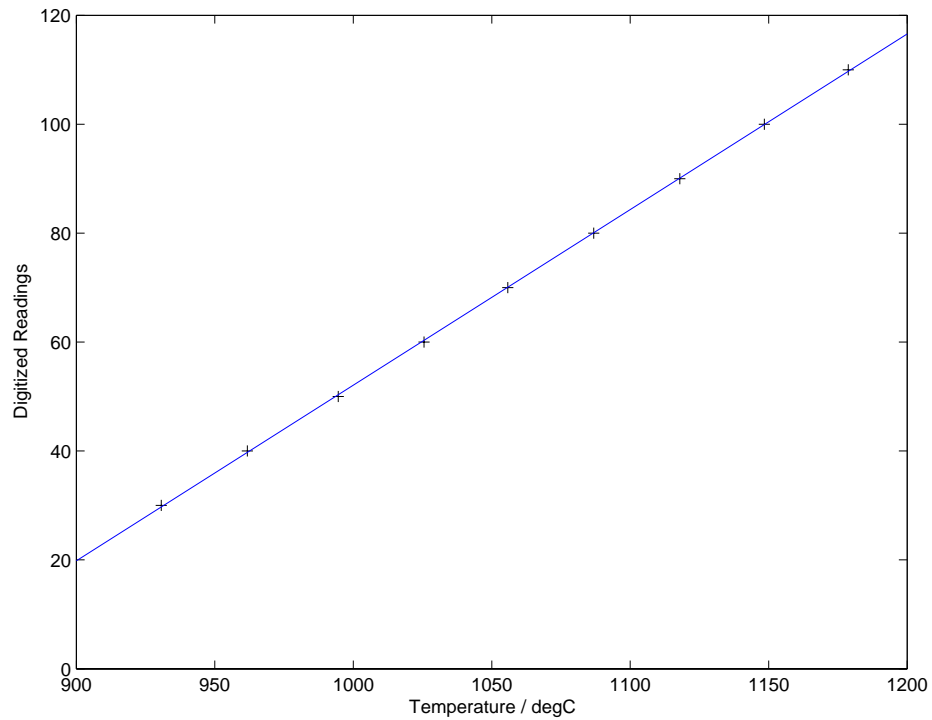


Figure 3-8. Straight-line fit of Channel 13 calibration data

### 3.5 Experimental Results

Figure 3-9 and Figure 3-10 shows the LCSR profile obtained using Design B, for sensors that have good thermal contact and poor thermal contact with the wafer. The high current duration was 20s and the nominal current duration was 60s; the sampling rate was 10Hz. The magnitude of the high current is about 1.1mA. Comparing Figure 3-9 with Figure 3-6, the temperature rise brought about by the larger excitation current for good thermal contact is now much greater at about 0.2°C. The estimated sensor time constant is 0.75s. When thermal contact is poor (Figure 3-10), the estimated time constant is 1.62s. It may be expected that the sensor with the poor thermal contact will have a larger time constant, since the heat generated by the high current will take longer to dissipate away.

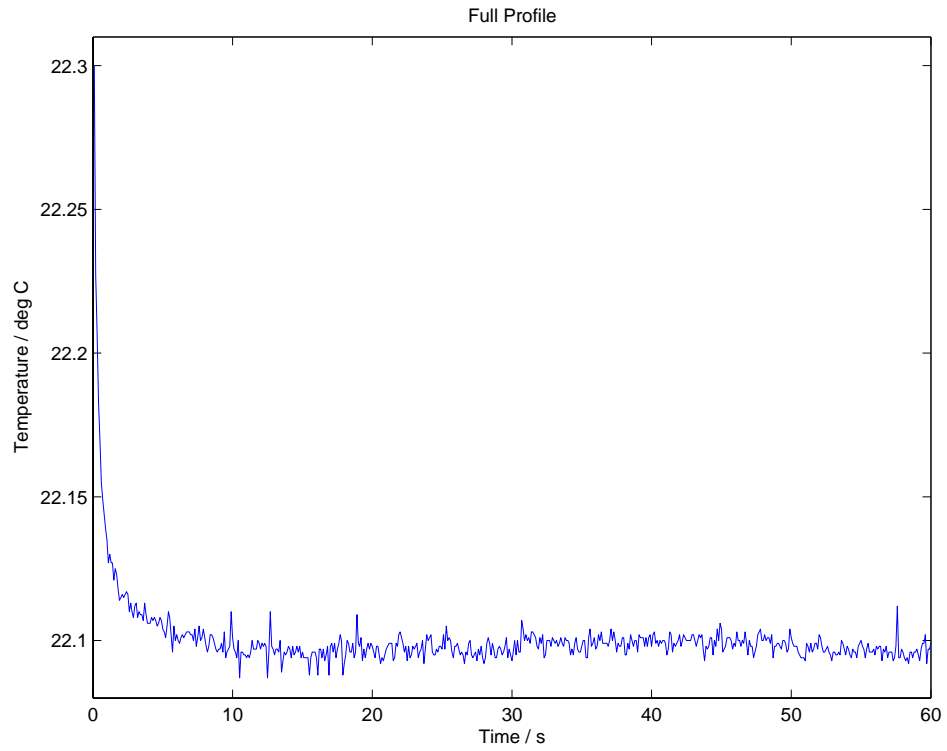


Figure 3-9. LCSR result of design B for good thermal contact

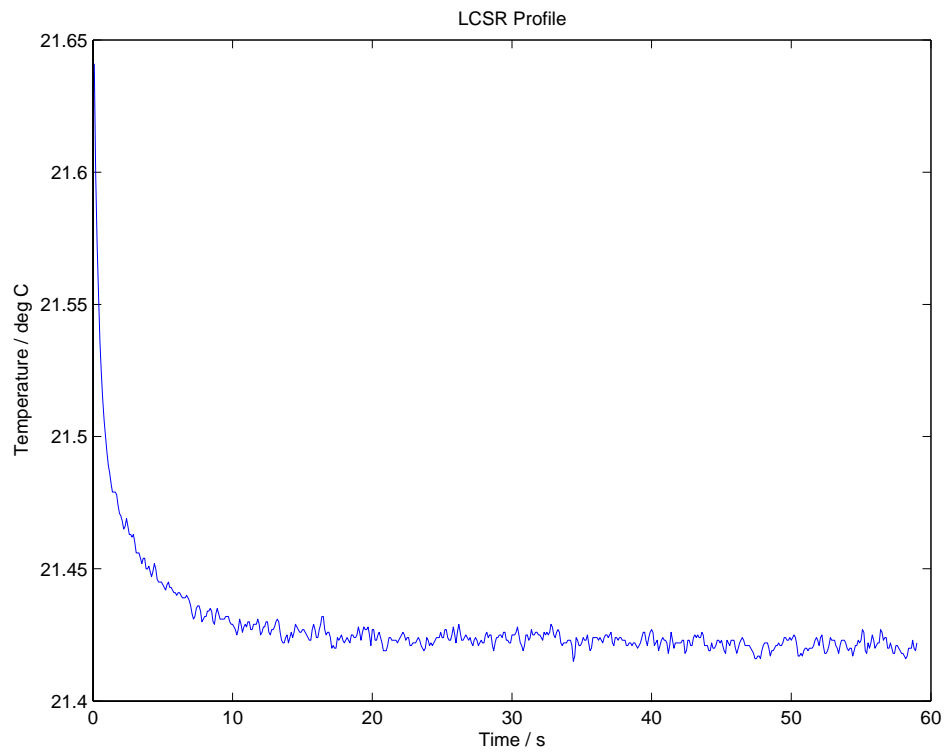


Figure 3-10 LCSR result of design B for poor thermal contact

The experimental results of this chapter demonstrate that the temperature measurement board modified according to design B is able to perform the LCSR test. A sufficiently large current can be injected into the RTD to induce a larger temperature change that is less likely to be affected by measurement noise and ambient temperature variations. However, due to hardware restrictions, this comes at the expense of being able to obtain high current temperature measurements.

Having shown that the measurement board is now able to perform the LCSR test to identify the sensor parameters, the next chapter will introduce the software compensation algorithm that seeks to improve the closed loop temperature control performance of the wafer.

## **CHAPTER 4**

### **AN ALGORITHM FOR IMPROVING MEASUREMENT ACCURACY**

Having successfully implemented the circuit for performing the LCSR test online, the sensor parameters can be identified in-situ. The LCSR test would capture all the factors that affect the sensor response characteristics and so the parameters identified should accurately reflect the actual conditions under which the PEB would be performed. In this chapter, an algorithm that aims at improving the measurement accuracy of the temperature measurement is proposed. The derivation of the algorithm is first shown. The need to cascade a filter with the algorithm is explained and the experimental effect of the filter demonstrated. The performance of a closed loop wafer temperature controller that utilized the feedback signals generated by the proposed algorithm is then presented.

#### **4.1 The Compensation Algorithm**

In Chapter 2, experimental results showing the impact of poor thermal contact on the performance of closed loop control is presented. A means of estimating the sensor parameters online is documented in Chapter 3. Accordingly, this section proposes an algorithm that seeks to alleviate the impact of varying amount of thermal contact on the quality of the feedback signal and, therefore, the closed loop control performance.

The algorithm for predicting the actual wafer temperature is based on the technique of estimating the input to a system by multiplying its output by the inverse transfer function. As shown in Chapter 2, the input-output relationship of the temperature measurement system, which utilizes a thin-film platinum RTD as the sensing element, can be modelled by the following first order transfer function [16] :

$$G(s) = \frac{T_m(s)}{T_a(s)} = \frac{K}{\tau s + 1} \quad (4.1)$$

where  $T_a(t)$  and  $T_m(t)$  are the actual and measured temperature respectively.  $K$  is the steady-state gain and  $\tau$  is the time constant of the RTD. An estimate of the wafer temperature,  $\hat{T}_a(t)$ , may be found via the following expression :

$$\hat{T}_a(t) = G^{-1}(s)T_m(s) = \frac{1}{\hat{K}} \left( \hat{\tau} s + 1 \right) T_m(t) \quad (4.2)$$

$\hat{K}$  and  $\hat{\tau}$  are, respectively, the steady-state gain and the sensor response time identified experimentally from the LCSR test. However,  $G^{-1}(s) = \frac{1}{\hat{K}} \left( \hat{\tau} s + 1 \right)$  is non-

causal and is the transfer function of a high pass filter. If Equation (4.2) is used to post-process the sensor output, high frequency noise in the feedback signal will be amplified. A solution to the problem is to cascade a low pass filter, whose transfer function is  $\frac{1}{\tau_f s + 1}$ , to  $G^{-1}(s)$ . Hence, the proposed compensation algorithm is of the

form  $\frac{\hat{\tau} s + 1}{\hat{K}(\tau_f s + 1)}$ . Figure 4-1 shows the functional block diagram of the temperature

measurement system and the proposed compensation system. The symbols represent :

- $T_a(t)$  Actual wafer temperature
- $T_a(k)$  Recovered wafer temperature
- $T_m(t)$  Output of temperature sensor
- $T_m(k)$  Sampled data from output of temperature sensor
- ZOH Zero-order hold
- $G(z)$  Transfer function of compensation algorithm with filter pole

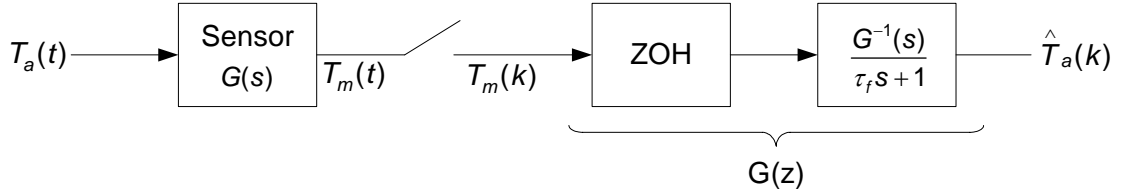


Figure 4-1. Functional block diagram of temperature measurement system

A point to note is that the compensation algorithm is defined in continuous-time domain. However, the output of the sensor,  $T_m(t)$ , is sampled by the signal conditioning chip and so the measurement data obtained is a discrete signal,  $T_m(k)$ . Thus, it is necessary to construct a continuous time signal by using the ZOH to hold the sampled value for the sampling period,  $h$ . The final expression for  $\hat{T}_a(k)$  is derived as follows.

$$\begin{aligned}
 G(z) &= \frac{\hat{T}_a(z)}{T_m(z)} \\
 &= (1 - z^{-1}) Z \left\{ \frac{G(s)}{s} \right\}
 \end{aligned} \tag{4.3}$$

and

$$\begin{aligned}
 \frac{G(s)}{s} &= \frac{1}{\hat{K}} \frac{\hat{\tau} s + 1}{s(\tau_f s + 1)} \\
 &= \frac{1}{\hat{K}} \left( \frac{1}{s} + \frac{\hat{\tau} - \tau_f}{\tau_f} \frac{1}{s + \frac{1}{\tau_f}} \right)
 \end{aligned} \tag{4.4}$$

Substituting Equation (4.4) into Equation (4.3),

$$\begin{aligned}
G(z) &= \frac{\hat{T}_a(z)}{T_m(z)} = (1-z^{-1})Z \left\{ \frac{1}{\hat{K}} \left( \frac{1}{s} + \frac{\hat{\tau}-\tau_f}{\tau_f} \frac{1}{s+\frac{1}{\tau_f}} \right) \right\} \\
&= \frac{1}{\hat{K}} \frac{z-1}{z} \left[ \frac{z}{z-1} + \frac{\hat{\tau}-\tau_f}{\tau_f} \frac{z-1}{z-e^{-\frac{h}{\tau_f}}} \right] \\
\frac{\hat{T}_a(z)}{T_m(z)} &= \frac{1}{\hat{K}} \left[ \frac{z-e^{-\frac{h}{\tau_f}} - \frac{\hat{\tau}-\tau_f}{\tau_f}}{z-e^{-\frac{h}{\tau_f}}} \right]
\end{aligned}$$

Cross multiplying and further evaluating, we have the final expression

$$\hat{T}_a(k) = e^{-\frac{h}{\tau_f}} \hat{T}_a(k-1) + \frac{1}{\hat{K}} \left[ \frac{\hat{\tau}}{\tau_f} T_m(k) - \left( e^{-\frac{h}{\tau_f}} + \frac{\hat{\tau}-\tau_f}{\tau_f} \right) T_m(k-1) \right] \quad (4.5)$$

Thus, an estimate of the measurand at the  $k$ th sample can be obtained using the  $k$ th and  $(k-1)$ th sample of the sensor output  $T_m(k)$  and  $T_m(k-1)$  respectively, together with the  $(k-1)$ th estimate of the wafer temperature  $\hat{T}_a(k-1)$ .

## 4.2 Experimental Results

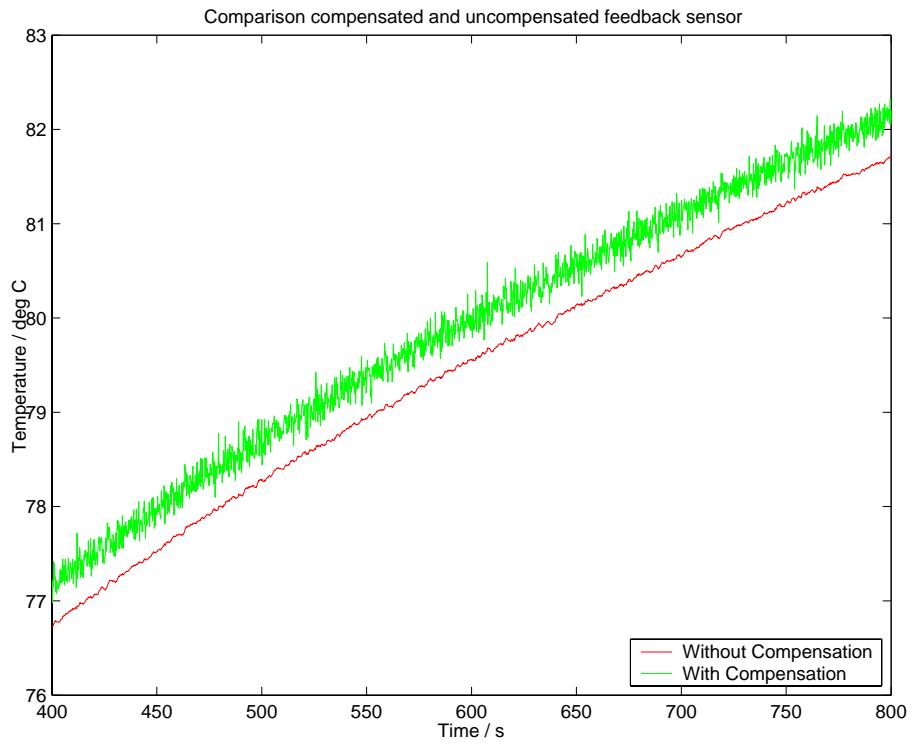
### 4.2.1 The Choice of Filter Pole

A unity gain first order low-pass filter,  $G_f(s) = \frac{1}{\tau_f s + 1}$ , was introduced in order to

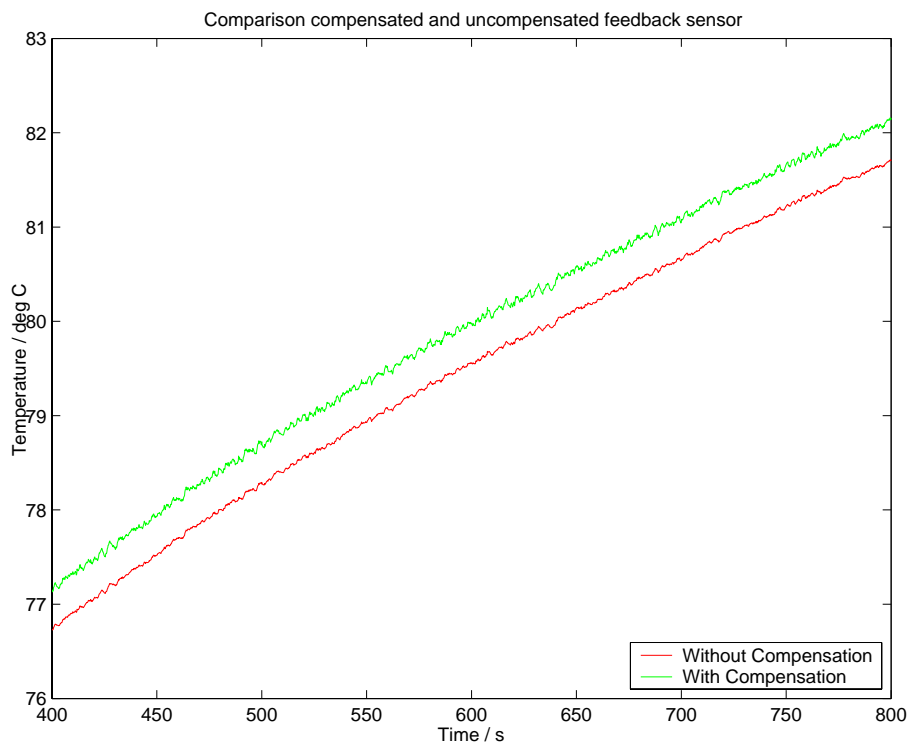
limit the amount by which the high frequency noise is amplified by the ideal inverse sensor transfer function,  $G^{-1}(s)$ . The trade-off is that  $G_f(s)$  will hinder the ability

of  $G^{-1}(s)$  to provide a good estimate of actual temperature on the wafer. Hence, the pole location of the low-pass filter must be selected with care. For simplicity,  $\tau_f$  is chosen as a fraction of the sensor response time derived from the LCSR test i.e.  $\tau_f = n\hat{\tau}$  where  $0 < n < 1$ . When  $n$  is small, the bandwidth of the filter is large so high frequency noise will be amplified by a larger gain, and vice versa.

Figure 4-2 shows the plots before and after the sensor outputs are processed by the compensation algorithm presented in Equation (4.5). The plots were generated using  $n=0$  and  $n=0.25$  respectively. The sampling time,  $h$ , is 0.25 seconds. It is clear from Figure 4-2(a) that the compensation algorithm will amplify noise if the low-pass filter is not employed. The results in Figure 4-2(b) demonstrate that the low pass-filter has successfully prevented high frequency noise amplification. Since the noise level in the software compensated signal is within the steady-state requirement of  $\pm 0.1^\circ\text{C}$ ,  $n$  is chosen as 0.25 and used to analyze the ability of the proposed strategy to minimize the impact of thermal contact level on the ability of the PI controller to regulate wafer temperature.



(a) Without filter



(b) With filter

Figure 4-2. Comparing measurement noise with and without filter

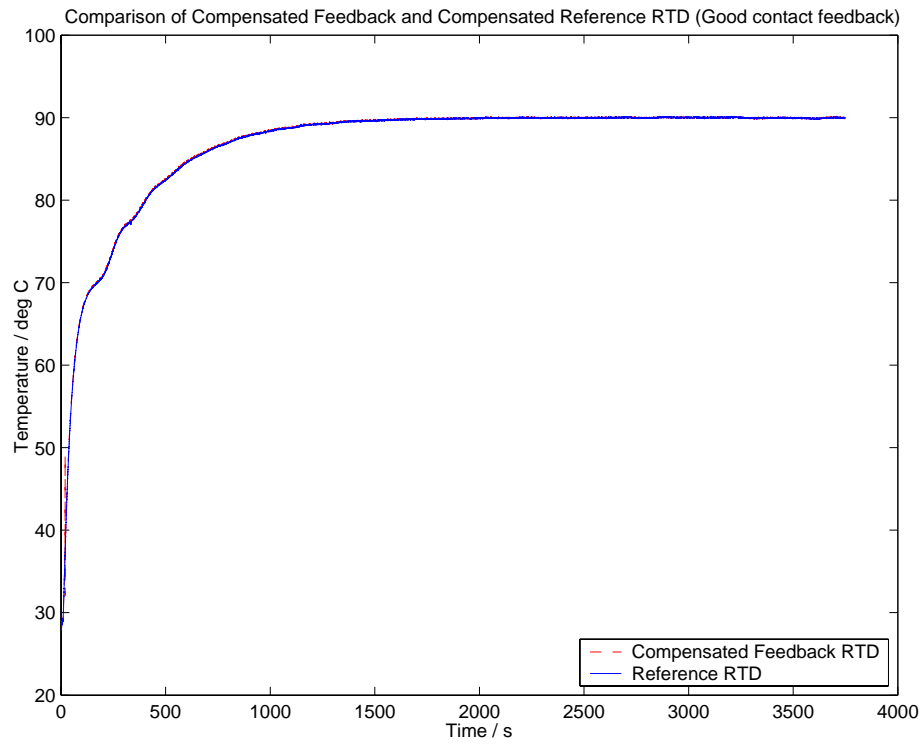
#### 4.2.2 The Closed Loop Performance

As in Section 2.4, the control problem is to heat the wafer from an ambient temperature of approximately 27°C to 90°C. The experimental procedures are the same. Two experiments were performed : one where the feedback signal was from the RTD that had good thermal contact with the wafer, and another in which the contact was poor. In both cases, the feedback signal received by the PI controller is processed through the compensation scheme. The PI controller parameters used were  $P = 10$  and  $I = 0.03$  and the sampling rate was 4Hz. A reference RTD was mounted beside the sensor that provides the feedback signal to obtain an indication of the wafer temperature. The sensor parameters identified via the LCSR test and the least-squares estimator, are tabulated in Table 4-1. The sampling time,  $h$ , is 0.25 seconds.

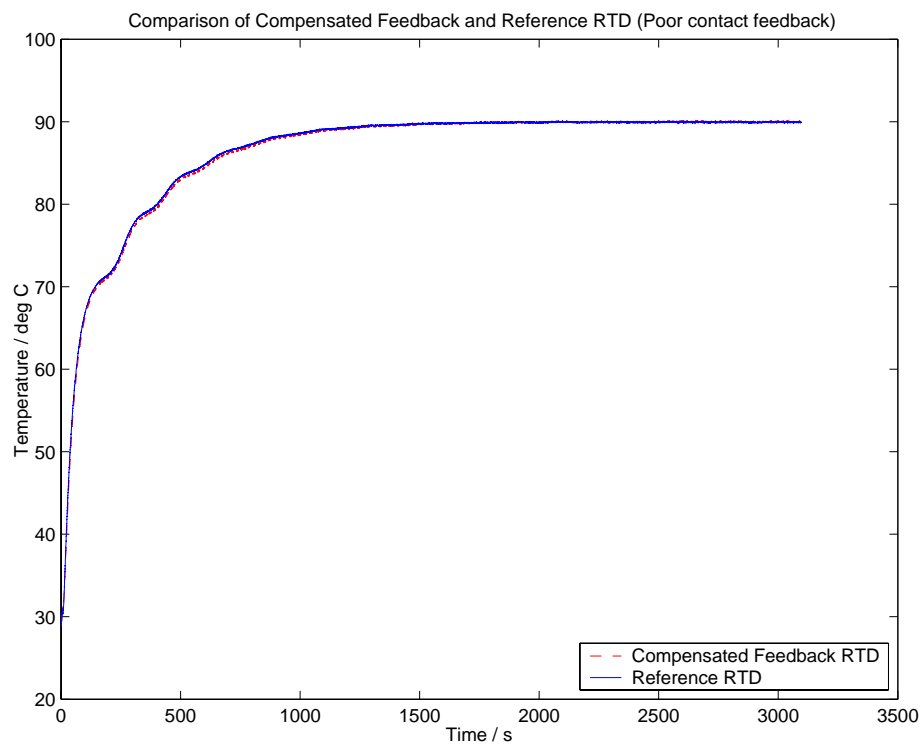
	$\hat{K}$	$\hat{\tau}$
Reference sensor	1	0.74
Feedback sensor (Good contact)	1	0.89
Feedback sensor (Poor contact)	1.0024	3.36

Table 4-1. The estimated sensor parameters

Figure 4-3 shows the feedback signals and the wafer temperature as measured by the reference sensor. Comparing Figure 2-11(a) and Figure 4-3(b), it can be observed that the difference between the output of the feedback and the reference sensor is significantly smaller and the step response is less oscillatory if the compensation algorithm is used to process the feedback signal. Furthermore, Figure 4-3 indicates that with the compensation algorithm in place, the behaviour of the temperature control system is less dependent on the sensor condition.



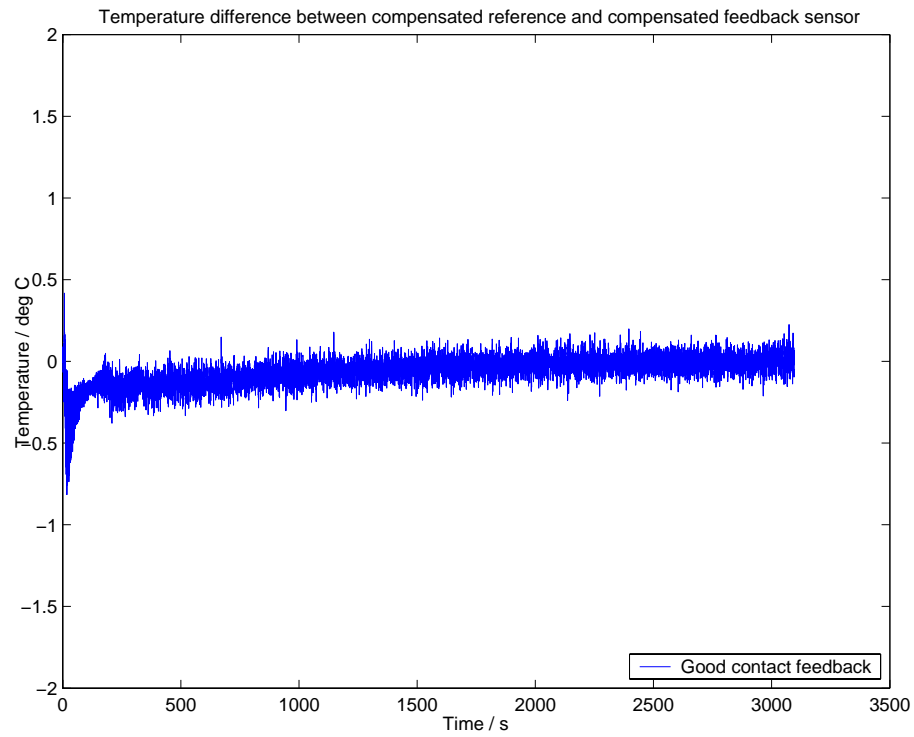
(a) Feedback sensor in good thermal contact with wafer



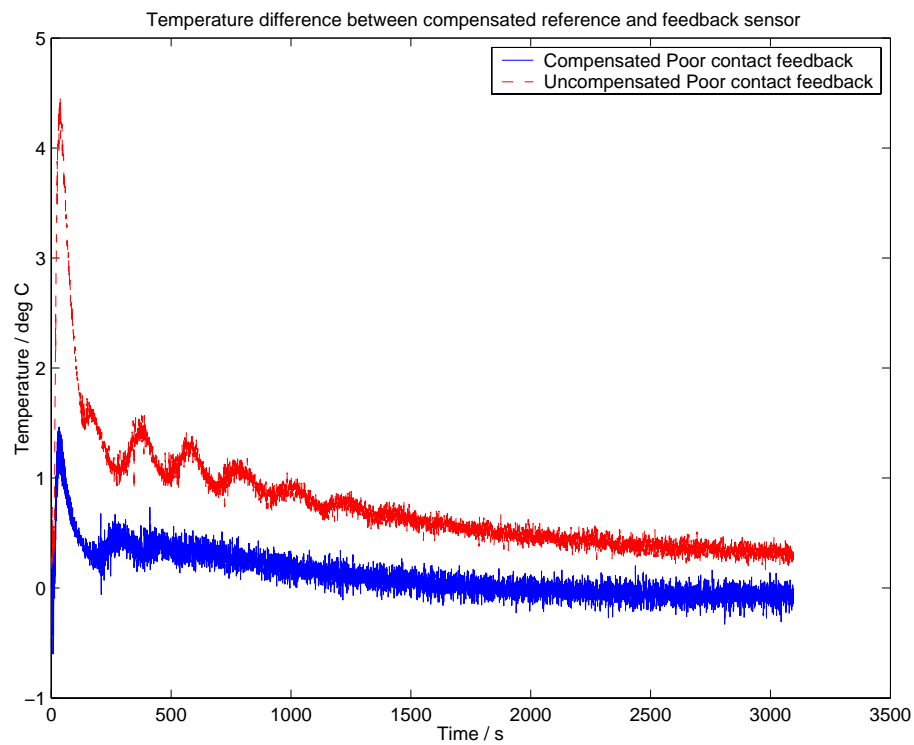
(b) Feedback sensor in poor thermal contact with wafer

Figure 4-3. Comparison of closed loop performance

In order to ascertain if the compensation algorithm is able to prevent poor thermal contact from hindering a multi-loop controller from achieving the desired spatial uniformity, the difference between the output of the reference sensor and the compensated feedback signal is shown in Figure 4-4. When the feedback sensor has relatively good contact with the wafer, the difference between the feedback and reference signal is within the desired accuracy of  $\pm 1^{\circ}\text{C}$  during transient and  $\pm 0.1^{\circ}\text{C}$  at steady-state. This is evident in Figure 4-4(a). For the case where the thermal contact of the feedback sensor is poor, the compensation algorithm reduced the maximum measurement error during transient by four times and eliminated the differences at steady-state. During the critical stage of the PEB process (wafer temperature is above  $60^{\circ}\text{C}$ ), the difference between the feedback and the reference sensor is less than  $1^{\circ}\text{C}$ . The results demonstrate that the proposed compensation algorithm may be used to reduce the adverse impact of poor thermal contact on the ability of a multi-zone closed-loop controller to maintain spatial uniformity across a wafer during the PEB process. Despite the promising results, the proposed algorithm faces several problems. In the next section, the limitations that may hinder a successful application in practice are described.



(a) Feedback sensor in good thermal contact with wafer



(b) Feedback sensor in poor thermal contact with wafer

Figure 4-4. Temperature difference between feedback and reference sensor

### 4.3 The Need for an Accurate Estimate of K

The sensor parameter estimation method based on the LCSR test has to be accurate, especially the estimation of  $K$ . The steady state temperature uniformity requirement of steady state error to be within  $\pm 0.1^\circ C$  leaves little room for error. For the desired temperature setpoint of  $90^\circ C$ , the maximum allowable error in the estimation of  $K$  is

$$\begin{aligned}\text{Max allowable error in } K &= \frac{\text{Max steady state error}}{\text{Steady state temperature}} \\ &= \frac{0.1}{90} \\ &= 0.00111\end{aligned}$$

The least-squares parameter estimation method is used to provide an estimate of the transfer function parameters from the transient profile data. However, the accuracy of the estimation is dependent on the ability of the data to faithfully capture all pertinent information about the temperature profile, ie. its initial value, the transient and the final value. If the data-logging begins after the instance when the current is returned to the normal state, only the first sample captures the rise in temperature induced by the LCSR test. Since the presence of noise is inevitable, it is likely that the first sample is corrupted. Consequently, the accuracy of the estimated sensor parameters would be adversely affected. This problem arises from the lack of readings during the first part of the LCSR test.

A solution would be to begin data-logging during the high current phase. The mean of the steady state samples during the high current phase data could be used as the initial value of the LCSR profile. Simulations were performed to demonstrate the effectiveness of this technique. The transfer function of the sensor was chosen as

$G(s) = \frac{1}{1.8s+1}$  to simulate a poor thermal contact case, where the time constant is greater. The sampling rate used was 10Hz and the step input change was  $-0.2^{\circ}\text{C}$ . Since thermal noise present in resistive elements has the characteristics of white noise [17] and the RTD is essentially a resistor, the noise model used in the simulation was band-limited white noise with zero mean. The power spectral density of the noise added was  $0.0002\text{W/rad/s}$  and was determined by a visual study of an LCSR profile obtained experimentally. Table 4-2 shows the estimation result. Without using the high current data, the estimation error for  $\hat{K}$  was 0.015, which is greater than the maximum allowable error at  $90^{\circ}\text{C}$ . With the high current data, the estimation error for  $\hat{K}$  was 0.0005 and is within the maximum allowable error. The simulation results indicate that the accuracy of  $\hat{K}$  can be improved if data recording was not suspended. However, the hardware restrictions highlighted in Chapter 3 resulted in the need to forsake the ability to obtain accurate high current readings in order to achieve a larger self-heating temperature change. The next chapter describes a method to work around the inability to obtain accurate high current readings so that a good estimate of  $K$  can still be obtained. It also introduces an algorithm that performs the LCSR test and the estimation of the sensor parameters during the PEB process. This alleviates the negative impact on wafer throughput if the LCSR test was performed before each wafer was processed.

	$\hat{K}$	$\hat{\tau} / \text{s}$
True value	1	1.8
Estimated value without high-current data	0.985	1.81
Estimated value with high-current data	0.9995	1.78

Table 4-2. Simulation results with and without high-current data

## **CHAPTER 5**

# **THE IN-SITU SENSOR PARAMETER IDENTIFICATION ALGORITHM**

Chapter 4 demonstrated that an algorithm that employs an inverse sensor model constructed via the LCSR test is able to improve measurement accuracy. However, performing the LCSR test prior to the PEB process takes away time from the fabrication process and reduces the throughput of wafers processed. One solution is to perform the LCSR test during the PEB process so that the wafer fabrication throughput is not affected. In this chapter, an algorithm is proposed that allows such an implementation. The LCSR test is performed during the PEB process and the data collected is processed through the least-square algorithm, yielding the sensor time constant and sensor gain. To overcome the inability to obtain accurate high current readings arising from the hardware restrictions, a workaround method to obtaining a good estimate of  $K$  is demonstrated.

### **5.1 Mathematical Derivation**

Figure 5-1 presents a block diagram that combines the temperature measurement process during PEB processing with the LCSR test, derived from the sensor model presented in section 3.1.1. The following assumptions are made :

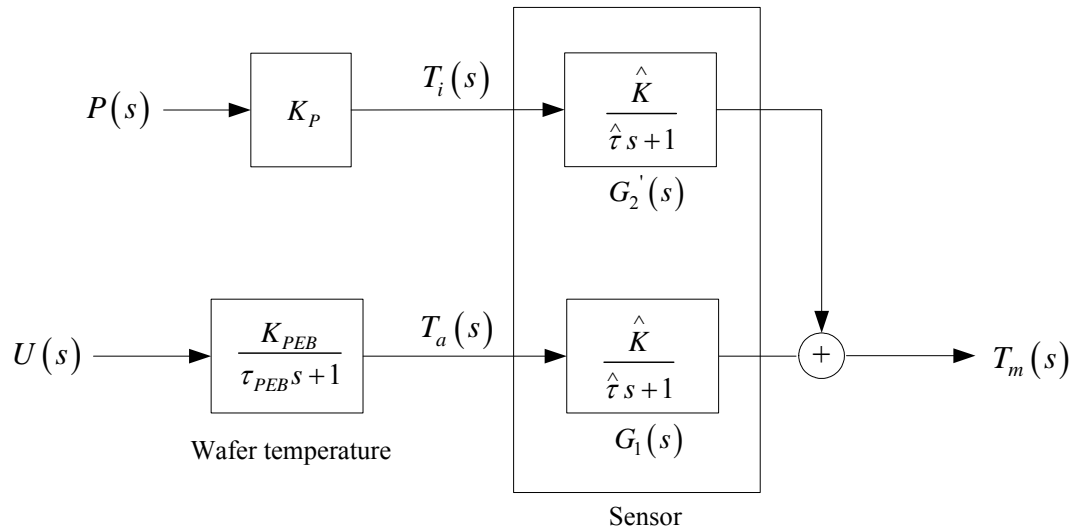
1. In the lower path, the thermal resistance of the protective sheath is negligible so that Equation (3.1) becomes the first-order transfer function

$$G_1(s) = \frac{T_m(s)}{T_a(s)} = \frac{\hat{K}}{\hat{\tau}s + 1}.$$

2. The thermal conversion transfer function of the upper path is first order so that Equation (3.2) becomes first-order system  $G_2'(s) = \frac{T_m(s)}{T_i(s)} = \frac{\hat{K}}{\hat{\tau}s + 1}$ .

$U(s)$  is the external heat source applied to heat the wafer and is modelled as a step input. The typical wafer temperature profile during PEB [2] is shown in Figure 5-2 and it is assumed that  $U(s)$  causes the wafer temperature to increase in a first-order manner ie.  $\frac{T_a(s)}{U(s)} = \frac{K_{PEB}}{\tau_{PEB}s + 1}$ . When the high current flowing through the RTD is

switched away, the electric power generated reduces and so  $P(s)$  is modelled as a negative step input. The self-heating in the RTD is reduced and this is manifested as a negative step change in temperature,  $T_i(s)$ . The RTD measures both these quantities ( $T_i(s)$  and  $T_a(s)$ ) and its output is  $T_m(t)$ . Defining the following symbols in Figure 5-1,



- $P(s)$  Electric power generated in the sensor. Modelled as a negative step input  
 $K_P$  Transfer function of electro-thermal conversion in sensor  
 $T_i(s)$  Temperature change due to reduction of self-heating. Modelled as a negative step input  
 $T_m(s)$  Measured temperature  
 $T_a(s)$  PEB wafer temperature  
 $\hat{\tau}$  Estimated sensor time constant  
 $\hat{K}$  Estimated sensor gain  
 $U(s)$  Temperature of heat source. Modelled as a step input  
 $K_{PEB}$  Post-exposure bake process gain  
 $\tau_{PEB}$  Post-exposure bake process time constant

Figure 5-1. Functional block diagram of temperature measurement

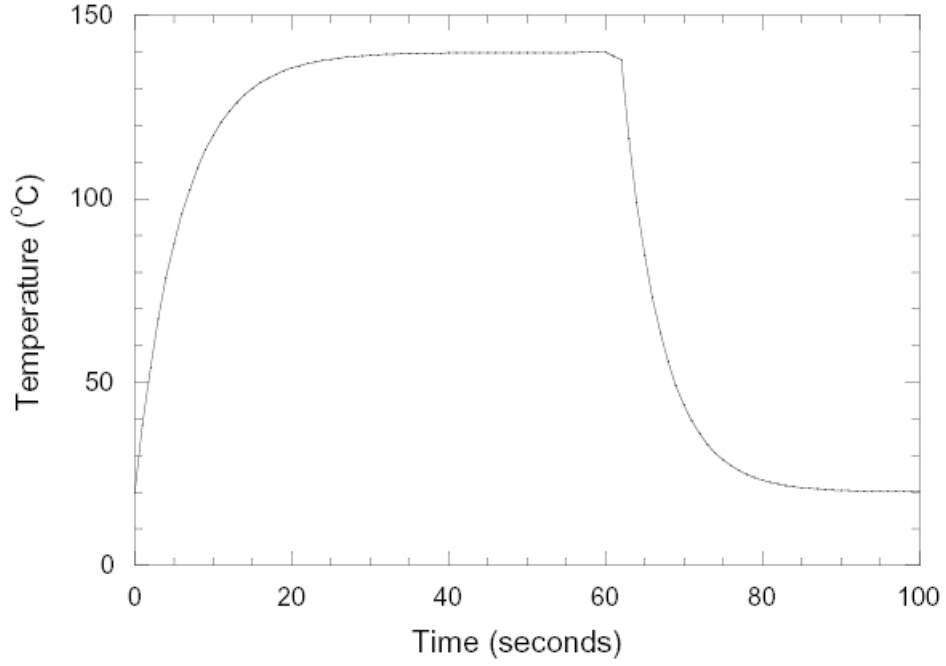


Figure 5-2. A typical wafer temperature profile during PEB [2]

From Figure 5-1,

$$T_m(s) = \frac{\hat{K} \cdot K_{PEB}}{(\hat{\tau}s + 1)(\tau_{PEB}s + 1)} U(s) + \frac{\hat{K}}{\hat{\tau}s + 1} T_i(s)$$

Cross-multiplying,

$$\begin{aligned} \left[ \tau_{PEB} \hat{\tau} s^2 + (\tau_{PEB} + \hat{\tau})s + 1 \right] T_m(s) &= K_{PEB} \hat{K} U(s) + \hat{K} (\tau_{PEB}s + 1) T_i(s) \\ \tau_{PEB} \hat{\tau} s^2 T_m(s) + (\tau_{PEB} + \hat{\tau})s T_m(s) + T_m(s) &= K_{PEB} \hat{K} U(s) + \hat{K} \tau_{PEB} s T_i(s) + \hat{K} T_i(s) \\ \tau_{PEB} \hat{\tau} s^2 T_m(s) &= -(\tau_{PEB} + \hat{\tau})s T_m(s) - T_m(s) + K_{PEB} \hat{K} U(s) + \hat{K} \tau_{PEB} s T_i(s) + \hat{K} T_i(s) \end{aligned}$$

From Figure 5-1,

$$\begin{aligned} T_i(s) &= K_p \cdot P(s) \\ &= K_p \cdot \left( -\frac{A_1}{s} \right) \end{aligned}$$

Let  $\Delta T = K_p A_1$  so that  $T_i(s) = -\frac{\Delta T}{s}$ . For  $U(s) = \frac{A_2}{s}$ ,

$$\begin{aligned}
\tau_{PEB} \hat{\tau} s^2 T_m(s) &= -(\tau_{PEB} + \hat{\tau}) s T_m(s) - T_m(s) + K_{PEB} \hat{K} \frac{A_2}{s} - \hat{K} \tau_{PEB} s \frac{\Delta T}{s} - \hat{K} \frac{\Delta T}{s} \\
T_m(s) &= -\frac{(\tau_{PEB} + \hat{\tau})}{\tau_{PEB} \hat{\tau}} \frac{1}{s} T_m(s) - \frac{1}{\tau_{PEB} \hat{\tau}} \frac{1}{s^2} T_m(s) + \frac{K_{PEB} \hat{K} A_2}{\tau_{PEB} \hat{\tau}} \frac{1}{s^3} - \frac{\hat{K} \Delta T}{\hat{\tau}} \frac{1}{s^2} - \frac{\hat{K} \Delta T}{\tau_{PEB} \hat{\tau}} \frac{1}{s^3} \\
&= -\frac{(\tau_{PEB} + \hat{\tau})}{\tau_{PEB} \hat{\tau}} \frac{1}{s} T_m(s) - \frac{1}{\tau_{PEB} \hat{\tau}} \frac{1}{s^2} T_m(s) + \left[ \frac{K_{PEB} \hat{K} A_2}{\tau_{PEB} \hat{\tau}} - \frac{\hat{K} \Delta T}{\tau_{PEB} \hat{\tau}} \right] \frac{1}{s^3} - \frac{\hat{K} \Delta T}{\hat{\tau}} \frac{1}{s^2}
\end{aligned}$$

Taking the inverse Laplace Transform,

$$T_m(t) = -\frac{(\tau_{PEB} + \hat{\tau})}{\tau_{PEB} \hat{\tau}} \int_0^t T_m(t) dt - \frac{1}{\tau_{PEB} \hat{\tau}} \int_0^t \int_0^t T_m(t) dt + \frac{1}{2} \frac{\hat{K}}{\tau_{PEB} \hat{\tau}} [K_{PEB} A_2 - \Delta T] t^2 - \frac{\hat{K} \Delta T}{\hat{\tau}} t$$

Let  $\hat{A} = K_{PEB} A_2$  and  $\hat{\tau}_{PEB} = \tau_{PEB}$  since both variables have to be estimated. In matrix form,

$$\begin{bmatrix} T_m(t_1) \\ T_m(t_2) \\ T_m(t_3) \\ \vdots \end{bmatrix} = \begin{bmatrix} t_1 & \int_0^{t_1} T_m(t) dt & t_1^2 & \int \int_0^{t_1} T_m(t) dt \\ t_2 & \int_0^{t_2} T_m(t) dt & t_2^2 & \int \int_0^{t_2} T_m(t) dt \\ t_3 & \int_0^{t_3} T_m(t) dt & t_3^2 & \int \int_0^{t_3} T_m(t) dt \\ \vdots & \vdots & \vdots & \vdots \end{bmatrix} \begin{bmatrix} -\frac{\hat{K} \Delta T}{\hat{\tau}} \\ -\frac{(\hat{\tau}_{PEB} + \hat{\tau})}{\hat{\tau}_{PEB} \hat{\tau}} \\ \frac{1}{2} \frac{\hat{K}}{\hat{\tau}_{PEB} \hat{\tau}} [\hat{A} - \Delta T] \\ -\frac{1}{\hat{\tau}_{PEB} \hat{\tau}} \end{bmatrix} \quad (5.1)$$

Like Equation (3.9), Equation (5.1) is linear-in-the-parameters. The coefficient vector can be found using the least-squares estimator. Once the coefficient vector has been identified, 4 equations can be formed to find the 4 unknown parameters. Let the 4 coefficients be  $d_1$ ,  $d_2$ ,  $d_3$  and  $d_4$  respectively. The 4 equations are thus :

$$-\frac{\hat{K} \Delta T}{\hat{\tau}} = d_1 \quad (5.2)$$

$$-\frac{(\hat{\tau}_{PEB} + \hat{\tau})}{\hat{\tau}_{PEB} \hat{\tau}} = d_2 \quad (5.3)$$

$$\frac{1}{2} \frac{\hat{K}}{\hat{\tau}_{PEB} \hat{\tau}} \left[ \hat{A} - \Delta T \right] = d_3 \quad (5.4)$$

$$-\frac{1}{\hat{\tau}_{PEB} \hat{\tau}} = d_4 \quad (5.5)$$

From Equation (5.3),

$$\hat{\tau}_{PEB} + \hat{\tau} = \frac{d_2}{d_4} \quad (5.6)$$

From Equation (5.5),

$$\hat{\tau}_{PEB} = \frac{1}{d_4 \hat{\tau}} \quad (5.7)$$

Substituting Equation (5.7) into Equation (5.6),

$$d_4 \hat{\tau}^2 - d_2 \hat{\tau} - 1 = 0 \quad (5.8)$$

Substituting values for  $d_2$  and  $d_4$  in Equation (5.8) and solving, the estimate of  $\hat{\tau}$  is obtained. Substituting  $\hat{\tau}$  back into Equation (5.7),  $\hat{\tau}_{PEB}$  is obtained.

From Equation (5.2),

$$\hat{K} = -\frac{d_1 \hat{\tau}}{\Delta T} \quad (5.9)$$

Here,  $\Delta T$  is not known, but can be determined separately. As described in section 3.1.2,  $\Delta T$  can be found via an LCSR test and a sensor that is in good thermal contact

with the wafer. When the sensor is in good thermal contact with the wafer,  $K$  can be assumed to be 1. Thus, this value of  $\Delta T$  serves as the magnitude of the temperature change induced by the self-heating in the RTD. With  $\Delta T$  and  $d_1$  known, and  $\hat{\tau}$  found earlier,  $\hat{K}$  can be calculated.

Finally, from Equation (5.4),

$$\hat{A} = \frac{2}{\hat{K}} \left( \frac{d_3}{d_4} \right) + \Delta T$$

With  $d_3$ ,  $d_4$  and  $\Delta T$  known, and  $\hat{K}$  found in Equation (5.9),  $\hat{A}$  can be calculated. In summary, the equations for calculating the PEB and sensor parameters are :

$$\text{Sensor time constant : } d_4 \hat{\tau}^2 - d_2 \hat{\tau} - 1 = 0$$

$$\text{Thermal contact gain : } \hat{K} = -\frac{d_1 \hat{\tau}}{\Delta T}$$

$$\text{PEB process time constant : } \hat{\tau}_{PEB} = \frac{1}{d_4 \hat{\tau}}$$

$$\text{Heat input and PEB process gain : } \hat{A} = \frac{2}{\hat{K}} \left( \frac{d_3}{d_4} \right) + \Delta T$$

Having shown parameter estimation algorithm and the calculations required to find the value of each parameter, the next step is to carry out simulations to determine the performance of the algorithm.

## 5.2 Simulation Results

A Matlab/Simulink simulation program was first written to verify the viability of the parameter estimation algorithm. The sequence of events is as follows :

1. With the wafer at room temperature, the high current is switched into the temperature sensor, modelled as  $G(s) = \frac{1}{0.6s+1}$ . This causes self-heating in the sensor and the measured temperature rises to a steady state value as a consequence.
2. Once the rise in temperature due to the increase in amount of self-heating has stabilized, the PEB process, modelled as  $\frac{T_a(s)}{U(s)} = \frac{1}{60s+1}$  and  $U(s) = 83^\circ\text{C}$ , is activated and the excitation current is returned to its nominal value. Logging of wafer temperature data begins. The amount of electrical power generated decreases at the same time that wafer temperature rises due to the PEB ramp. The LCSR test results shown in Chapter 4 indicate that the temperature change when the RTD current increases from  $200\mu\text{A}$  to about  $1.1\text{mA}$  is approximately  $0.2^\circ\text{C}$ . Hence,  $\Delta T$  was set at  $0.2^\circ\text{C}$  in the simulation programme.
3. After a pre-defined duration, data logging is stopped. The data is processed by the estimation algorithm and the sensor parameters obtained.

The simulation results are presented in Figure 5-3. The lower pane shows that the current flowing through the temperature sensor is switched back to the nominal value at  $t = 10\text{s}$ , reducing the amount of self-heating.

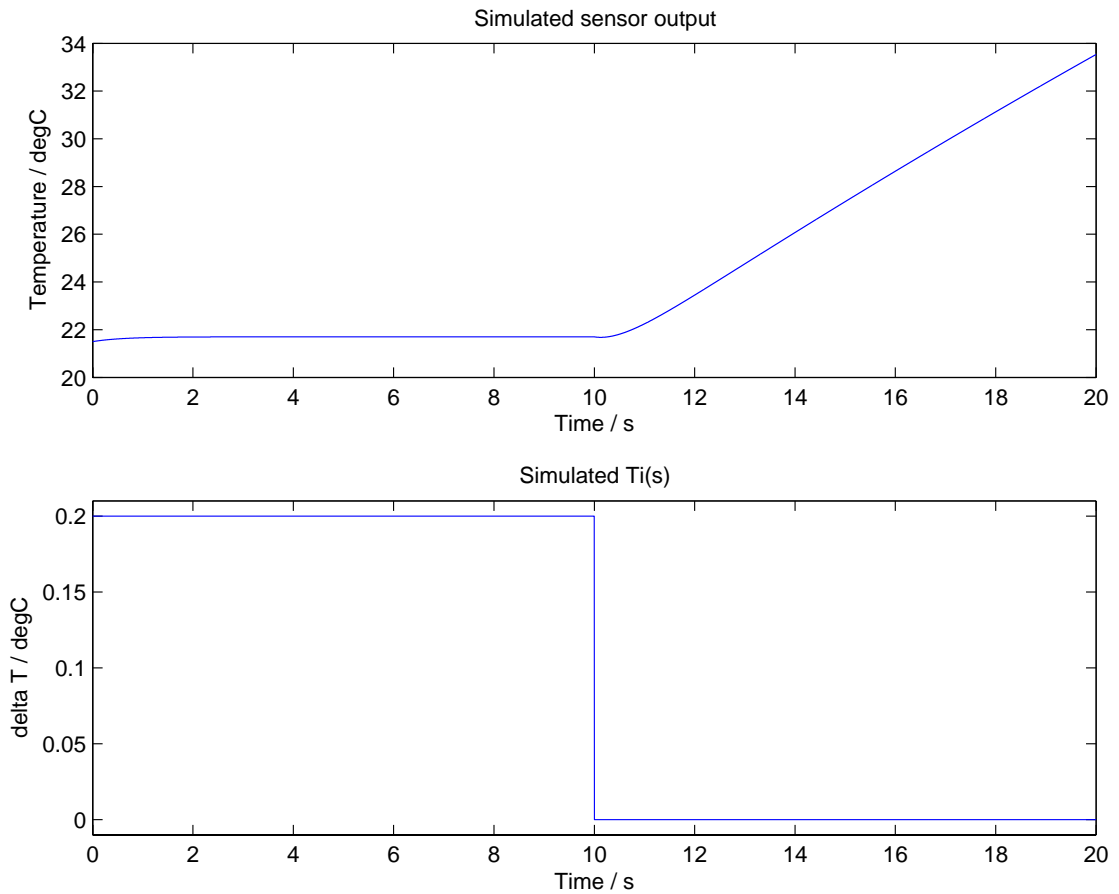


Figure 5-3. Illustration of high current and PEB temperature ramp

Figure 5-4 focuses on the initial wafer temperature rise of the simulation. The LCSR test and the wafer temperature was logged immediately when the PEB ramp was activated, for a duration of 10s. Figure 5-4(a) shows the 10s of the simulation when the LCSR test was running. Figure 5-4(b), which focuses on the first second after the high current was switched off at  $t = 10s$ , shows that the measured temperature decays initially even though the wafer is being heated. This behaviour occurred because the electrical power generated internally decreases when the current flowing through the RTD is reduced to its nominal value. Since  $\tau < \tau_{PEB}$ , the rate of decay in sensor output brought about by the drop in the RTD excitation current is faster than the increase in wafer temperature due to the applied heat.

The coefficients to be found are :

$$\theta = \begin{bmatrix} -\frac{\hat{K} \Delta T}{\hat{\tau}} \\ -\frac{(\hat{\tau}_{PEB} + \hat{\tau})}{\hat{\tau}_{PEB} \hat{\tau}} \\ \frac{1}{2} \frac{\hat{K}}{\hat{\tau}_{PEB} \hat{\tau}} \left[ \hat{A} - \Delta T \right] \\ -\frac{1}{\hat{\tau}_{PEB} \hat{\tau}} \end{bmatrix}$$

Using the data and the least-squares estimator, the coefficients were identified and compared with their ideal values in Table 5-1 .

	$-\frac{\hat{K} \Delta T}{\hat{\tau}}$	$-\frac{(\hat{\tau}_{PEB} + \hat{\tau})}{\hat{\tau}_{PEB} \hat{\tau}}$	$\frac{1}{2} \frac{\hat{K}}{\hat{\tau}_{PEB} \hat{\tau}} \left[ \hat{A} - \Delta T \right]$	$-\frac{1}{\hat{\tau}_{PEB} \hat{\tau}}$
Actual value	-0.33333	-1.6833	1.1556	-0.027778
Estimated value	-0.33124	-1.679	1.147	-0.027709

Table 5-1. The estimated coefficients from simulation

From the coefficients in Table 5-1, the sensor parameters were calculated. Table 5-2 compares the actual and the estimated sensor and PEB process parameters.

	$\hat{\tau}$	$\hat{K}$	$\hat{\tau}_{PEB}$	$\hat{A}$
True value	0.6	1	60	83
Estimated value	0.60157	0.99631	59.993	82.991

Table 5-2. The estimated parameters from simulation

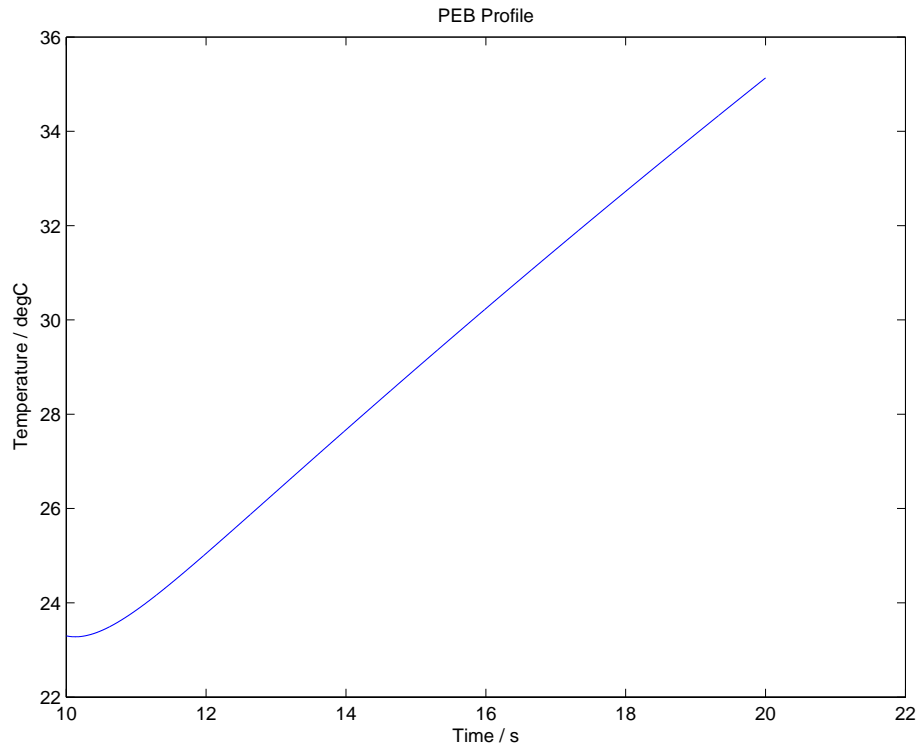
It is evident from Table 5-2 that the estimation algorithm performs well and is able to accurately identify the sensor parameters.

To further check that the algorithm is able to perform well under experimental conditions, measurement noise was added to the simulation model. Since the RTD is a resistive element, the noise model used was the band-limited white noise model from Simulink [17]. The power spectral density of the noise added was 0.002W/rad/s and was determined by a visual study of a similar temperature rise profile obtained experimentally. Table 5-3 compares the estimation results. Figure 5-5 shows the first 10s of the simulated wafer temperature profile.

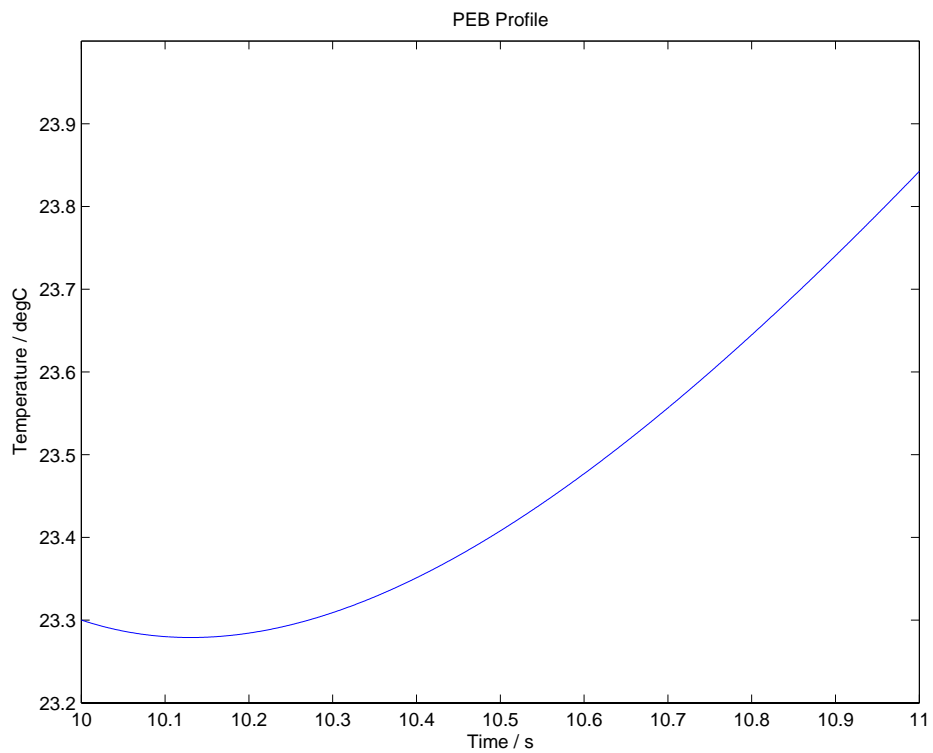
	$\hat{\tau}$	$\hat{K}$	$\hat{\tau}_{PEB}$	$\hat{A}$
Actual value	0.6	1	60	83
Estimated value	0.64624	0.82828	50.954	86.695

Table 5-3. The estimated parameters from simulation with noise added

Though the estimates  $\hat{\tau}_{PEB}$  and  $\hat{A}$  have been significantly affected by measurement noise, the parameters of primary interest,  $\hat{\tau}$  and  $\hat{K}$ , were still close to their actual values. This could be a consequence of the measurement data used for the parameter estimation, which fully captures the LCSR profile but does not capture the steady state of the PEB process.



(a) Simulation wafer temperature profile over the first 10s of PEB ramp



(b) Simulation result, zooming in on the first second of wafer temperature ramp

Figure 5-4. Simulation results of parameter estimation algorithm

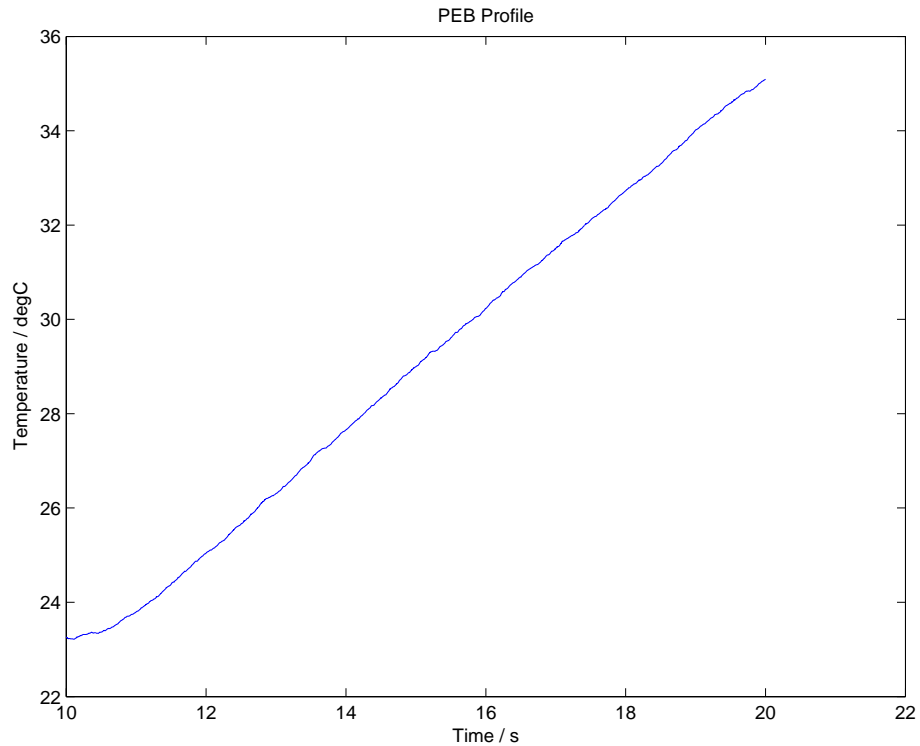


Figure 5-5. Simulation wafer temperature profile over the first 10s of PEB ramp with noise added

### 5.3 Caveat

In Section 5.2, Table 5-2 showed that if the data logging and high current switching coincided exactly with the start of the PEB process, the estimated parameters were very close to the true values. However, it is difficult to synchronize the high current switch-over exactly with the start of PEB process. The presence of an air-gap between the heater and the wafer results in a short delay between the instance when heat is applied and when the wafer temperature begins rising. This section aims to investigate the effect of a delay between the instant when current is switched to the nominal level and the start of the PEB process.

Delays of 0.5s and 1.0s were used to highlight the effect of a failure to synchronize the start of the data logging and PEB ramp. Figure 5-6 illustrates a 0.5s difference between the start of the PEB process and the start of data logging. Table 5-4 compares the estimates obtained without measurement noise.

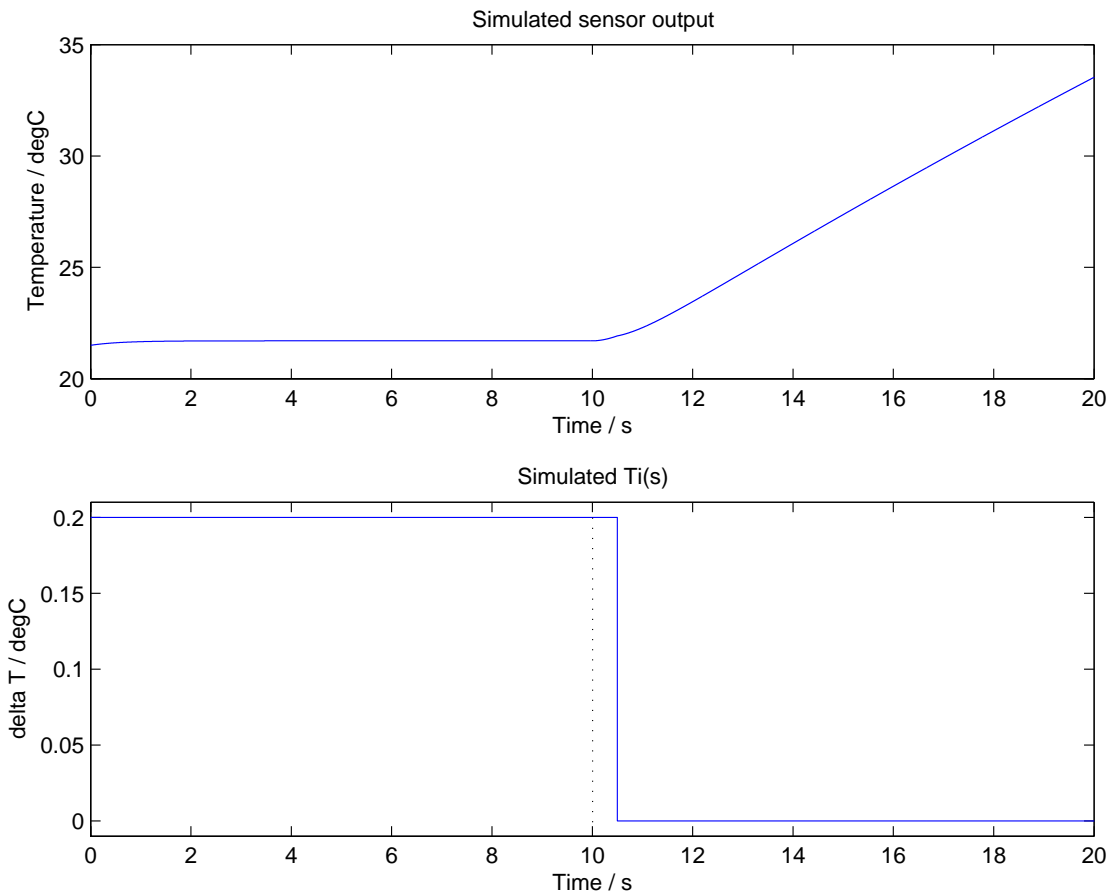


Figure 5-6. Illustration of a 0.5s delay in starting data logging

	$\hat{\tau}$	$\hat{K}$	$\hat{\tau}_{PEB}$	$\hat{A}$
Actual value	0.6	1	60	83
Estimated value (no delay)	0.60157	0.996	59.993	82.991
Estimated value (0.5s delay)	0.6017	-1.344	59.993	-61.245
Estimated value (1.0s delay)	0.6019	-2.342	59.993	-34.847

Table 5-4. Variation of estimates with delay in measurement

Though the impact of the delay on the estimated value of  $\tau$  is minimal,  $\hat{K}$  is incorrect, even in the absence of measurement noise. Not surprisingly, the effect of the delay on the parameter estimates is exacerbated in the presence of measurement noise, as Table 5-5 shows.

	$\hat{\tau}$	$\hat{K}$	$\hat{\tau}_{PEB}$	$\hat{A}$
Actual value	0.6	1	60	83
Estimated value (no delay)	0.646	0.828	50.954	86.695
Estimated value (0.5s delay)	0.653	-1.59	49.297	-43.480
Estimated value (1.0s delay)	0.730	-3.122	47.159	-21.003

Table 5-5. Variation of estimates with delay in measurement, in the presence of measurement noise

For a delay of 0.5s, the estimates of  $\tau$  is still reasonable but the estimate for  $K$  is incorrect. For a delay of 1.0s, the estimates of  $\tau$  is further from the actual value but the estimate for  $K$  deteriorates much further. For the proposed algorithm to work in practice, it is necessary to ascertain the extent to which the error in the estimated value of  $\tau$  affects the closed loop control performance.

The study was carried out by assuming that the actual sensor time constant was  $\tau = 0.6s$  whilst the identified sensor time constant was  $\hat{\tau} = 0.73s$  (for a measurement delay of 1.0s in Table 5-5). Since the algorithm would be used in closed loop wafer temperature control, a closed loop control simulation was chosen. The parameters of the PI controller were  $P = 10$  and  $I = 0.03$  and the PEB process model was chosen to be  $\frac{T_a(s)}{U(s)} = \frac{1}{150s+1}$  (Figure 5-1) and  $U(s) = 68^\circ C$ . The simulation sampling rate

was 4Hz and the noise model used was the same as for the results in Table 5-5. The filter pole of the compensation algorithm described in section 4.2.1 was chosen to be

$$\tau_f = 0.25 \hat{\tau}.$$

Figure 5-7 shows the simulated dynamic response of the closed loop performance. The blue plot represents the simulated wafer temperature and the green plot is the predicted temperature (ie. the output from the RTD that has been processed through the compensation algorithm). Figure 5-8 shows the temperature difference between the blue and green plots. The largest temperature difference is about  $0.5^{\circ}\text{C}$  and is within the requirement of  $\pm 1^{\circ}\text{C}$  during transient. The steady state difference is about  $0.005^{\circ}\text{C}$  and within the steady state requirement of  $\pm 0.1^{\circ}\text{C}$ . Thus, the identified time constant of 0.73s is acceptable. Having shown that the sensor time constant can be estimated, the next section investigates a method to determine the estimate of  $K$  using the identified sensor time constant.

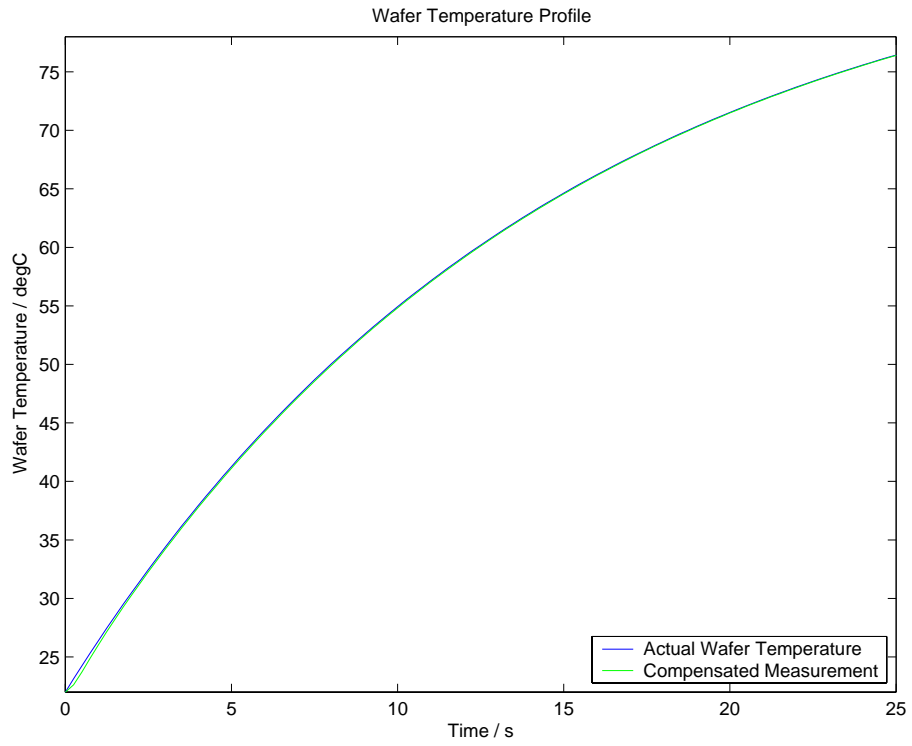


Figure 5-7. Dynamic response of closed loop performance simulation

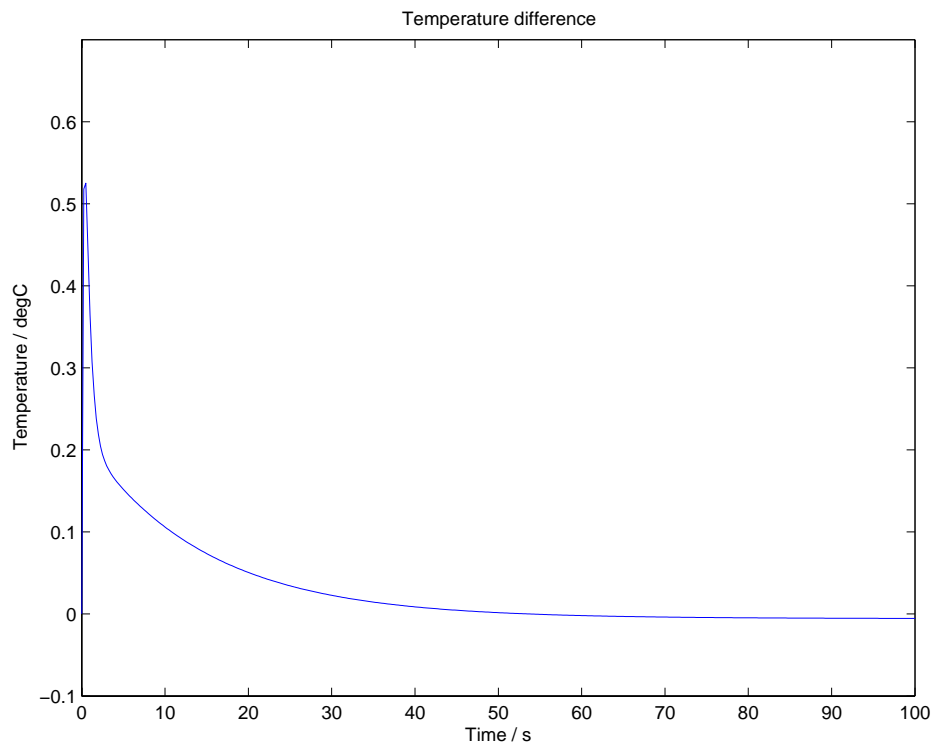


Figure 5-8. Temperature difference between actual and compensated readings for  $\hat{\tau} = 0.73s$

## 5.4 Relationship between $K$ and $\tau$

In order for  $K$  to be reliably identified, a method that ensures  $K$  is not affected by the synchronization of the current switching and PEB temperature ramp is needed. In section 5.3, it was shown that  $\tau$  can be reasonably estimated even in the presence of synchronization errors and measurement noise. Thus, one possible method is to use  $\tau$  to find  $K$ . By first experimentally determining the relation between  $K$  and  $\tau$ , the estimate of  $\tau$  can be used to identify  $K$ .

### 5.4.1 The Experimental Results

To obtain the experimental data, two sensors were attached to the wafer : one serving as a *reference sensor* that is always in good thermal contact with the wafer; the other as the *measurement sensor* with varying levels of thermal contact with the wafer. Good thermal contact between the sensor and wafer was achieved by applying liberal amounts of thermal paste. Poor thermal contact was achieved by covering the contact surface of the sensor with tape to varying extents. For the measurement sensor, each level of thermal contact corresponded to a certain value of  $\tau$ . This value of  $\tau$  can be determined using the LCSR test. Having determined  $\tau$ , the wafer was then heated under open loop to a steady state temperature of around 90°C. The ratio of the reference sensor reading over the measurement sensor reading at steady state is the steady state gain, or  $K$ , of the sensor transfer function when thermal contact is poor. Repeating the experiment for different levels of thermal contact, Table 5-6 shows the corresponding  $\tau$  and  $K$  values obtained. The relation between them can be determined using least-squares curve fitting to the general second-order equation  $K = a\tau^2 + b\tau + c$ , as shown in Figure 5-9. The equation of the best-fit curve is

$$K = 0.00042937\tau^2 + 0.0010961\tau + 0.99906$$

With this information, the estimation algorithm can be used to find  $\tau$ , and from which  $K$  can subsequently be found.

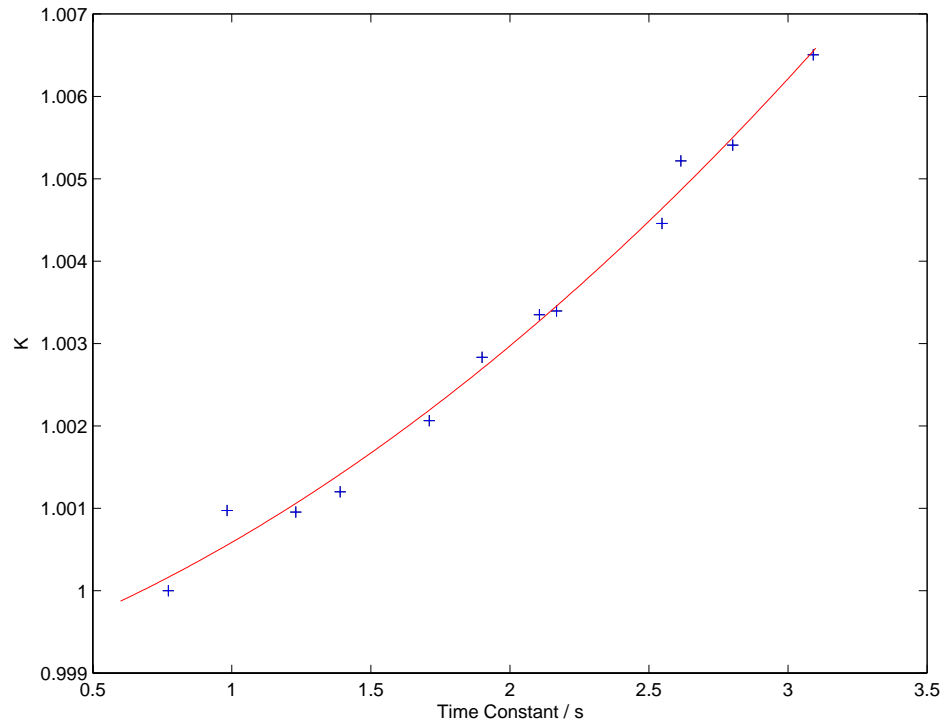


Figure 5-9. Best fit line representing relation between  $\tau$  and  $K$

$\tau / s$	$K$	$\tau / s$	$K$
0.772	1	2.106	1.00335
0.983	1.000973	2.168	1.00400
1.23	1.000955	2.547	1.00446
1.39	1.00120	2.615	1.00522
1.71	1.002064	2.801	1.00541
1.90	1.00283	3.091	1.00651

Table 5-6. Corresponding values of  $\tau$  and  $K$

Having identified a relationship between  $\tau$  and  $K$ , the next step is to put the proposed algorithm using an experimental setup.

## 5.5 Experimental Results

To test the performance of the algorithm under actual experimental conditions, the experimental procedure is as follows :

1. The heaters are first maintained at a steady state temperature of 125°C. The wafer is left at room temperature.
2. The high current of 1.1mA is switched into the temperature sensor. For the duration of the high current, the readings from the sensor are not logged.
3. The wafer is then loaded into the bake-chill machine.
4. After about 15s, the heaters are lowered. As the heaters are nearing their fully lowered positions, the cardboards are quickly removed.
5. The current is then switched back to its nominal value. The Labview program has been written to start the data logging once the RTD excitation current is switched to its nominal level.
6. After the sensor parameters have been identified, these are then passed to the compensation algorithm. The Labview program then switches to closed-loop temperature control of the wafer and activates the compensation algorithm.
7. The wafer temperature is then heated up to and maintained at 90°C .

As with the experiments in section 4.2.2, two sets of experiments were performed : one where the feedback signal was from the RTD that had good thermal contact with the wafer, and another in which the contact was poor. In both cases, the feedback signal received by the PI controller is processed through the compensation scheme. The PI controller parameters used were  $P = 10$  and  $I = 0.05$ . A reference RTD was mounted beside the poor contact sensor to obtain an indication of the wafer temperature.

### 5.5.1 Good Thermal Contact

Figure 5-11 shows the first 10s of the experiment for a temperature sensor with good thermal contact. The high current duration was about 20s (not shown in Figure 5-11) and the nominal current duration was 10s; the sampling rate was chosen to be 10Hz in order to capture the dynamics of the LCSR profile. For the duration of the LCSR test, the heater temperature was maintained at 125°C i.e. applied heat remains constant. This is to achieve a faster wafer temperature rise time. After switching to closed-loop temperature control, the sampling rate was changed to 4Hz since the dynamics of the PEB process is slower than the LCSR test. This reduces the amount of measurement noise in the data. Using the proposed algorithm, the identified parameters are shown in Table 5-7.  $\hat{K}$  was determined using the relation between  $\tau$  and  $K$  proposed in section 5.4.

$\hat{\tau}$	$\hat{K}$	$\hat{\tau}_{PEB}$	$\hat{A}$
0.819	1.0002	145.9	144.2

Table 5-7. The identified parameters for a sensor with good thermal contact

From the experimental data presented in section 5.4.1, the time constant and gain of a sensor that has good contact with the wafer is 0.772s and 1 respectively. Thus, the estimated value of  $\tau$  is close to the value obtained when wafer temperature is constant and  $\hat{K}$  is within the allowable estimation error noted in section 4.3.

Since  $\hat{\tau}_{PEB}$  and  $\hat{A}$  are affected by a synchronization error between the high current switching and the start of the PEB process, there is a need to verify the identified

parameters. To do this, a simulation was used to compare the experimental profile with the temperature rise profile obtained from a simulation model constructed using the identified PEB parameters. This is depicted in Figure 5-10.

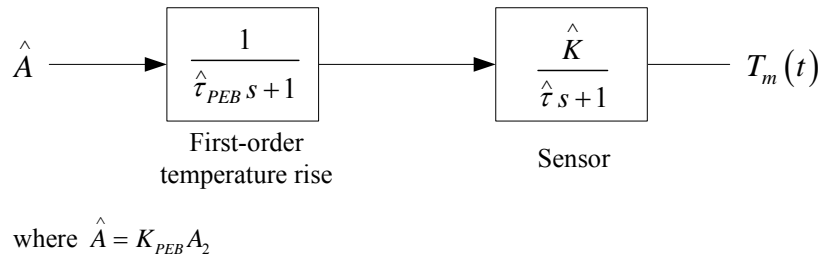


Figure 5-10. Functional block diagram of simulation to generate PEB temperature rise

Since the experimental result of Figure 5-11 was for a good thermal contact sensor, the results in Table 5-7 were used as the simulation parameters. The resulting data was then plotted together with the experimental data.

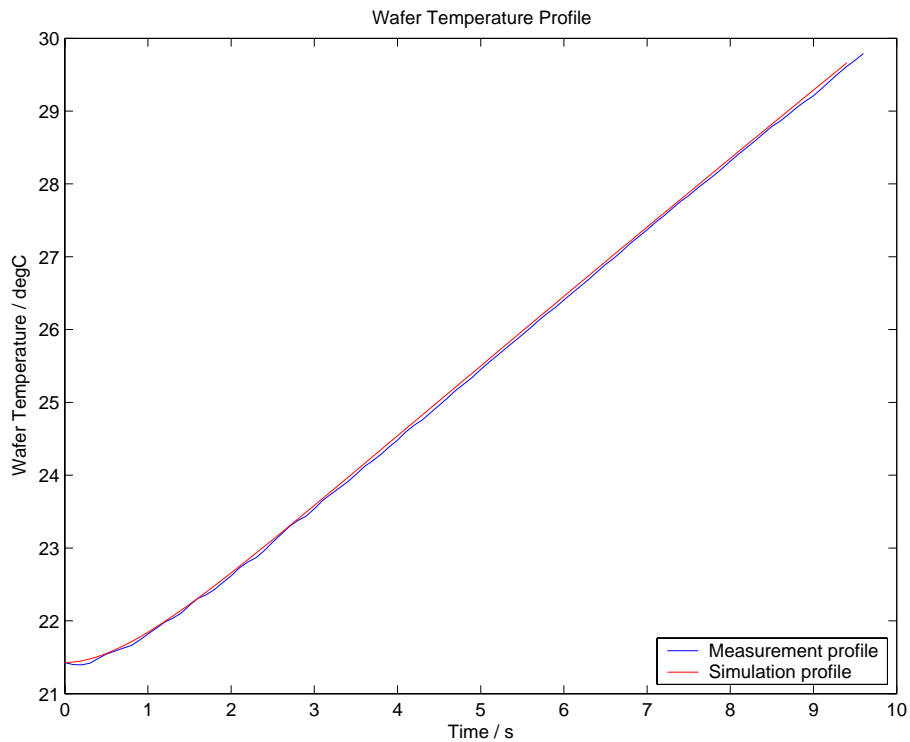


Figure 5-11. Experimental result of LCSR test with wafer heating for sensor with good thermal contact

Figure 5-11 clearly shows the closeness of the fit of the actual PEB profile to the simulated profile. Thus, the estimation algorithm can be used to determine the sensor parameters during the PEB process.

After the sensor parameters had been identified, the Labview program automatically switches to closed loop temperature control of the wafer with the compensation algorithm active. Figure 5-12 plots the compensated measurement sensor signal (blue) with the compensated reference sensor signal (black). Figure 5-13 plots the difference between the readings of the two channels. The filter pole of the compensation algorithm was chosen to be  $\tau_f = 0.25\hat{\tau}$ , for the measurement sensor and  $\tau_f = 0.75\hat{\tau}$  for the reference sensor. The filter bandwidth used for the reference channel is smaller because the reference channel had greater measurement noise due to the hardware modifications. The filter pole was therefore chosen to reduce noise in the compensated reference channel measurements to the same level as the measurement channel.

The critical temperature for the PEB process is above 60°C and was crossed about 58s into the experiment (see Figure 5-12). In Figure 5-13, the temperature difference between the sensors fell to within  $\pm 1^\circ\text{C}$  about 26s into the experiment and finally to within  $\pm 0.1^\circ\text{C}$  at steady state. Thus, the compensation algorithm was able to reduce measurement error to within  $\pm 1^\circ\text{C}$  during the critical stage of the PEB process and to within  $\pm 0.1^\circ\text{C}$  at steady state. The largest temperature difference in Figure 5-13 is greater than Figure 4-4(a) (good thermal contact results of section 4.2.2). This is because the estimates  $\hat{\tau}$  and  $\hat{K}$  used in the compensation algorithm in section 4.2.2

were obtained in a separate LCSR test without ambient temperature drift and are more accurate indicators of the sensor response characteristics. They are not subject to the synchronization errors that may occur in the experiments for this section. Thus, it may be expected that the closed loop temperature control performance of the compensation algorithm will be better in section 4.2.2.

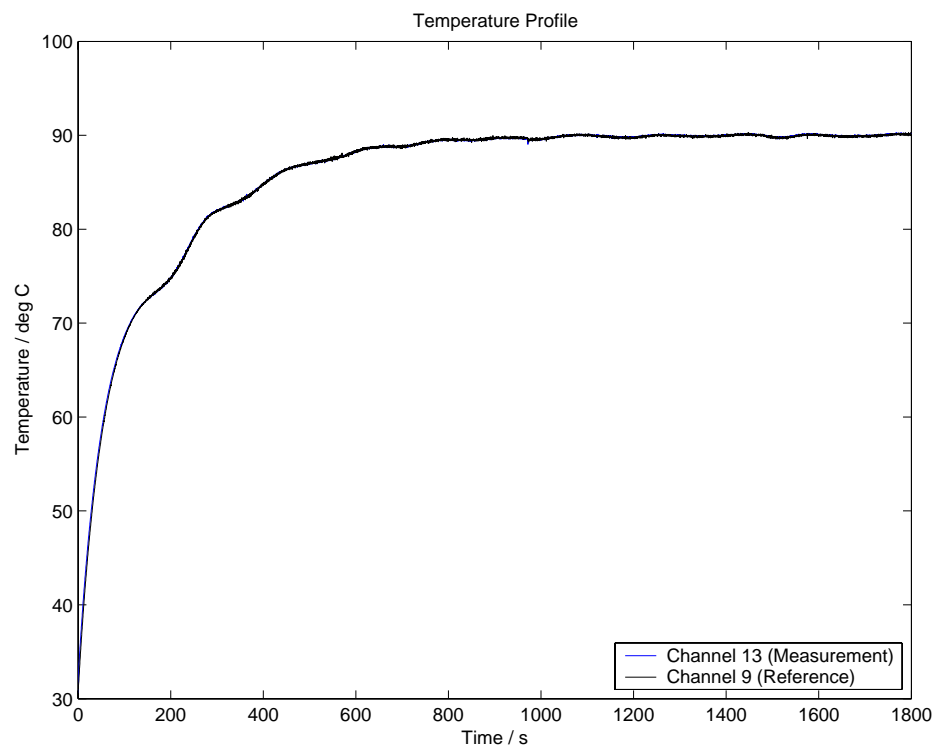


Figure 5-12. Experimental result of closed loop control with compensation for sensor with good thermal contact

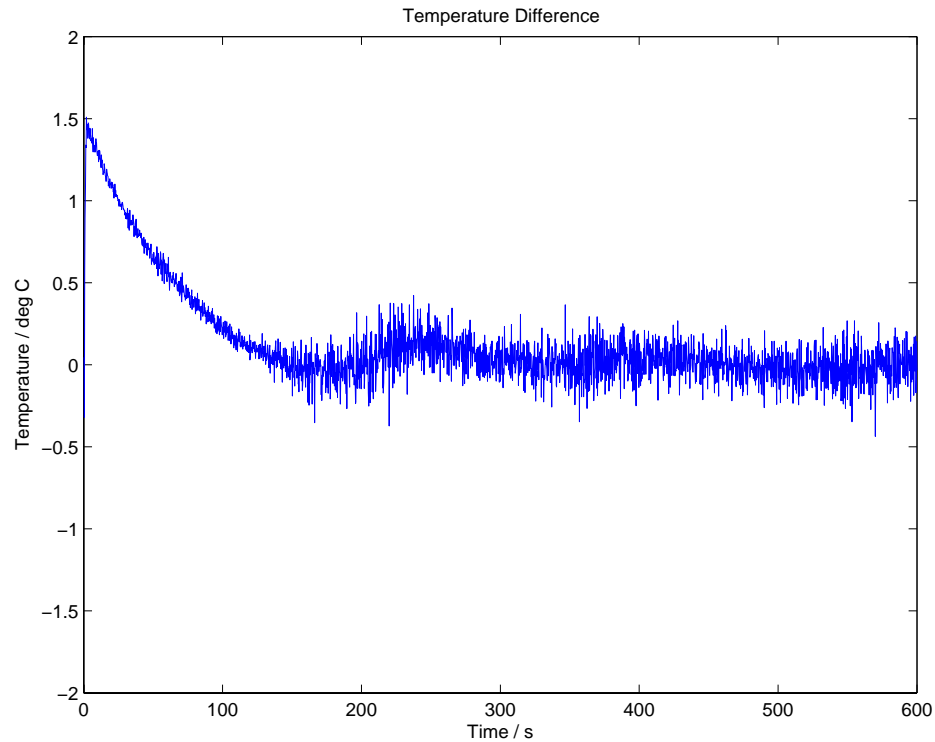


Figure 5-13. Temperature difference between the compensated measurement and reference sensor for experiment with good sensor thermal contact

### 5.5.2 Poor Thermal Contact

Poor thermal contact between the sensor and wafer was created by pasting a layer of tape onto the sensing surface of the RTD. Figure 5-14 shows the first 15s of the experiment for a temperature sensor with poor thermal contact. The high current duration was about 20s (not shown in Figure 5-14) and the closed loop control was commenced 15s after the current was switched back to the nominal value. The least-squares estimation was performed 5s later than the good contact case because a poor contact sensor has a larger time constant. As with section 5.5.1, the sampling rate was chosen to be 10Hz. Using the proposed algorithm, the identified parameters are shown in Table 5-8.  $\hat{K}$  was determined using the relation between  $\tau$  and  $K$  proposed in section 5.4.

$\hat{\tau}$	$\hat{K}$	$\hat{\tau}_{PEB}$	$\hat{A}$
1.80	1.0024	148.4	138.6

Table 5-8. The identified parameters for a sensor with poor thermal contact

To serve as the reference parameters  $\tau$  and  $K$  with which to compare the estimation results of the poor thermal contact experiment, an LCSR test with the least-squares estimator was performed under steady ambient temperature conditions to identify the sensor parameters. Since the identification of the sensor parameters under constant ambient conditions is not subject to the caveat noted in section 5.3, it is reasonable to assume that it provides a more accurate estimate of the sensor parameters. Under constant ambient conditions, the sensor time constant  $\tau$  was found to be 1.63s and using the relation found in section 5.4,  $K$  was 1.00199. Comparing the parameters identified during the PEB process with those identified under constant ambient conditions, it is evident that  $\hat{\tau}$  is close to  $\tau$ . The difference between  $\hat{K}$  and  $K$  is 0.0004 and is within the allowable estimation error noted in section 4.3. Thus, with poor thermal contact between the sensor and wafer, the estimation algorithm is able to determine the sensor parameters.

After switching to closed-loop temperature control, the sampling rate was reduced to 4Hz. The PI controller parameters used were  $P = 10$  and  $I = 0.05$ . Figure 5-15 plots the compensated measurement sensor signal (blue) with the compensated reference sensor signal (black). The filter pole of the compensation algorithm was chosen to be  $\tau_f = 0.25\hat{\tau}$ , for the measurement sensor and  $\tau_f = 0.75\hat{\tau}$  for the reference sensor. In Figure 5-16, the largest temperature difference between the sensors was about 1.6°C.

The critical temperature for the PEB is above 60°C and was crossed about 50s into the experiment (see Figure 5-15). In Figure 5-16, the temperature difference between the sensors falls to within  $\pm 1^\circ\text{C}$  at about 40s into the experiment and finally to within  $\pm 0.1^\circ\text{C}$  at steady state. This demonstrates that the compensation algorithm is able to reduce the measurement errors to within the specified requirements.

The results of this chapter demonstrate that with the use of the sensor parameter identification algorithm, the LCSR test can be performed during the PEB process. The sensor parameters can be identified whilst maintaining the throughput of wafers processed. Using the identified parameters in the compensation algorithm to process the feedback sensor signals, the closed loop wafer temperature control was able to maintain the temperature uniformity between the sensors to within the requirements of  $\pm 1^\circ\text{C}$  during the critical stage of the PEB process and  $\pm 0.1^\circ\text{C}$  at steady state.

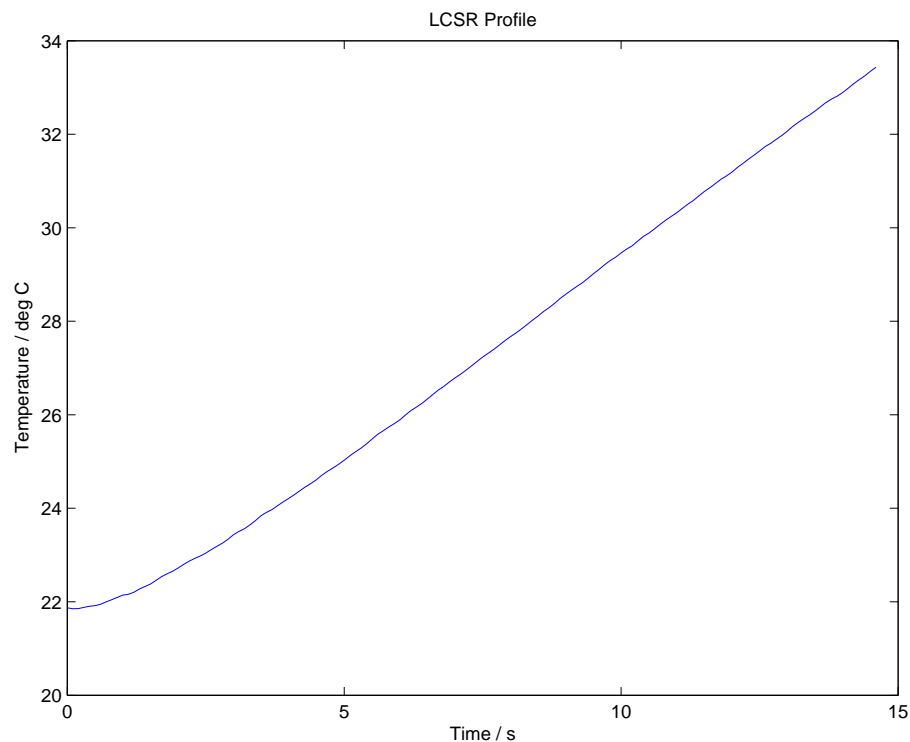


Figure 5-14. Experimental result of LCSR test with wafer heating for sensor with poor thermal contact

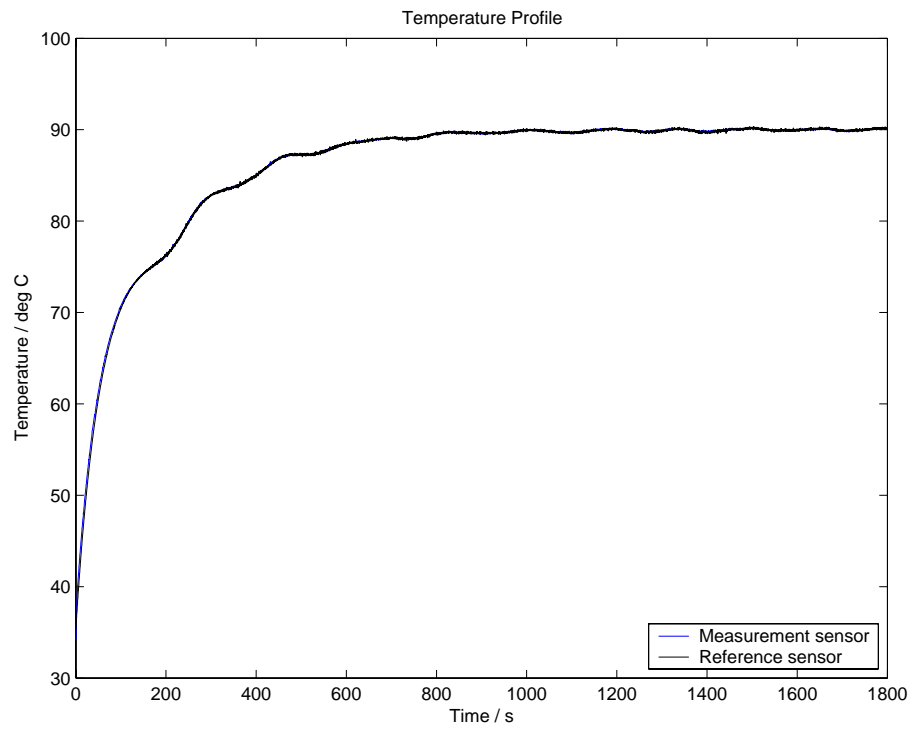


Figure 5-15. Experimental result of closed loop control with compensation for sensor with poor thermal contact

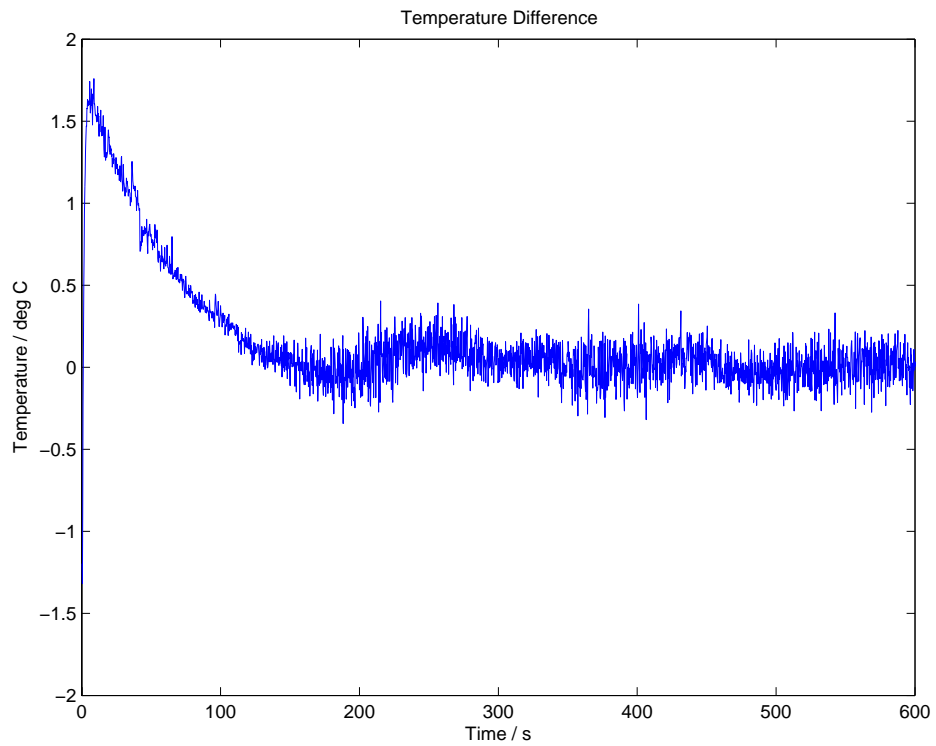


Figure 5-16. Temperature difference between the compensated measurement and reference sensor for experiment with poor sensor thermal contact

## CONCLUSION

The move towards DUV lithography and its use of chemically amplified resists created a situation where the minimum feature size is greatly influenced by the PEB temperature. Hence, tight closed loop control of the PEB temperature across the entire wafer is crucial in ensuring that the reactions of the chemically amplified resist take place properly. Closed loop control techniques may be used to ensure spatial temperature uniformity. However, the performance of closed loop controllers depend on the availability of accurate feedback signals. As poor thermal contact between sensor and wafer adversely affects measurement accuracy, in-situ temperature measurement systems for the PEB process will be practical only if techniques for minimizing the influence of contact level are available.

In an attempt to reduce the undesirable impact of poor thermal contact on measurement accuracy, the Loop Current Step Response test was employed for in-situ testing of the sensor's condition. Hardware for performing the LCSR test was designed and implemented. Experimental results showed that the LCSR test can be carried out by the modified temperature measurement system and the sensor parameters can be identified on-line.

Having successfully implemented the LCSR test on-line, an algorithm that utilizes the LCSR test results to predict the actual PEB temperature is proposed and implemented. Experimental results showed that the proposed algorithm is able to improve the measurement accuracy. When the estimation algorithm was used to provide the temperature feedback signals that is fed to a PI controller, better control performance

was obtained. Although the test results are promising, the algorithm is of limited practical use because the LCSR test must be completed before the PEB process can commence, resulting in a loss in wafer throughput. To address this problem, the sensor parameter estimation algorithm was modified so that the LCSR test and PEB processing can be performed concurrently. The mathematic derivation of the algorithm was presented. Simulation results demonstrated that the sensor parameters could be estimated reasonably accurately even in the presence of measurement noise. However, there was a caveat to the use of the algorithm; the start of the PEB and the instant at which current is switched back to its nominal value had to coincide exactly. A workaround was proposed to enable the parameters to be found. Finally, experiments were conducted and the results demonstrated the ability of the algorithm to identify the sensor parameters. Using the identified parameters in the compensation algorithm to process the feedback sensor signals, the closed loop wafer temperature control was able to reduce the measurement error to within the requirements of  $\pm 1^{\circ}\text{C}$  during transient and  $\pm 0.1^{\circ}\text{C}$  at steady state.

There are several aspects of this research that could benefit from future work. One would be a re-design of the temperature measurement system so that during the high current phase of the LCSR test, a larger current can be passed through the RTD to generate significant electrical power while temperature measurements are made. This can be achieved by providing a higher supply voltage to the AD7711AN chip so that a larger reference voltage can be used, thereby raising the voltage limit where the measurement readings saturate. Such a design would provide the data required to obtain a good estimate of the first data point of the LCSR profile, and ultimately an accurate identification of the sensor thermal contact gain  $K$ . Another possible front for

future work would be to use recursive least-squares to identify the sensor parameters. The current least-squares method identifies the sensor parameters after the LCSR test has been completed. Since the level of thermal contact is not known prior to performing the LCSR test, the test has to be performed for a long duration so that in the event of a larger time constant arising from a poor thermal contact, sufficient data is recorded to allow accurate identification of the sensor parameters. However, in the event of a good thermal contact, the LCSR test would run longer than necessary and delay the resumption of closed loop control. With the recursive least-squares, the sensor parameter is identified real-time so that the LCSR test can be stopped when the value of the identified parameters has remained sufficiently stable. In this manner, the duration of the LCSR test will not be longer than necessary.

## REFERENCES

- 
1. Semiconductor Industry Association, *Semiconductor Industry Association Annual Report 2003*
  2. B. Cohen, W. Renken and P. Miller, *Dynamic in-situ temperature profile monitoring of a deep UV post exposure bake process*, Proc. SPIE Vol. 4689, p. 1133-1142, Metrology, Inspection, and Process Control for Microlithography XVI, 2002
  3. John G. Webster (Editor-in-chief), *The Measurement, Instrumentation and Sensors Handbook*, 1999, CRC Press
  4. Jeffrey Maron, *Selecting Noncontact Pyrometers and Thermometers*, Process Heating Magazine, Jan 1999
  5. Photolithography Notes, Dept of ECE, University of Manitoba
  6. J. Wauters, *Extending Optical Lithography to 0.1 $\mu$ m?*, 8<sup>th</sup> Edition, pp. 175-180, Semiconductor Fabtech journal, Jul 1998
  7. S. J. Holmes, P. H. Mitchell, and M. C. Hakey, *Manufacturing with DUV Lithography*, IBM Journal of Research and Development Volume 41, Numbers 1/2, 1997 Optical lithography
  8. S. Wolf, R. N. Tauber, *Silicon processing for the VLSI era Vol. 1 Process Technology*, 2<sup>nd</sup> Edition, 2000, Lattice Press
  9. J. Sturtevant, S Holmes, P. Rabidoux, *Post-exposure bake characteristics of a chemically amplified deep-ultraviolet resist*, 1992, SPIE vol. 1672 Advances in Resist Technology and Processing IX

- 
10. Luo Jun, *Design of an integrated in-situ temperature measurement system for the microlithography process*, M.Eng Thesis, National University of Singapore. 2001
  11. Tham, T. M., *Design and control of an integrated bake/chill system for the microlithography process*, M.Eng Thesis, National University of Singapore. 2000
  12. Elliott David J., *Integrated circuit fabrication technology*, McGraw-Hill, pp.179-344. 1989
  13. J. Parker, W. Renken. *Temperature metrology for CD control in DUV lithography*, Semiconductor International, Vol. 20(10), pp. 111-117, 1997.
  14. Jackowska-Strumillo, L.; Sankowski, D.; McGhee, J.; Henderson, I.A., *Modelling and MBS experimentation for temperature sensors*, Measurement: Journal of the International Measurement Confederation, Volume 20, Issue 1, January 1997, Pages 49-60
  15. Neslab, *EX-251HT Instruction and Operation Manual*, Rev. 02/02/02, 2002
  16. J. McGhee, I.A. Henderson, L. Michalski, K. Eckersdorf, D. Sankowski, *"Dynamic properties of contact temperature sensors : II Modelling, characterisation and testing of real sensors*, in *Temperature : Its measurement and control in Science and Industry*, vol. 6, Part 2, pp. 1163-1168, 1992.
  17. Henry W. Ott, *Noise reduction techniques in electronic systems*, 2<sup>nd</sup> Edition, 1988, John Wiley & Sons

## **APPENDIX A**

# APPENDIX A

## THE PLATINUM RESISTANCE TEMPERATURE DETECTOR

A resistance-temperature detector (RTD) is a temperature sensing device whose resistance varies with temperature. An RTD consists of a wire coil or deposited film of pure metal enclosed in a sheath of protective casing. RTDs can be made of different metals and have different resistances, like copper, nickel and platinum. Because of its favourable characteristics over the other metals, platinum has become the metal of choice for RTDs. These characteristics include resistance to corrosion and contamination, availability in a pure form, and mechanical and electrical properties that are highly stable and reproducible.

Figure A-1 shows a cross-section of a thin-film RTD. It is extremely small, often less than  $1.6\text{mm}^2$ , and is manufactured by techniques similar to those in the fabrication of integrated circuits. A thin film of platinum is first deposited onto a ceramic substrate. Then, the element's surfaces are covered with glass material to protect the elements from humidity and contaminants and provide strain relief for the external leadwires.

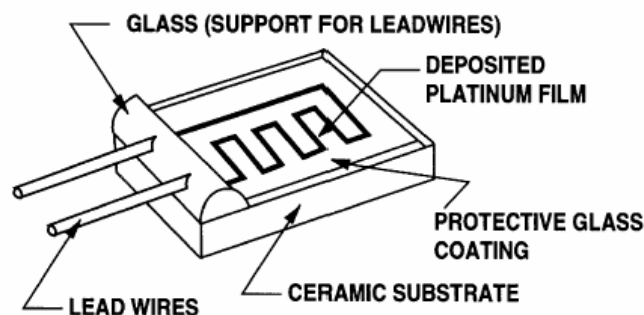


Figure A-1. A thin-film RTD [1]

The nominal resistance of RTDs come in two common values : 100Ω or 1000Ω . A high nominal resistance would be more advantageous because of higher measurement sensitivity and reduced effects of connecting lead resistances on the measurement accuracy. The following sections detail some of the typical characteristics of RTDs.

### ***A.1 Accuracy, Stability and Repeatability***

RTDs have excellent accuracy over a wide temperature range, and some have accuracies as high as 0.01Ω at 0° C. IEC standard 751 sets two tolerance classes for the accuracy of RTDs: Class A and Class B. Class A has an accuracy of  $\Delta T = \pm(0.15 + 0.002 \cdot |T|)$ , whilst that of Class B is  $\Delta T = \pm(0.30 + 0.005 \cdot |T|)$ , where  $|T|$  is the absolute value of temperature in °C. The definition of Class A applies to temperatures from -200°C to 650°C, and only for three- or four- wire configurations. Class B covers the entire range from -200°C to 850°C.

Stability is the sensor's ability to maintain a consistent output when a constant input is applied. Physical or chemical changes can cause calibration drift. The material that the platinum is adhered to can expand and contract, straining the wire. The stability of RTDs is exceptional and common industrial RTDs drift less than 0.1° C per year, and some models are stable to within 0.0025° C year. Drift rates conservatively specified by manufacturers are typically 0.05°C/yr [2].

Repeatability is the sensor's ability to give the same output or reading under repeated identical conditions. In most applications, absolute accuracy is not necessary. Instead,

the focus is on the stability and repeatability of the sensor. If an RTD in a 90°C oil bath consistently reads 90.1°C, other means can easily compensate for this error [2].

## A.2 Linearity

An RTD has a temperature-resistance relationship given by

$$R = R_0 \left( 1 + \gamma_1 T + \gamma_2 T^2 + \dots + \gamma_n T^n \right) \quad (0.1)$$

where  $\gamma_1, \gamma_2, \dots, \gamma_n$  are the temperature coefficients of resistivity and  $R_0$  is the resistance of the RTD at a reference temperature  $T_0$ . This is usually specified at 0°C.

The number of terms in Equation (0.1) is determined by the material used and the range of temperature. Over a narrow range, the higher order terms may be neglected.

From Figure A-2 below, it is clear that platinum is linear over a wide temperature range and this is one reason it is preferred over other metals.

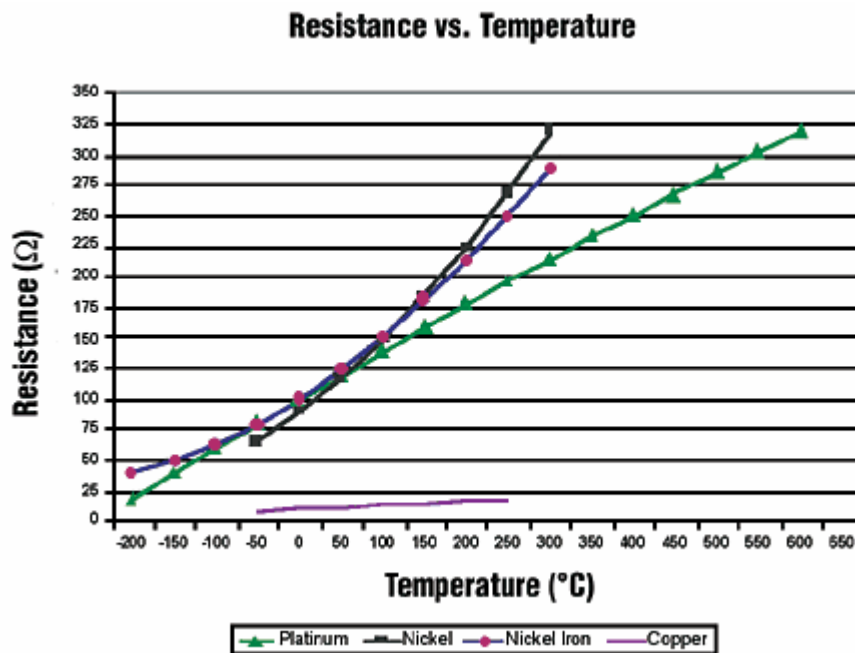


Figure A-2. Resistance-temperature relation of various materials [3]

Each of the different metals used for sensing elements (platinum, nickel, copper) has a different amount of relative change in resistance per unit change in temperature. A measure of a resistance thermometer's sensitivity is its temperature coefficient of resistance, or  $\alpha$ . It is commonly defined as the element's average change in resistance per degree Celsius change, in  $\Omega/^\circ\text{C}$  of sensor resistance over the range of  $0^\circ\text{C}$  to  $100^\circ\text{C}$ .

$$\alpha = \frac{R_{100} - R_0}{R_0 \cdot 100^\circ\text{C}}$$

where  $R_0$  is the RTD resistance at  $0^\circ\text{C}$  and  $R_{100}$  is the resistance at  $100^\circ\text{C}$ .  $\alpha$  has units of  $\Omega/\Omega/^\circ\text{C}$ . The  $\alpha$  of an RTD is a physical and electrical property of the metal alloy and the method by which the element was fabricated.

### ***A.3 Self-Heating***

The excitation current can cause the RTD to heat up internally, via  $I^2R$  heating of resistive elements. Self-heating is typically specified as the amount of power that will raise the RTD temperature by  $1^\circ\text{C}$ , or  $1\text{ mW}/^\circ\text{C}$ . Self-heating can be minimized by using the smallest possible excitation current. The amount of self-heating also depends heavily on the medium in which the RTD is immersed. Self-heating can be up to 100 times higher in still air than in moving water [4].

In applications where the change in temperature measured is small and high sensitivity is required, sensors with large surface areas should be used. In this manner, a large excitation current can be used. The heat generated by the large current can be quickly dissipated by the large surface area.

#### ***A.4 Response Time***

The response time, or the sensor time constant, is typically defined as the time it takes for an RTD to respond to a step change in temperature and come to 63% of its final steady state value. It is an indication of the RTD's ability to react to a change in temperature, and depends on the RTD's thermal mass and proximity to the material being measured. The response time can also vary depending on the application. For instance, an RTD sensor in a thermowell will react more slowly to a temperature change than the same sensor immersed directly into the process.

An advantage of thin-film platinum RTDs is that they are fabricated on a substrate with significantly smaller volume and mass, thus allowing faster response times.

##### ***1.1.1 Signal Conditioning***

RTDs can be difficult to measure because their resistances are relatively low and vary only slightly with temperature. To use it as a measurement device, a constant current (the excitation current) is passed through it, producing a measurable voltage. Any change in the measured temperature causes the resistance to change, and this is reflected as a change in the voltage across it. It is important that the constant current source is stable and has a low temperature coefficient, otherwise changes in the measured voltage will not be due only to the resistance, and the sensor readings will be inaccurate.

- 
1. John G. Webster Editor-in-chief, *The measurement, instrumentation and sensors handbook*, 1999, CRC Press
  2. Doris Gavey, *So What is an RTD?*, Sensor Magazine, August 1999
  3. Randal A. Gauthier, *Time to Learn Your RTDs*, Sensor Magazine, May 2003
  4. National Instruments, *Measuring temperature with RTDs*, 1996

## **APPENDIX B**

## APPENDIX B

### Modifications to the Firmware

(Note : Additions/modifications to the code are highlighted in bold)

#### **AD7711.c**

- Added cases 'rmLCSRON' and 'rmLCSROFF' in function 'MainLoop' to switch on and switch off Port D7

```
#include <80c196.h>
#include <psd401.h>
#include <AD7711.h>
#include "RunMode.h"

#define True 1
#define False 0

extern void Idle96(void);
static register volatile ERunMode RunMode;
static register unsigned char bAverSampleBits;
static register unsigned char ADCStarted;
static register unsigned char ADCMode;
static register unsigned char ADCCGain;
static register unsigned int ADCFilter;
static register unsigned int DelayCount;
static register unsigned int *pADBuf, ChipMask;
static register unsigned char *pbData, BitMask;
static register unsigned char WordCnt;
static register unsigned char Ret;
static register unsigned char Round;
static register unsigned char *pbLast;
static register unsigned long TheLong, *plSum;
static register unsigned int RawADBuf[ADWORDLENGTH << 3];
static register unsigned char XchgADBuf[ADWORDLENGTH << 4];
extern unsigned long Sum[16];
extern unsigned char ADData[(ADWORDLENGTH << 4) * AverSamples];

/* -----
function to delay Cnt times
-----*/
void Delay(void)
{
    while(--DelayCount);
}
#define DELAY(COUNT) DelayCount=COUNT; Delay()

/* -----
function to read the SDATA from 16 AD7711s to RawADBuf
-----*/
void ReadADCs(void)
{
    pADBuf = RawADBuf;
    WordCnt = ADWORDLENGTH << 3;
```

```

do
{
    *(pADBuf++) = PortABIn;
    Set_SCLK;
    DELAY(SCLK_PulseDelay);
    Clear_SCLK;
}
while (--WordCnt);
Stop_Access;
} /* end of ReadADCs function */

/* -----
function to write the SDATA to 16 AD7711s from RawADBuf
-----*/
void WriteADCs(void)
{
    pADBuf = RawADBuf;
    WordCnt = ADWORDLENGTH << 3;
    do
    {
        PortABOut = *(pADBuf++);
        Set_SCLK;
        DELAY(SCLK_PulseDelay);
        Clear_SCLK;
    }
    while (--WordCnt);
    Stop_Access;
} /* end of WriteADCs function */

/* -----
function to decode the SDATA in RawADBuf
-----*/
void DecodesSDATA(void)
{
    pbData+= ADWORDLENGTH << 4;
    ChipMask= 0x8000; /* Bit15 stands for the 15th AD7711 */
    do
    {
        pADBuf= RawADBuf;
        WordCnt= ADWORDLENGTH;
        do
        {
            *(--pbData) = 0;
            BitMask= 0x80;
            do
            {
                if (*(pADBuf++) & ChipMask)
                    *pbData|= BitMask;
                BitMask= BitMask >> 1;
            }
            while (BitMask);
        }
        while (--WordCnt);
        ChipMask= ChipMask >> 1;
    }
    while (ChipMask);
} /* end of DecodesSDATA function */

/* -----
function to encode the SDATA in RawADBuf
-----*/

```

```

-----*/
void EncodeSDATA(void)
{
    WordCnt= (ADWORDLENGTH << 4) / 2;
    pADBuf= RawADBuf;
    do
        *(pADBuf++) = 0;
    while (--WordCnt);
    pbData+= ADWORDLENGTH << 4;
    ChipMask= 0x8000;      /* Bit15 stands for the 15th AD7711 */
    do
    {
        pADBuf = RawADBuf;
        WordCnt = ADWORDLENGTH;
        do
        {
            pbData--;
            BitMask = 0x80;
            do
            {
                if (*pbData & BitMask)
                    *pADBuf |= ChipMask;
                pADBuf++;
                BitMask= BitMask >> 1;
            }
            while (BitMask);
        }
        while (--WordCnt);
        ChipMask= ChipMask >> 1;
    }
    while (ChipMask);
} /* end of EncodeSDATA function */

/* -----
   function to copy the first 3 bytes into rest of XchgADBuf
-----*/
void DupCtrlReg(void)
{
    WordCnt=0;
    pbData= XchgADBuf;
    do
    {
        *(pbData+3)= *pbData;
        pbData++;
    }
    while(++WordCnt < 3*15);
}

/* -----
   function to set the 16 adc7711 control registers
-----*/
void PutCtrlReg(void)
{
    EncodeSDATA();
    Start_WriteCtrl;
    WriteADCs();
} /* end of PutCtrlReg function */

/* -----
   function to get the 16 adc7711 data/calibration registers
-----*/

```

```

void GetDataReg(void)
{
    Start_ReadData;
    ReadADCs();
    DecodeSDATA();
} /* end of GetDataReg function */

/* -----
   function to set the 16 adc7711 data/calibration registers
   -----*/
void PutDataReg(void)
{
    EncodeSDATA();
    Start_WriteData;
    WriteADCs();
} /* end of PutDataReg function */

/* -----
   function to test whether all 16 ad7711s are ready
   -----*/
void IsReady(void)
{
    while (Port01 & WorkSet)
        if (--DelayCount == 0)
        {
            RunMode= rmADCOutOfTime;
            Ret= False;
            return;
        };
    Ret= True;
    return;
}
#define      ISREADY(COUNT)          DelayCount=COUNT; IsReady(); if
(Ret)
#define      TESTREADY(COUNT)      DelayCount=COUNT; IsReady()

/* -----
   Write control registers of the 16 AD7711s
   -----*/
void WriteCtrl(void)
{
    if (ADCFilter < 19)
        ADCFilter= 19;
    if (ADCFilter > 2000)
        ADCFilter= 2000;
    XchgADBuf[2]= (ADCMode << 3 | ADCGain & 7) << 2;
    /* channel is always AIN1 here.*/
    XchgADBuf[1]= 0xd0;
    /* 1(uses 24bit word, keep accord with ADWORDLENGTH)
       1(RTD current on)
       0(burnout current off)
       1(unipolar)*/
    XchgADBuf[1]|= ADCFilter >> 8;
    XchgADBuf[0]= ADCFilter & 0xff;
    DupCtrlReg();
    pbData= XchgADBuf;
    PutCtrlReg();

    if ((ADCMode>0) && (ADCMode<5))
    {
        /* ignore the /DRDY status for a modulator cycle at least,

```

```

    and wait until calibrations over*/
    for (WordCnt=0; WordCnt< 20; WordCnt++)
    {
        DELAY(30000);
    };
    TESTREADY(20000);
};
return;
}

void IdleAD7711s(void)
{
    XchgADBuf[2]= (ADCGain & 7) << 2 | 0x01;
    /* 000, normal mode
       0, channel is always AIN1 here.
       1, power down*/
    XchgADBuf[1]= 0x90;
    /* 1(uses 24bit word, keep accord with ADWORDLENGTH)
       0(RTD current off)
       0(burnout current off)
       1(unipolar)*/
    XchgADBuf[1]|= ADCFilter >> 8;
    XchgADBuf[0]= ADCFilter & 0xff;
    DupCtrlReg();
    pbData= XchgADBuf;
    PutCtrlReg();
}

/* -----
   function to perform alrothim average
   -----*/
void AverData(void)
{
    WordCnt=16;
    plSum= Sum;
    do
        *(plSum++)= 0;
    while (--WordCnt);

    WordCnt= 1 << bAverSampleBits;
    pbData= ADDData;
    do
    {
        ChipMask=0x8000;
        plSum= Sum;
        do
        {
            *((unsigned char *)&TheLong)= *(pbData++);
            *((unsigned char *)&TheLong)+1)= *(pbData++);
            *((unsigned char *)&TheLong)+2)= *(pbData++);
            *(plSum++)+= TheLong;
            ChipMask= ChipMask >> 1;
        }
        while (ChipMask);
    }
    while (--WordCnt);

    ChipMask= 0x8000;
    plSum= Sum;
    pbData= XchgADBuf;

```

```

do
{
    *plSum= *plSum >> bAverSampleBits;
    *(pbData++)= *((unsigned char *)plSum);
    *(pbData++)= *((unsigned char *)plSum)+1);
    *(pbData++)= *((unsigned char *)plSum)+2);
    plSum++;
    ChipMask= ChipMask >> 1;
}
while (ChipMask);
}

/* -----
   function to get the latest results of 16 ad7711s into pbData
   -----*/
void GetADResult(void)
{
    if (Port01 & WorkSet)
        return;
    pbData= pbLast;
    pbLast+= (ADWORDLENGTH<<4);
    if (pbLast >= ((unsigned char *)ADData + sizeof(ADData)))
        pbLast= ADDData;
    GetDataReg();
    AverData;
    RunMode = rmReady;
} /* end of GetADResult function */

void ResetAD7711s(void)
{
    TheLong= 0;
    bAverSampleBits= AverSampleBits;
    Round=0;
    pbLast= ADDData;
    AD CGain= AD7711Gain;
    ADCFilter= AD7711Filter;
    ADCMode= 1;
    WriteCtrl();

/* synchronize 16 ADCs */
    Start_Sync;
    DELAY(5);
    Stop_Access;
}

void InitPorts(void)
{
    PortABCtrl= 0xFFFF; /* sets all pins of port A and B as MCU I/O*/
    PortCDCtrl= 0xFFFF; /* sets all pins of port C and D as MCU I/O*/
    Stop_Access;
    Clear_SCLK;
    PortCDDir= 0xFFFF; /* sets all pins of port C and D as output */
    PortDOut=0x00;
    ioport1= 0xff;
}

void MainLoop(void)
{

```

```

RunMode=rmUnknown;
ADCStarted= False;
do
{
    switch (RunMode)
    {
        case rmReset:{      RunMode=rmBusy;
                          InitPorts();
                          ResetAD7711s();
                          break;
                        };
        case rmIdle: {      IdleAD7711s();
                          Idle96();
                          RunMode= rmReady;
                          break;
                        };
        case rmQuit: {      RunMode=rmUnknown;
                          return;
                        };
        case rmUnknown:    break;
        case rmBusy:
        case rmReady:{      GetADResult();
                          break;
                        };
        case rmADCOutOfTime:break;
        case rmLCSRON: {
                          PortDOut|= 0x80;
                          RunMode = rmReady;
                          break;
                        };
        case rmLCSROFF: {
                          PortDOut&= 0x0F;
                          RunMode = rmReady;
                          break;
                        };
        default:           RunMode=rmUnknown;
    };
}
while(1);
}

```

### **AD7711.h**

- Changed defined value of 'AD7711Filter' to increase AD7711 sampling rate
- Changed defined value of 'AverSamples' to reduce number of samples in moving average window
- Changed defined value of 'Set\_SCLK' so that Port D7 status will not be affected by setting of S\_CLK
- Changed defined value of 'Clear\_SCLK' so that Port D7 status will not be affected by clearing of S\_CLK

```

#include <80c196.h>
#include <PSD401.h>

```

```

#ifndef _AD7712h
#define _AD7712h

#define Ch1 0x4000
#define Ch2 0x8000
#define Ch3 0x2000
#define Ch4 0x1000
#define Ch5 0x0400
#define Ch6 0x0800
#define Ch7 0x0200
#define Ch8 0x0100
#define Ch9 0x0080
#define Ch10 0x0040
#define Ch11 0x0020
#define Ch12 0x0010
#define Ch13 0x0004
#define Ch14 0x0001
#define Ch15 0x0008
#define Ch16 0x0002

/* the parameters of ad7711s */
#define Gain1 0x00
#define Gain2 0x01
#define Gain4 0x02
#define Gain8 0x03
#define Gain16 0x04
#define Gain32 0x05
#define Gain64 0x06
#define Gain128 0x07

#define AD7711Gain Gain4
#define AD7711Filter 781
#define ADWORDLENGTH 3
#define WorkSet 0xffff
#define AverSampleBits 2
#define AverSamples 1 /* (1<<AverSampleBits) */
/* set to 1 if no averaging used */

/* macros for ad7711 control */
#define Start_ReadCtrl PortABDir= 0x0000; PortCOut= 0x3C
/* RFS= low, A0= low */
#define Start_ReadData PortABDir= 0x0000; PortCOut= 0xFC
/* RFS= low, A0= high */
#define Start_WriteCtrl PortABDir= 0xffff; PortCOut= 0x33
/* TFS= low, A0= low */
#define Start_WriteData PortABDir= 0xffff; PortCOut= 0xF3
/* TFS= low, A0= high */
#define Stop_Access PortABDir= 0x0000; PortCOut= 0xFF
/* RFS= TFS= high */
#define Start_Sync PortCOut= 0xCF
#define Set_SCLK PortDOut|= 0x0F
/* SCLK= 1 */
#define Clear_SCLK PortDOut&= 0xF0
/* SCLK= 0 */
#define SCLK_PulseDelay 0x02
/* delay constant for active SCLK pulse*/
#endif

```

## ***RUNMODE.h***

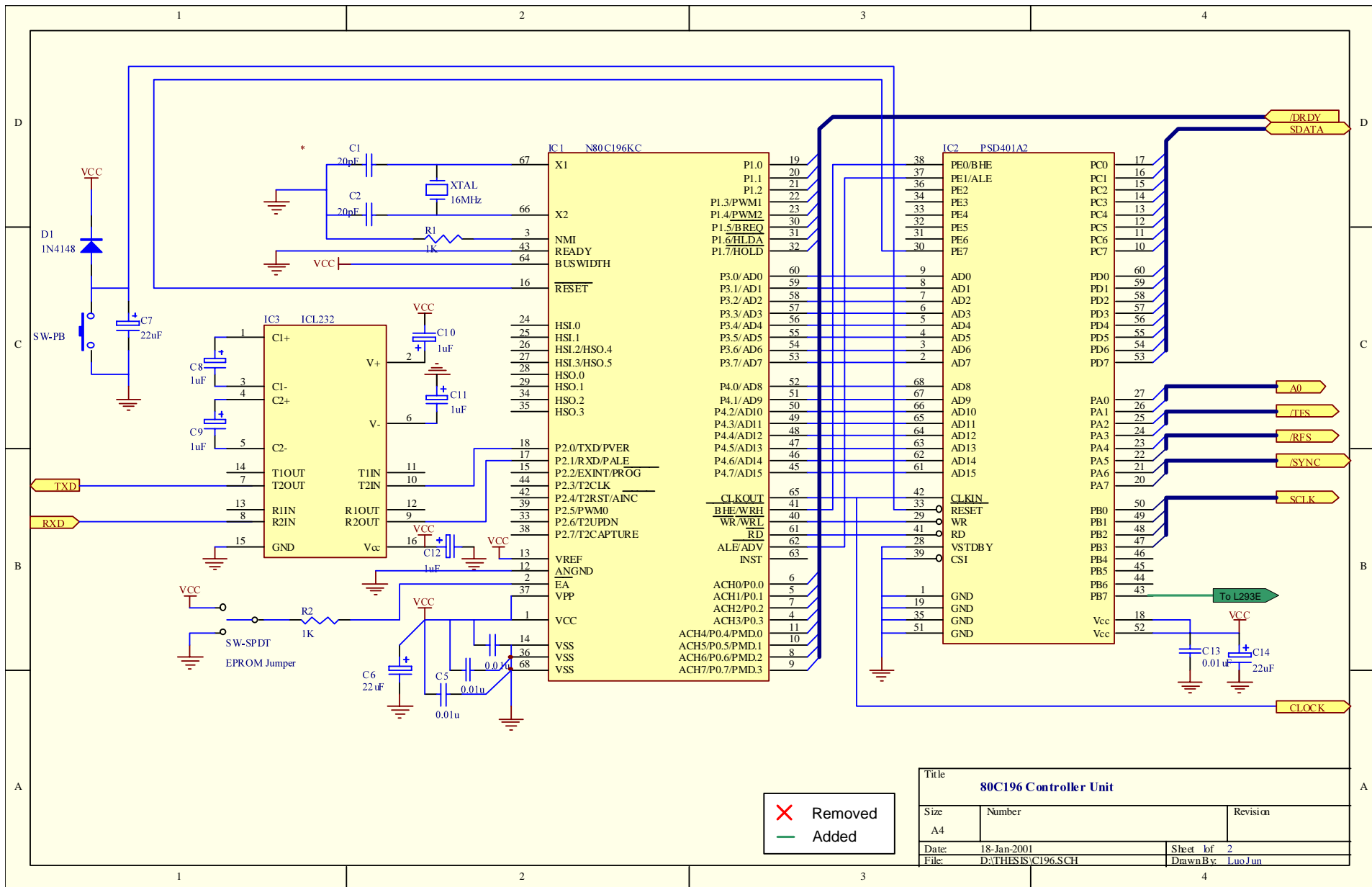
- Added 'rmLCSRON' and rmLCSROFF'

```
#ifndef _RunModeh
#define _RunModeh

typedef enum
{
    rmInit,                /* issued by PC */
    rmCali,                /* issued by PC */
    rmReset,              /* issued by PC */
    rmAcqu,               /* issued by PC */
    rmIdle,               /* issued by PC */
    rmQuit,              /* issued by PC */
    rmUnknown,          /* reported by C196 */
    rmBusy,              /* reported by C196 */
    rmReady,            /* reported by C196 */
    rmADCOutOfTime, /* reported by C196 */
    rmLCSRON,          /* issued by PC */
    rmLCSROFF       /* issued by PC */
} ERunMode;

#endif
```

## **APPENDIX C**



X Removed  
— Added

Title		
<b>80C196 Controller Unit</b>		
Size	Number	Revision
A4		
Date:	18-Jan-2001	Sheet of 2
File:	D:\THESIS\IC196.SCH	Drawn By: Luo Jun

